ABSORPTION HEAT PUMP FOR SPACE APPLICATIONS

FINAL REPORT

NASA Grant # NAG 9-613

December, 1993

Lamar University
College of Engineering
Beaumont, Texas

Tuan Nguyen, Ph.D., P.E., Principal Investigator
William E. Simon, Ph.D., P.E., Research Associate
Gopinath R. Warrier, M.S., Graduate Assistant
Woranun Woramontri, M.S., Graduate Assistant

ABSTRACT

Absorption Heat Pumps for Space Applications

In the first part of this study, the performance of the Absorption Heat Pump (AHP) with water-sulfuric acid and water-magnesium chloride as two new refrigerant-absorbent fluid pairs was investigated. A model was proposed for the analysis of the new working pairs in a heat pump system, subject to different temperature lifts. Computer codes were developed to calculate the Coefficient of Performance (COP) of the system with the thermodynamic properties of the working fluids obtained from the literature. The study shows the potential of water-sulfuric acid as a satisfactory replacement for water-lithium bromide in the targeted temperature range. The performance of the AHP using water-magnesium chloride as refrigerant-absorbent pair does not compare well with those obtained using water-lithium bromide.

The second part of this study concentrated on the design and testing of a simple ElectroHydrodynamic (EHD) Pump. A theoretical design model based on continuum electromechanics was analyzed to predict the performance characteristics of the electrohydrodynamic (EHD) pump to circulate the fluid in the absorption heat pump. A numerical method of solving the governing equations was established to predict the velocity profile, pressure - flow rate relationship and efficiency of the pump. The predicted operational characteristics of the EHD pump is comparable to that of turbomachinery hardware; however, the overall efficiency of the electromagnetic pump is much lower. An experimental investigation to verify the numerical results was conducted. The pressure - flow rate performance characteristics and overall efficiency of the pump obtained experimentally agree well with the theoretical model.

TABLE OF CONTENTS

LIST OF TABLES

LIST OF FIGURES

Figure Page

Section I

Section II

Section I

Refrigerant -Absorbent Pair Selection for the Absorption Heat Pump

Refrigerant-Absorbent Pair Selection for the Absorption Heat Pump

Introduction

The absorption heat pump (AHP) has come a long way since its invention by Ferdinand Carré in 1860. Due to the inherent absence of moving parts, the AHP has the advantage of relative simplicity and potential reliability. On the other hand, it requires large heat exchangers for acceptable coefficient of performance (COP). It also exhibits relatively lower cooling-mode COP as compared to that of Rankine cycle refrigeration machinery. The COP of the AHP depends on the following parameters:

System Configuration. The system configuration refers to the various components that make up the heat pump. The components of the system are usually dependent on the particular application, refrigerant-absorbent pair, and other factors like space, weight, etc. The final layout of the heat pump is generally determined by the economics of the system.

Operating Temperature Range. The operating temperature range decides the selection and performance of the refrigerant-absorbent fluid pair. An optimal temperature range cannot be specified for all applications. The temperature range for an AHP is decided by the type of heat source and heat sink.

Properties of Refrigerant-Absorbent Pair. The thermodynamic properties of the refrigerant-absorbent pair are the deciding factor in its selection as a feasible working pair. The properties needed to calculate the COP of an AHP have been discussed in detail by Alefeld (1987). The desirable properties of the working pairs are described in later sections.

Various system configurations used to improve the COP of the AHP have been reported (Serpente, Perez-Blanco, & Seewald, 1992; Garimella, Christensen, & Petty,

1992). These modifications have resulted in an improvement in system COP. The operating temperatures in almost all practical heat pumps depend on the particular application. A temperature range cannot be prescribed for all cases; however, a suitable choice of refrigerant-absorbent pair will allow an optimum COP. The most commonly used refrigerant-absorbent fluid pairs are ammonia-water (NH_3-H_2O) and water-lithium bromide (H_2O-LiBr). The properties and working parameters of these fluid pairs have been thoroughly investigated (ASHRAE Handbook, 1985). A few other working pairs have been suggested (Bhatt, Krishna Murthy, & Seetharamu, 1992; Kaushik, Gadhi, Agarwal, & Kumari, 1988). The basis for the selection of a refrigerant-absorbent pair has been described in the literature (Mansoori & Pate, 1979; ASHRAE Handbook, 1985). The AHP analysis based on the first and second laws of thermodynamics has also been well documented (ASHRAE Handbook, 1985; Stoecker & Jones, 1982).

In the present effort, an attempt was made to understand the thermodynamics of new refrigerant-absorbent pairs. The objectives of this study were twofold:

1. To investigate the feasibility of using water-sulfuric acid and water-magnesium chloride as new refrigerant-absorbent fluid pairs for the absorption heat pump.
2. To design an EHD pump for space applications.

The first part of the study deals with the determination of thermodynamic properties of aqueous sulfuric acid and aqueous magnesium chloride solutions. The thermodynamic properties of interest in AHP simulation are vapor pressure, solubility, relative volatility, latent heat and enthalpy of the fluid pairs. A computer program was written to calculate the performance of both working fluid pairs in the system.

The design and development of an EHD pump has been detailed in the second part of this study. The results obtained testing the pump are also presented.

Characteristics of Refrigerant-Absorbent Fluid Pair

The efficiency of the absorption heat pump depends on the selection of a proper refrigerant-absorbent fluid pair. The operating pressures, heat transfer rates and hence the COP of the system are decided by the physical, transport, and thermal properties of the refrigerant-absorbent pair. The following section discuss the desirable properties of the working pairs. The thermodynamic properties of sulfuric acid solution and aqueous magnesium chloride are also described.

Desirable Properties of Refrigerant-Absorbent Pairs

Certain chemical and physical properties of the refrigerant-absorbent pair must be satisfied before it can be selected for use in the absorption heat pump. The properties of interest specified by the American Society of Heating, Refrigerating and Air-Conditioning Engineers (ASHRAE) are:

Absence of Solid Phase. The refrigerant-absorbent pair should not form a solid phase over the operating concentration and temperature ranges. The freezing-point temperature and crystallization-point temperature of the pair over the operating concentration range should be well below the corresponding operating temperature. The presence of solid phase depends on the maximum solubility of the refrigerant in the absorbent at a given temperature.

High Volatility Ratio. The volatility ratio is the ratio of the refrigerant volatility to that of the absorbent at any given pressure. The volatility ratio directly affects the heat transfer rate in the generator. As the volatility ratio increases, the ease of separation improves. The volatility of the refrigerant must be higher than that of the absorbent (i.e., relative volatility >> 1).

Strong Affinity. The absorbent must possess strong affinity for the refrigerant under normal operating conditions, greater the affinity between the refrigerant-absorbent pair the lesser the amount of absorbent to be circulated.

Moderate Operating Pressure. The operating pressures of the heat pump depend on the physical properties of the refrigerant-absorbent pair. High pressures necessitate the use of thick-walled equipment while low pressures necessitate the use of large volume equipment. Moderate pressures are therefore preferred.

Chemical Stability. The refrigerant-absorbent pair needs to be chemically stable under normal operating conditions. Chemical instability can lead to the formation of unwanted substances such as solids, gases or corrosives that can damage the equipment.

Low Corrosiveness. Almost all the commonly used refrigerant-absorbent pairs are corrosive to some extent. Care should be taken to minimize corrosion of mechanical parts.

Safety. As far as possible the fluid pairs used in the absorption heat pump should be nontoxic and nonflammable. Fluids that are not safe are limited to outdoor use.

Transport Properties. The refrigerant-absorbent pair should possess such properties as low viscosity, moderate density, low surface tension, high thermal diffusivity and high mass diffusivity. These transport properties have an effect on the overall performance of the system.

High Latent Heat. The latent heat of the refrigerant has a large impact on the refrigerating effect. The greater the latent heat, the lesser is the circulation rate of both refrigerant and absorbent.

Detailed characteristics of commonly used refrigerant-absorbent pairs have been reported at length in the literature (ASHRAE Handbook, 1985). The properties considered in the present study are solubility, pressure, enthalpy, relative volatility and

freezing point. All the concentrations referred to in this study are with respect to the absorbent (H_2SO_4 or $MgCl_2$).

Thermodynamic Properties of Water-Sulfuric Acid Fluid Pair

The thermodynamic properties of interest in the determination of the COP are temperature, pressure and concentration. Knowledge of any two of the three implies the third. The physical properties of the fluid pair establish the operating pressures of the cycle. The properties of water-sulfuric acid solution have been documented in the literature (Warrier, Annamalai, Nguyen, & Lin, 1993). The total pressure of the fluid pair as a function of temperature and concentration was regressed from data available in the literature (Chemical Engineers' Handbook, 1973; CRC Handbook of Chemistry and Physics, 1980). The total pressure of the solution as a function of temperature and concentration is given in Table 1. The equation in Table 1 is an Antoine-type equation with 50 data points utilized for the regression. The percentage error for the regressed equation was ±3%. The computed mean square error was 18.5 and the absolute standard deviation was 4.3.

Sulfuric acid is completely soluble in water at all temperatures (infinite solubility). In cold water, heat is evolved during mixing (heat of dilution), while in hot water no heat is evolved. Since sulfuric acid theoretically has infinite solubility, sulfuric acid solution of any concentration may be used. The concentrations used in practice are limited by the corrosiveness of the sulfuric acid solution.

It is essential that the solution does not freeze within the operating temperatures and concentrations. The freezing point of water-sulfuric acid solution as a function of the solution concentration can be obtained from Chemical Engineers' Handbook (1950). The data obtained are plotted in Figure 1. As the solution freezing points are well below the

normal operating temperature limits over most concentrations, the chances for the solution freezing and causing equipment shutdown are minimal.

The ease of separation of the refrigerant from the solution depends upon the relative volatility of the refrigerant in the solution at the given temperature and pressure. The greater the relative volatility, the easier is the separation. The relative volatility of water in an aqueous sulfuric acid solution is determined using the equation outlined in Table 2. The relative volatility of the aqueous sulfuric acid solution for various temperatures and at the generator pressure is illustrated in Figure 2, where y_i and x_i are obtained from equilibrium vapor pressure data. Figure 3 shows the variation in relative volatility with pressure. From Figure 3, it can be seen that as the operating pressure increases, the relative volatility increases and the separation becomes easier. This property helps provide an initial estimate of the feasible operating pressure range.

The vapor pressure equilibrium diagram for a mixture is also important during the preliminary design stages, since the formation of azeotropes should be avoided. An azeotrope is formed when the mole fraction of a substance in a mixture is equal in both the liquid and vapor phases (i.e., $y_i = x_i$). An azeotrope forms a constant boiling point mixture and hence separation becomes impossible.

The COP of the absorption heat pump depends on the enthalpy of the solution at various temperatures and concentrations. The enthalpy for various temperatures and concentrations was regressed from enthalpy-concentration diagrams available in the literature (Smith & Van Ness, 1979). The enthalpy as a function of temperature and concentration is given in Table 3. The effect of pressure on the enthalpy of the solution is negligible. The regression was performed using a total of 50 data points. The computed mean squared error was 33.14 and the absolute standard deviation was 5.76. The percentage error was found to be 4.36%.

Thermodynamic Properties of Water-Magnesium Chloride Fluid Pair

The thermodynamic properties of aqueous magnesium chloride solution are described in this section. Like all salts, magnesium chloride has limited solubility at a given temperature. The operating concentration at any given temperature should be less than the maximum solubility at that temperature to prevent crystallization. Crystallization of the salt leads to blockage of equipment and shutdown of the unit. The maximum solubility of magnesium chloride is given by the correlation shown in Table 4. The solubility data was obtained from the literature (Mel'nik & Mel'nikov, 1970). The maximum solubility at various temperatures is plotted in Figure 4. As seen from the figure, the solubility limits the operating concentration range at any temperature.

The vapor pressure of water-magnesium chloride solution was obtained from the literature (Sako, Hakuta, & Yoshitome, 1985; Patil, Tripathi, Pathak, & Katti, 1991). The equations used to calculate vapor pressures of the solution are shown in Tables 5 and 6. These correlations in Table 5 and 6 are Antoine-type equations. Available experimental data are very limited. No data are available for vapor pressure in the temperature range of 273K to 303K. Similarly, no vapor pressure data are available for higher molalities. Hence, the equations available in the literature were extrapolated to determine the vapor pressure.

The relative volatility of the water (refrigerant) in a water-magnesium chloride solution was calculated using the equation described earlier in Table 2. The relative volatility is shown in Figure 5 as a function of pressure. The relative volatility of water is very high as seen in Figure 5, and hence separation will not be a problem.

The enthalpy of aqueous magnesium chloride was determined from data available in the literature (Snipes, Manly, & Ensor, 1975). Table 7 shows the equation used to fit the data points determined experimentally. A total of 43 data points were used for the

regression analysis. The mean square error was 0.069 and the absolute standard deviation was 0.263. The mean percentage error was calculated to be ±0.04%. Enthalpy at higher temperatures were obtained from experimental data (Mayrath & Wood, 1983). The regression analysis was done using a total of 46 data points. The mean square error was 0.002 and the absolute standard deviation was 0.052. The mean percentage error was ± 0.15%. The correlation equation is shown in Table 8. As seen from Tables 7 and 8, the enthalpy correlations do not cover all temperature and molality ranges. The correlation equations obtained have been extrapolated to obtain vapor pressure and enthalpy data for those ranges for which no experimental data were available.

Absorption Heat Pump Cycle Analysis

The properties of the refrigerant-absorbent pairs were discussed in the previous sections. This section discusses the analysis of the performance of water-sulfuric acid and water-magnesium chloride as new refrigerant-absorbent pairs. The AHP configuration, basic governing equations and performance calculation procedure are described in the following sections.

Absorption Heat Pump Configuration

A simple AHP configuration was chosen for this study. The system consists of a generator(G), condenser(C), evaporator(E), absorber(A), and a solution-side heat exchanger (HE) as shown in Figure 6 (Stoecker & Jones, 1982). The function of a compressor in a vapor-compression system is accomplished in a vapor-absorption system by the combination of the absorber, solution pump and generator. Heat is supplied at the generator to boil off the refrigerant from the strong solution. The generator is a separation device where the fluids are separated by distillation. The differences in the boiling points between the fluids and the relative volatility of the refrigerant are the factors deciding the ease of separation. The temperature and pressure of the refrigerant leaving the generator are in equilibrium. The high-pressure refrigerant vapor is condensed at the condenser, where heat is released. An expansion device then expands the liquid refrigerant to a lower pressure state prior to the evaporator.

The liquid refrigerant absorbs the heat of vaporization and evaporates in the evaporator. The temperature and pressure of the low-pressure vapor leaving the evaporator are in equilibrium. This vapor is absorbed at the absorber by the weak solution returning from the generator. The heat of dilution is removed in the absorber. The strong solution is pumped to the high-pressure generator by a pump. The refrigerant is then

regenerated in the generator and the cycle continues. A heat exchanger is provided prior to the generator to transfer the heat from the hot, weak solution exiting the generator to the cool, strong solution being pumped from the absorber. This heat exchanger has a positive impact on the COP of the system as it reduces the supplied heat to the generator required to free the absorbate.

Governing Equations and Performance Calculation

The following three equations form the basis for the thermodynamic analysis of the absorption heat pump cycle.

Mass Balance. The mass balance equation is given by:

$$\sum_{i}^{n} m_i = 0 \tag{1}$$

where, m is the mass flow rate.

Partial Mass Balance (Material Balance). The conservation of individual mass balance is given by:

$$\sum_{i}^{n} m_i \, \xi_i = 0 \tag{2}$$

where, m is the mass flow rate and ξ the solution concentration.

Energy Balance. The conservation of energy is given by:

$$\sum_{i}^{n} Q_i + \sum_{i}^{n} m_i \, h_i = 0 \tag{3}$$

where, Q is the heat transfer and m the mass flow rate. The above equations can be applied to any state point of the heat pump system.

The performance calculations are based on the following assumptions:

1. The load is constant at 1 ton.
2. Selected evaporator, condenser and absorber temperatures are maintained constant. (T_a= 303K, T_e = 283K, T_c = 313K)

3. Equilibrium conditions exist at the generator and absorber outlets.

4. The expansion processes are isenthalpic.

5. The heat exchanger effectiveness (ε) is 0.8.

With a 1-ton load and constant temperatures at the evaporator, condenser and absorber, the COP of the system was calculated for various temperature lifts (i.e., temperature difference between the hot and cold plates). The condenser/generator pressure was the saturation pressure of the refrigerant vapor corresponding to the condenser temperature (T_c = 303K). Saturation pressures and enthalpies of the refrigerant at different state points were obtained from the literature (Raznjevic, 1976). The saturation pressure corresponding to the evaporator temperature (T_e = 283K) dictates the pressure of the evaporator/absorber that forms the low pressure side of the system. As the load is maintained constant, the refrigerant mass flow rate is constant. The refrigerant mass flow rate corresponding to state point 6 in Figure 6 is given by:

$$m_6 = \frac{\text{load}}{h_7 - h_6} = \frac{Q_e}{h_7 - h_6} \tag{4}$$

where, h_6 and h_7 are the enthalpies corresponding to saturated water at (T_c and P_c) and (T_e and P_e), respectively, Q_e being the heat transfer at the evaporator.

The following mass flow rate relations are applicable to the system: $m_1 = m_2$, $m_3 = m_4$, and $m_5 = m_6 = m_7$. The total mass flow rate of the system is obtained from:

$$m_1 = m_3 + m_5 \tag{5}$$

The H_2SO_4 mass flow rate is calculated from:

$$m_1 \xi_1 = m_3 \xi_3 \tag{6}$$

where, ξ_1 = concentration based on T_a and P_a and ξ_3 = concentration of solution based on T_g and P_g.

The heat rejected at the condenser and absorber is given by:

$$Q_c = m_5 (h_5 - h_6)$$
$$Q_a = m_7 h_7 + m_4 h_4 - m_1 h_1 \quad (7)$$

where, m and h are the mass flow rate and enthalpy of corresponding state points. The heat supplied at the generator is obtained from the energy balance around the generator:

$$Q_g = m_3 h_3 + m_5 h_5 - m_2 h_2 \quad (8)$$

At the heat exchanger:

$$\varepsilon = 0.8 = \frac{m_1 (h_2 - h_1)}{m_3 (h_3 - h_3^*)} \quad (9)$$

where, h_3^* = enthalpy of solution for ξ_3 and T_a. The above relation for ε is given by Soo (1958).

The specific circulation flow rate is defined as the ratio of the weak solution flow rate (m_1) to the refrigerant vapor flow rate (m_5), as given by:

$$F = \frac{-\xi_3 + \xi_5}{\xi_1 - \xi_3} = \frac{-\xi_3}{\xi_1 - \xi_3} \quad (10)$$

since $\xi_5 \cong 0$ (relative volatility >> 1). In Equation 10, F is the specific circulation flow rate and ξ is the concentration of the aqueous solution.

Once all state points (1 through 7) are determined, the COP of the system is easily calculated. The coefficient of performance (COP) of the system is defined as:

$$\text{Heating mode : } COP_{heat} = \frac{Q_a + Q_c}{Q_g} \quad (11)$$

$$\text{Cooling mode : } COP_{cool} = \frac{Q_e}{Q_g} \quad (12)$$

where, Q_e, Q_g, Q_c, and Q_a are the heats at the evaporator, generator, condenser and absorber, respectively.

The COP of the AHP system depends upon many factors, such as system configuration, operating temperature range and fluid properties. The results obtained

were compared with those obtained from a heat pump system using water-lithium bromide as the refrigerant-absorbent pair. Data for the aqueous LiBr solution were obtained from the literature (ASHRAE Handbook, 1985). The above equations were solved for a range of temperatures at the generator. Computer codes were developed and the system performance analysis was carried out on a microcomputer. The results obtained were compared with the vapor equilibrium data for assessment of accuracy. The pump work, being negligible, was not included in the calculations for the system performance.

Results and Discussion

The physical and thermodynamic properties of the two new working pairs, a description of the heat pump system and the calculation procedures have been covered to this point. The results of the absorption heat pump modeling with the newly developed working pairs are presented in the following sections.

Heat Pump Performance

The coefficient of performance of the heat pump was calculated for both the heating and cooling modes. The results obtained for water-sulfuric acid and water-magnesium chloride pairs are presented below.

AHP Performance using the Water-Sulfuric Acid Pair

The results obtained with water-sulfuric acid as the working fluid pair are shown in Table 9. For comparison purposes, results of the water-lithium bromide system are shown in Table 10. For the water-sulfuric acid system, the minimum temperature lift is 70K. Below this range, the concentration of the strong solution (ξ_3) is less than that of the weak solution (ξ_1). As a result, the refrigerant mass flow rate (m_5) according to Equation 5 would become negative, which is an impossibility. The material balance around the generator thus determines the minimum possible temperature lift . The water-lithium bromide heat pump system is also considered for the same temperature lift.

The cooling-mode COP of the water-sulfuric acid system as shown in Figure 7, increases from 0.788 at T_g = 373K, to a maximum of 0.805 at T_g = 353K, and then decreases rapidly. For the same range, the COP of the water-lithium bromide system increases from 0.801 at T_g = 373K to 0.817 at T_g = 353K, and then decreases.

For constant T_g, T_c, T_e, and T_a, as the specific circulation rate (F) increases or the difference between concentrations ξ_3 and ξ_1 decreases, the COP of the system decreases. In the present study, the increase or decrease in F does not provide any information about the COP of the system. This is because T_g is not constant. For the water-sulfuric acid pair the specific circulation rate increases rapidly from 4.341 kg/kg of vapor at T_g = 373K to a maximum of 110.6 kg/kg of vapor at T_g = 338K. The increase in F is due to the difference between ξ_3 and ξ_1 as a function of T_g. The change in specific circulation rate as a function of temperature for both systems is plotted in Figure 8.

The maximum cooling mode COP is obtained when Tg is around 353K. The cooling mode COP is the ratio of the heat absorbed at the evaporator to that supplied at the generator. With an assumed constant load, the heat absorbed at the evaporator (Q_e) does not change and, therefore the only variable is the heat supplied to the generator (Q_g). Q_g depends on several factors. As seen from Equation 8, h_2, h_3, m_3, and m_2 are the key parameters that affect Q_g. Q_g decreases as h_3 decreases and h_2 increases. As T_g decreases from 373K to 338K, both h_3 and h_2 decrease. The ratio of h_2 to h_3 is largest at a generator temperature of about 353K; hence the COP is maximum.

A plot of the heating-mode COP as a function of the generator temperature is shown in Figure 9. For the case of water-sulfuric acid, the COP increases from 1.788 at Tg = 373K to 1.805 at Tg = 353K, and then decreases. Similarly, the COP of the water-lithium bromide system increases steadily from 1.801 to 1.817 for the same temperature range. The increase in COP in the former case can be explained by the continuous increase in heat of dilution evolved at the absorber, Q_a. This heat is largely affected by the enthalpy of the weak solution entering the absorber. On the other hand, as the temperature lift decreases, Q_a increases, and hence, overall COP increases.

AHP Performance using the Water-Magnesium Chloride Pair

The performance of water-magnesium chloride as an alternative refrigerant-absorbent pair is summarized in Tables 11 and 12. The temperatures for the performance calculation are T_a=298K, T_e=283K, and T_c=298K. The generator temperature varies from 321K to 315K. The concentration of the strong solution leaving the generator (ξ_3) is greater than that leaving the absorber (ξ_1). This limits the range over which T_g can be varied. The maximum temperature of the generator is limited to 321K, since the generator and condenser pressures must be equal.

Table 11 shows the results obtained using water-magnesium chloride as the working pair. The performance of this pair is compared with those obtained using water-lithium bromide for the same heat pump conditions. The results of the water-lithium bromide pair are shown in Table 12. The cooling COP of both pairs are compared in Figure 10. In the cooling mode, the COP of the water-magnesium chloride pair remains steady at 0.76 over the entire range. The COP using water-lithium bromide decreases slightly from 0.904 to 0.794 for the same range.

Figure 11 shows the comparison of the specific circulation rates. As can be seen, the specific circulation rates increase with decreasing temperature lifts. The sudden increase in F for water-magnesium chloride is due to the appreciable change in mass flow rate at the absorber outlet (m_1). The only disadvantage with higher specific circulation rates is that more solution must be circulated per unit mass of the refrigerant.

The heating mode COP of both pairs are shown in Figure 12. The COP for water-magnesium chloride remains nearly steady at 1.76, while that for water-lithium bromide decreases from 1.904 to 1.794. The water-magnesium chloride COP remains constant because Q_c, Q_a and Q_g do not change appreciably.

Conclusion

The AHP analysis has resulted in the discovery of some interesting features of water-sulfuric acid and water-magnesium chloride as refrigerant-absorbent pairs, as compared to the water-lithium bromide system. These are summarized as follows:

1. The water-sulfuric acid pair can be used as a satisfactory replacement for water-lithium bromide pair in the targeted temperature range.
2. Unlike the water-magnesium chloride and water-lithium bromide pairs, the water-sulfuric acid pair does not undergo crystallization.
3. The corrosiveness and toxicity of sulfuric acid must be taken into consideration in the design of a practical heat pump.
4. At lower temperatures, the performance of the AHP using water-magnesium chloride does not compare well with those obtained using water-lithium bromide.
5. The operating temperature and concentration ranges for the water-magnesium chloride pair are limited by its solubility.
6. The computer codes developed can be used to analyze the performance of an AHP with any refrigerant-absorbent working fluid pair with only slight modifications.

The results of this study should help future researchers to design more efficient absorption heat pumps.

References

Alefeld, G. (1987). What needs to be known about working fluids to calculate coefficients of performance. Heat Pumps: Prospects in Heat Pump Technology and Marketing (Proceedings of the 1987 IEA Heat Pump Conference). Michigan: Lewis Publishers, Inc.

ASHRAE Handbook: 1985 Fundamentals. (1985). Atlanta: American Society of Heating, Refrigerating and Air-Conditioning Engineers, Inc.

Bhatt, M. S., Krishna Murthy, M. V., & Seetharamu, S. (1992). An absorption-compression heat pump with the new working pair R22-NMP. Recent Research in Heat Pump Design, Analysis, and Application, ASME, AES-28, 27-42.

Garimella, S., Christensen, R. N., & Petty, S. E. (1992). Cycle description and performance simulation of a gas-fired hydronically coupled double-effect absorption heat pump system. Recent Research in Heat Pump Design, Analysis, and Application, ASME, AES-28, 7-14.

Kaushik, S. C., Gadhi, S. M. B., Agarwal, R. S., & Kumari, R. (1988). Modeling and simulation studies on single/double-effect absorption cycle using water-multicomponent salt (MCS) mixtures. Solar Energy, 40(5), 431-441.

Lu, D. C., & Lee, C. C. (1991). Heat transfer correlation for condenser design in heat pump. Recent Research in Heat Pump Design, Analysis, and Application, ASME, AES-28, 89-95.

Mansoori, G. A., & Pate, V. (1979). Thermodynamic basis for the choice of working fluids for solar absorption cooling systems. Solar Energy, 22, 483-491.

Mayrath, J. E., & Wood, R. H. (1983). Enthalpy of dilution of aqueous solutions of Na_2SO_4, K_2SO_4, and $MgSO_4$ at 373.15 and 423.65 K and of $MgCl_2$ at 375.15, 423.65, and 472.95 K. Journal of Chemical and Engineering Data, 28, 56-59.

Mel'nik, B. D., & Mel'nikov, E. B. (1970). Technology of inorganic compounds. (Kondor, R., Trans.). Jerusalem: Keter Press. (Original work published in 1968)

Patil, K. R., Tripathi, A. D., Pathak, G., and Katti, S. S. (1991). Thermodynamic properties of aqueous electrolyte solutions. 2. Vapor pressure of aqueous solutions of NaBr, NaI, KCl, KI, RbCl, CsCl, CsI, $MgCl_2$, $CaCl_2$, $CaBr_2$, CaI_2, $SrCl_2$, $SrBr_2$, SrI_2, $BaCl_2$, and $BaBr_2$. Journal of Chemical and Engineering Data, 36(2), 225-230.

Perry, J. H. (Ed.). (1950). Chemical engineers' handbook (3rd ed.). NY: McGraw-Hill Book Company.

Perry, R. H., & Chilton, C. H. (Eds.). (1973). Chemical engineers' handbook (5th ed.). NY: McGraw-Hill Book Company.

Sako, T., Hakuta, T., & Yoshitome, H. (1985). Vapor pressure of binary (H_2O-HCl,-$MgCl_2$, and -$CaCl_2$) and ternary (H_2O-$MgCl_2$-$CaCl_2$) aqueous solutions. Journal of Chemical and Engineering Data, 30(2), 224-228.

Serpente, C. P., Perez-Blanco, H., & Seewald, J. S. (1992). A single effect absorption cooling machine with solution cooled absorber. Recent Research in Heat Pump Design, Analysis, and Application, ASME, AES-28, 1-5.

Smith, J. M., & Van Ness, H. C. (1975). Intoduction to Chemical Engineering Thermodynamics. Tokyo: McGraw-Hill Kogakusha, Ltd.

Snipes, H. P., Manly, C., & Ensor, D. D. (1975). Heats of dilution of aqueous electrolytes: Temperature dependence. Journal of Chemical and Engineering Data, 20(3), 287-291.

Soo, S. L. (1958). Thermodynamics of Engineering Science. NJ: Prentice-Hall.

Stoecker, W. F., & Jones, J. W. (1982). Refrigeration and Air Conditioning. New York: McGraw-Hill Book Company.

Warrier, G. R., Annamalai, S., Nguyen, T., & Lin, C. H. (1993). Water/sulfuric acid as refrigerant/absorbent fluid pair for the absorption heat pump. ASME Winter Annual Meeting.

Table 1

Total Pressure-Temperature-Concentration Correlation for Water-Sulfuric Acid Solution

$$\log P = A(\xi) - \frac{B(\xi)}{T}$$

$$A(\xi) = A_0 + A_1 \xi + A_2 \xi^2 + A_3 \xi^3$$

$$B(\xi) = B_0 + B_1 \xi + B_2 \xi^2 + B_3 \xi^3$$

$$A_0 = 8.895309, A_1 = 0.626003, A_2 = -3.443284, A_3 = 3.828686$$

$$B_0 = 2148.129, B_1 = 1363.297, B_2 = -4540.463, B_3 = 5202.362$$

where,

P = Total vapor pressure, (mm Hg)

T = Temperature of solution, (K) $[273 \le T \le 378]$

ξ = Mass fraction of sulfuric acid $[0.1 \le \xi \le 0.90]$

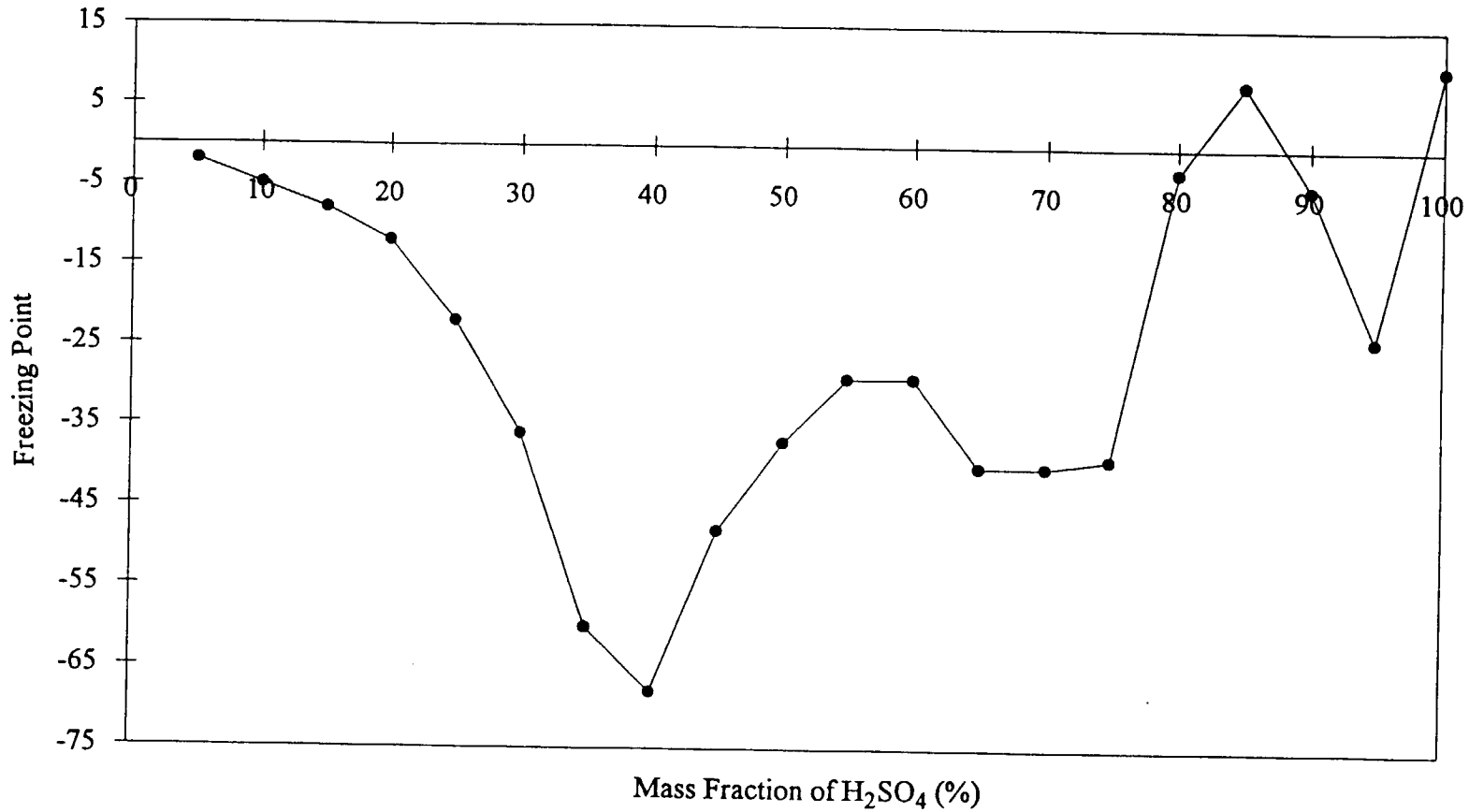

Figure 1

Freezing Points of H_2O-H_2SO_4 Solution at Various Concenrations

Table 2

Relative Volatility Relationship for Water-Sulfuric Acid Solution

$$RV = \frac{y_1 x_2}{y_2 x_1}$$

y_1 = mole fraction of water in vapor phase.
y_2 = mole fraction of sulfuric acid in vapor phase.
x_1 = mole fraction of water in liquid phase.
x_2 = mole fraction of sulfuric acid in liquid phase.

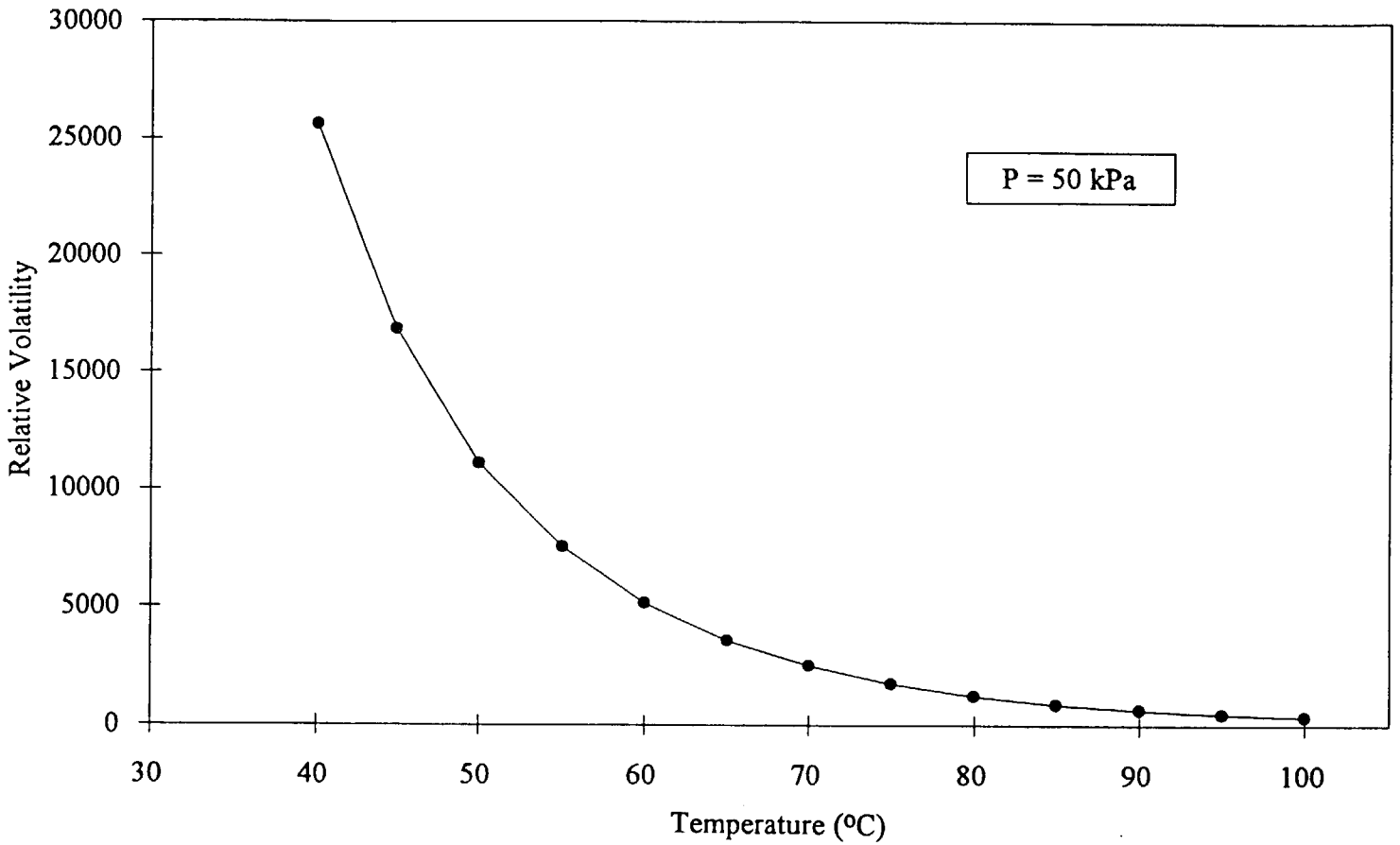

Figure 2

Relative Volatility of H_2O-H_2SO_4 Solution at $P = P_g$

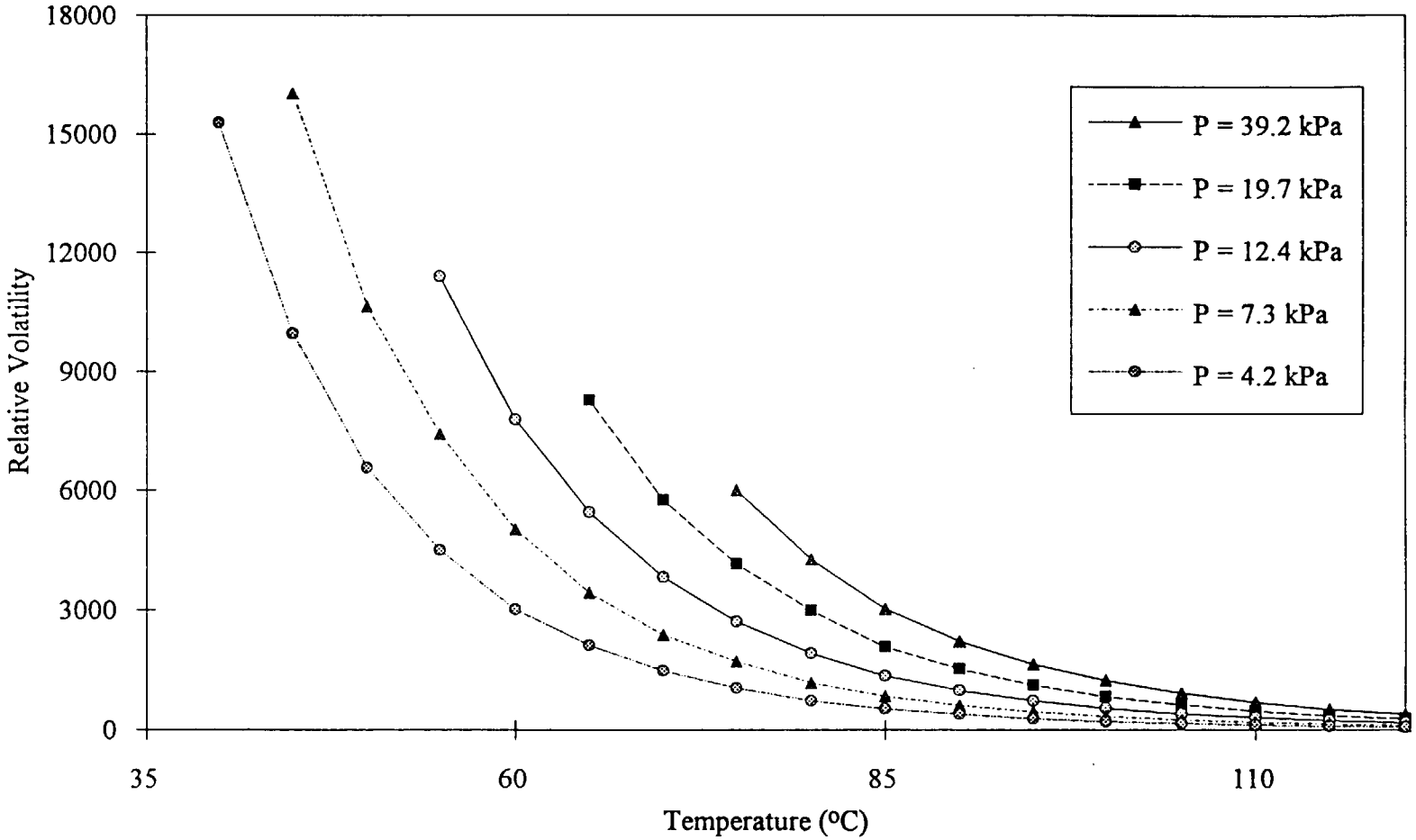

Figure 3

Relative Volatility of H_2O-H_2SO_4 Solution at Various Pressures

Table 3

Enthalpy-Temperature-Concentration Correlation for Water-Sulfuric Acid Solution

$$h[T,\xi] = b_o + b_1\xi + b_2 T + b_3 \xi T + b_4 \xi^2 + b_5 T^2 + b_6 \xi^2 T + b_7 \xi T^2 + b_8 \xi^3 + b_9 T^3$$

$b_0 = -3.746\ E+3$, $b_1 = 403.068$, $b_2 = 28.889$

$b_3 = -3.335$, $b_4 = -964.04$, $b_5 = -0.078$

$b_6 = 1.038$, $b_7 = -4.088\ E-4$, $b_8 = 1.182\ E+3$

$b_9 = 8.11\ E-5$

where,

h = Enthalpy of solution, (kJ / kg)

T = Temperature of solution, (K) $[273 \le T \le 373]$

ξ = Mass fraction of sulfuric acid $[0.20 \le \xi \le 0.80]$

Table 4

Maximum Solubility of Magnesium Chloride as a Function of Solution Temperature

$$S = b_0 + b_1 T + b_2 T^2 + b_3 T^3 + b_4 T^4 + b_5 T^5 + b_6 T^6$$

$b_0 = 0.346,\ b_1 = 5.643E-4,\ b_2 = -2.400E-5$

$b_3 = 9.161E-13,\ b_4 = -1.372E-8,\ b_5 = 9.649E-11$

$b_6 = -2.494E-13$

where,

S = maximum solubility of $MgCl_2$ [weight fraction]

T = solution temperature, (K) $[273 \leq T \leq 413]$

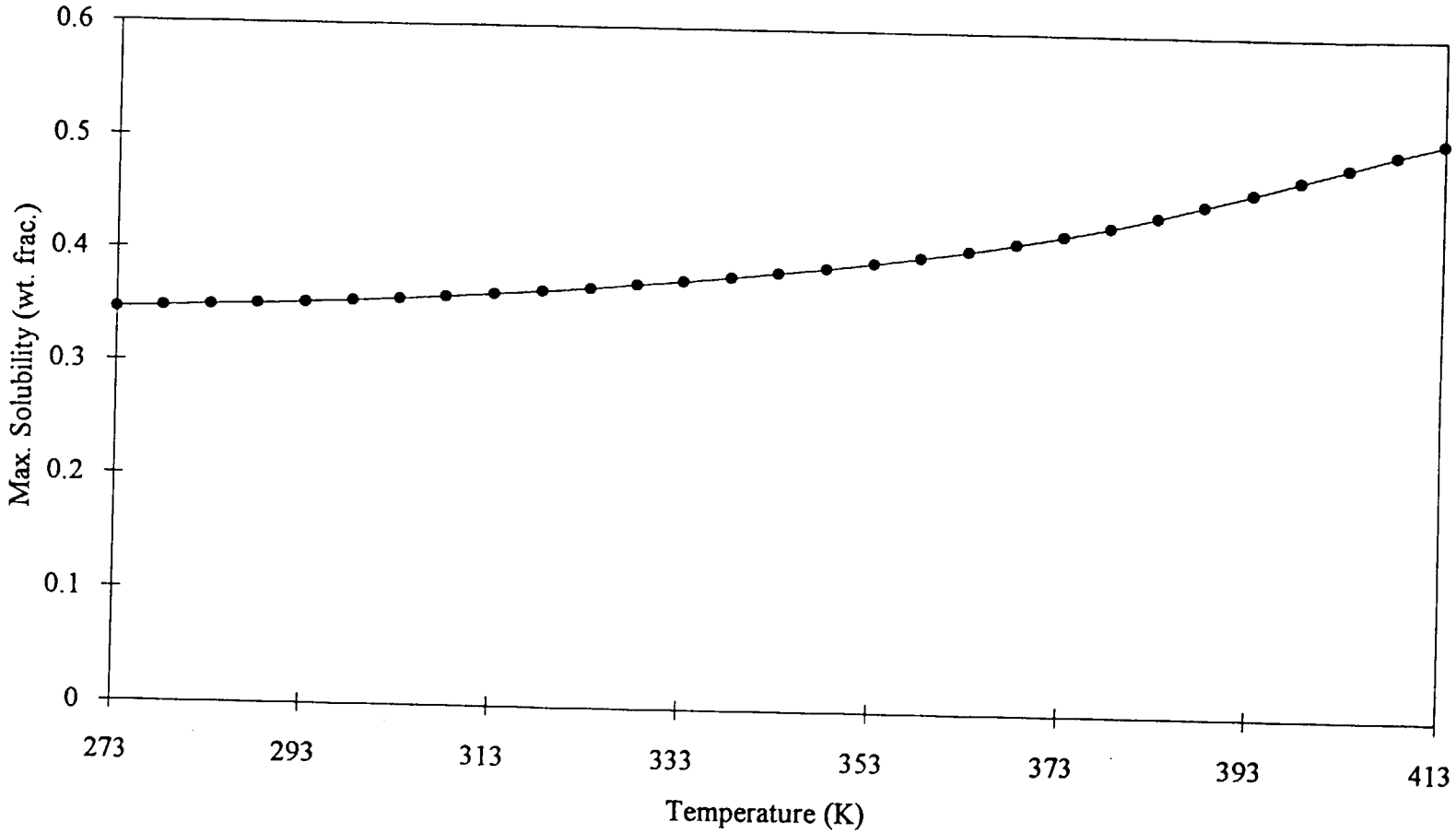

Figure 4

Maximum Solubility of $MgCl_2$ in Solution

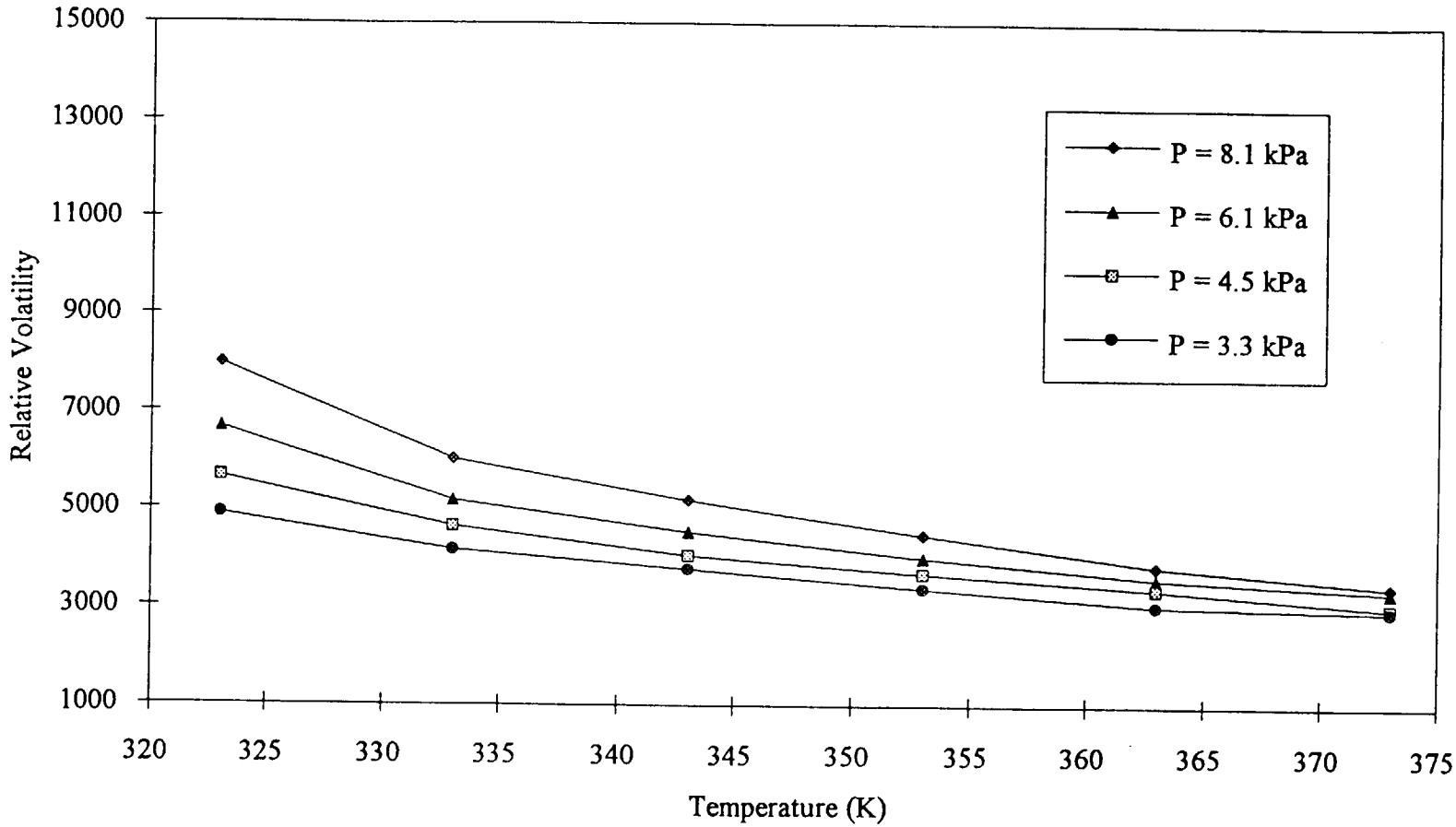

Figure 5

Relative Volatility of H_2O-$MgCl_2$ Solution at Various Pressures

Table 5

Vapor Pressure of Water-Magnesium Chloride Solution
T(K)=[303-343], m(mol/kg)=[0.5-8.6]

$$\log p = A(m) + \frac{B(m)}{T} + \frac{C(m)}{T^2}$$

$$A(m) = A_0 + A_1 m + A_2 m^2 + A_3 m^3$$

$$B(m) = B_0 + B_1 m + B_2 m^2 + B_3 m^3$$

$$C(m) = C_0 + C_1 m + C_2 m^2 + C_3 m^3$$

$$A_0 = 6.8529260, A_1 = 0.1636174, A_2 = -0.0656395, A_3 = 0.0086453$$

$$B_0 = -1545.4780, B_1 = 0.7887, B_2 = -7.8757, B_3 = -0.1009$$

$$C_0 = -99192.550, C_1 = -23502.530, C_2 = 10382.470, C_3 = -1127.883$$

where,

p = vapor pressure (KPa)

T = solution temperature (K) $[303 \le T \le 343]$

m = molality of electrolyte (mol / kg) $[0.5 \le m \le 8.6]$

Table 6

Vapor pressure of water-magnesium chloride solution
T(K)=[320-400], m(mol/kg)=[1.051-4.104]

$$\log p = A(m) + \frac{B(m)}{T + C}$$

$$A(m) = A_0 + A_1\, m + A_2\, m^2 + A_3\, m^3$$

$$B(m) = B_0 + B_1\, m + B_2\, m^2 + B_3\, m^3$$

$$C = -45.107$$

$$A_0 = 7.09562, A_1 = -5.42893E-2, A_2 = 2.50527E-2, A_3 = -4.02686E-3$$

$$B_0 = -1670.05, B_1 = 10.5198, B_2 = -9.38085, B_3 = 1.07931$$

where,

p = vapor pressure (kPa)

T = temperature (K) $[320 \le T \le 400]$

m = molality of electrolyte (mol / kg) $[1.051 \le m \le 4.104]$

Table 7

Enthalpy of Water-Magnesium Chloride Solution
T(°C)=[25-80] m(mol/kg)=[0.005-2.0]

$$h = c_0 + c_1 T + c_2 m + c_3 T m + c_4 T^2 + c_5 m^2 + c_6 T^2 m^2$$
$$c_7 T^2 m + c_8 T m^2 + c_9 T^3 m + c_{10} T m^3 + c_{11} T^3 m^2$$

$c_0 = 5.838612, c_1 = 0.044056, c_2 = 3.274185$

$c_3 = 0.613119, c_4 = 0.001166, c_5 = 2.264470$

$c_6 = 8.642301E-4, c_7 = -1.680469E-4, c_8 = 0.322342$

$c = 1.699305E-5, c = 0.045694, c = 2.415471E-6$

where,

h = specific enthalpy of solution (cal / mol)

T = solution temperature (°C) $[25 \le T \le 80]$

m = molality of electrolyte (mol / kg) $[0.005 \le m \le 2.0]$

Table 8

Enthalpy of Water-Magnesium Chloride Solution
T(K)=[373-473], m(mol/kg)=[0.1-3.6]

$$h = A(T)\,m^{\frac{1}{2}} + B(T)\,m + C(T)\,m^{\frac{3}{2}} + D(T)\,m^{2} + E(T)\,m^{\frac{5}{2}} + F(T)\,m^{3}$$

$$A(T) = A_0 + A_1 T + A_2 T^2$$

$$B(T) = B_0 + B_1 T + B_2 T^2$$

$$C(T) = C_0 + C_1 T + C_2 T^2$$

$$D(T) = D_0 + D_1 T + D_2 T^2$$

$$E(T) = E_0 + E_1 T + E_2 T^2$$

$$F(T) = F_0 + F_1 T + F_2 T^2$$

$A_0 = 323.64946, A_1 = -1.85086, A_2 = 0.00284$

$B_0 = -299.96794, B_1 = 0.91114, B_2 = -0.00325$

$C_0 = 223.40526, C_1 = -1.70142, C_2 = 0.00325$

$D_0 = -125.65092, D_1 = 1.12735, D_2 = -0.00226$

$E_0 = 22.30547, E_1 = -0.33572, E_2 = 7.68004E-4$

$F_0 = 4.53126, F_1 = 0.01766, F_2 = -7.98914E-5$

where,

h = specific enthalpy of solution (cal / mol)

T = solution temperature (K) $[373 \le T \le 473]$

m = molality of electrolyte (mol / kg) $[0.1 \le m \le 3.6]$

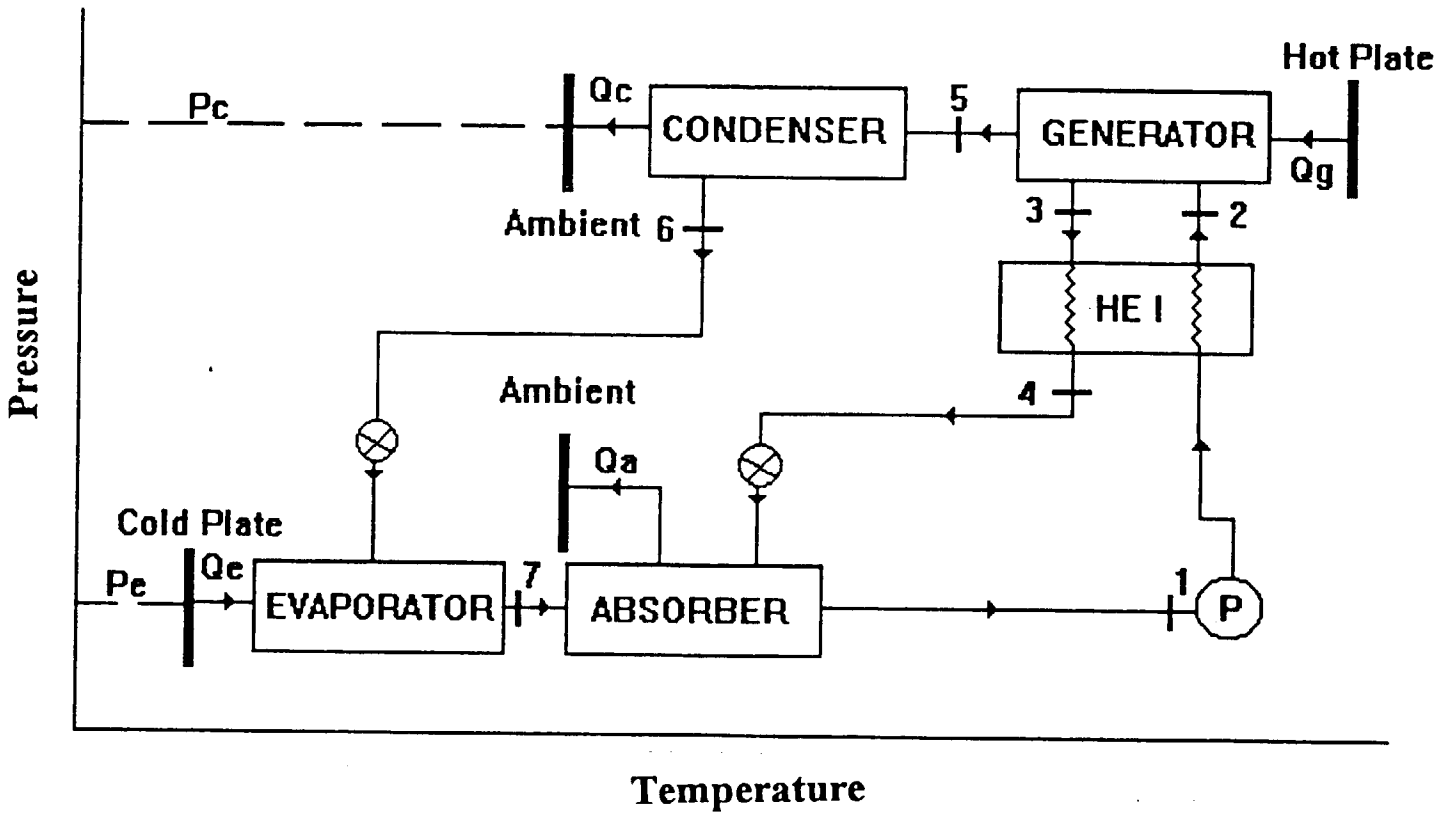

Figure 6

Absorption Heat Pump Configuration

Table 9

Water-Sulfuric Acid System
[m_S = 0.001493 kg/s, ε = 0.8]

T_g K	Q_g kW	Q_c kW	Q_a kW	Q_e kW	ξ_1 mass frac.	ξ_3 mass frac.	$m_3(10^3)$ kg/s	F kg sol/ kg vap.	COP cool	COP heat
373	4.46	3.74	4.23	3.52	0.548	0.712	4.989	4.341	0.788	1.788
368	4.43	3.73	4.22	3.52	0.548	0.695	5.565	4.728	0.793	1.793
363	4.40	3.72	4.20	3.52	0.548	0.677	6.342	5.248	0.798	1.798
358	4.38	3.71	4.19	3.52	0.548	0.657	7.506	6.028	0.802	1.802
353	4.37	3.69	4.19	3.52	0.548	0.636	9.297	7.227	0.805	1.805
348	4.38	3.68	4.22	3.52	0.548	0.612	12.783	9.563	0.802	1.802
343	4.49	3.67	4.33	3.52	0.548	0.585	22.111	15.811	0.783	1.783
338	6.79	3.66	6.65	3.52	0.548	0.553	163.625	110.600	0.517	1.517

Table 10

Water-Lithium Bromide system
[m_5 = 0.001493 kg/s, ε = 0.8]

T_g K	Q_g kW	Q_c kW	Q_a kW	Q_e kW	ξ_1 mass frac.	ξ_3 mass frac.	$m_3(10^3)$ kg/s	F kg sol/ kg vap.	COP cool	COP heat
373	4.39	3.74	4.16	3.52	0.508	0.664	4.860	4.256	0.801	1.801
368	4.37	3.73	4.15	3.52	0.508	0.648	5.417	4.628	0.805	1.805
363	4.35	3.72	4.14	3.52	0.508	0.630	6.216	5.164	0.809	1.809
358	4.32	3.70	4.13	3.52	0.508	0.612	7.292	5.885	0.814	1.814
353	4.31	3.69	4.13	3.52	0.508	0.590	9.249	7.195	0.817	1.817
348	4.32	3.68	4.15	3.52	0.508	0.565	13.305	9.912	0.815	1.815
343	4.42	3.67	4.26	3.52	0.508	0.540	23.700	16.875	0.796	1.796
338	7.80	3.66	7.66	3.52	0.508	0.511	252.802	170.333	0.451	1.451

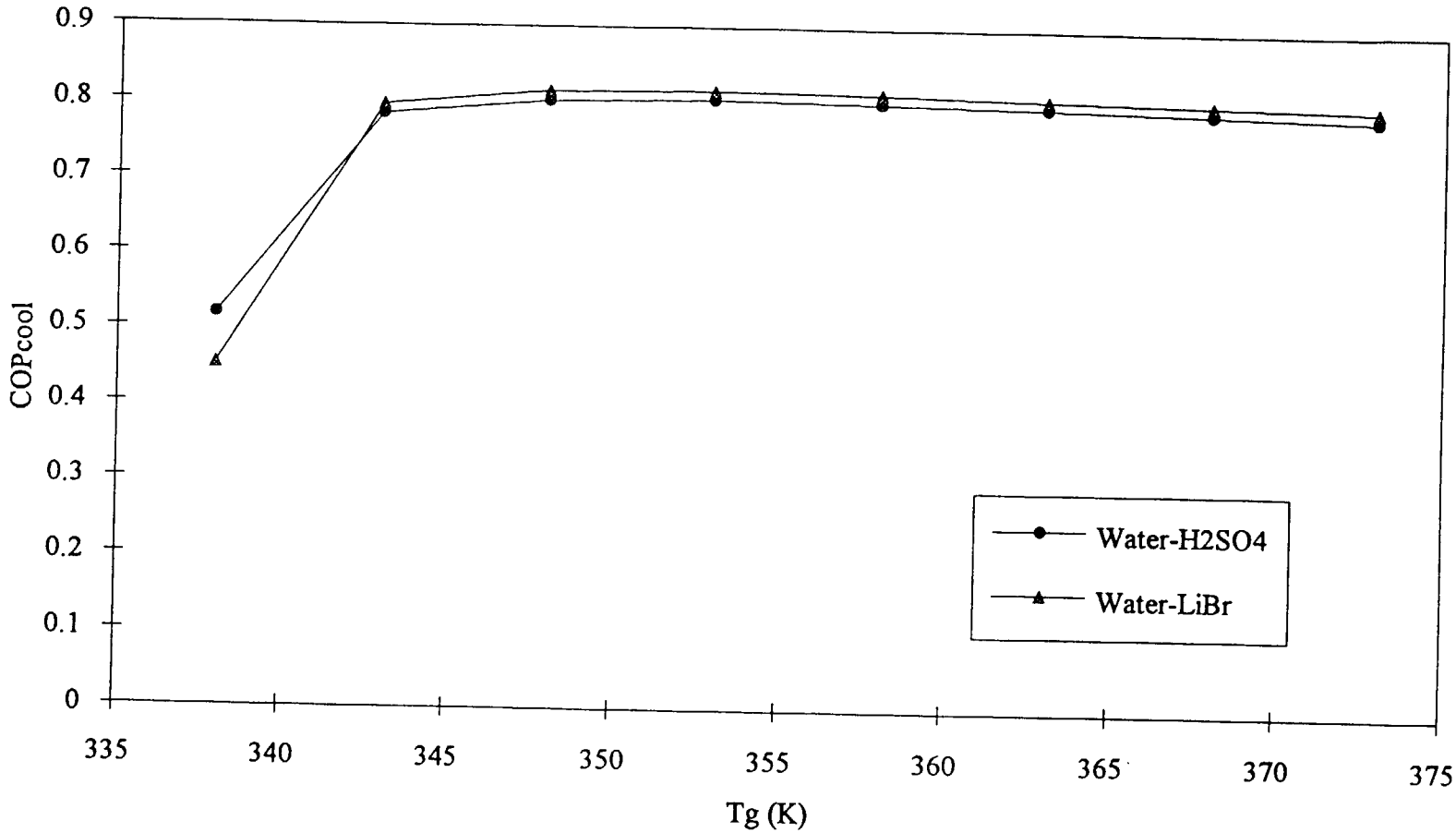

Figure 7

Cooling Mode COP Comparison [H_2O-H_2SO_4 Vs. H_2O-LiBr]

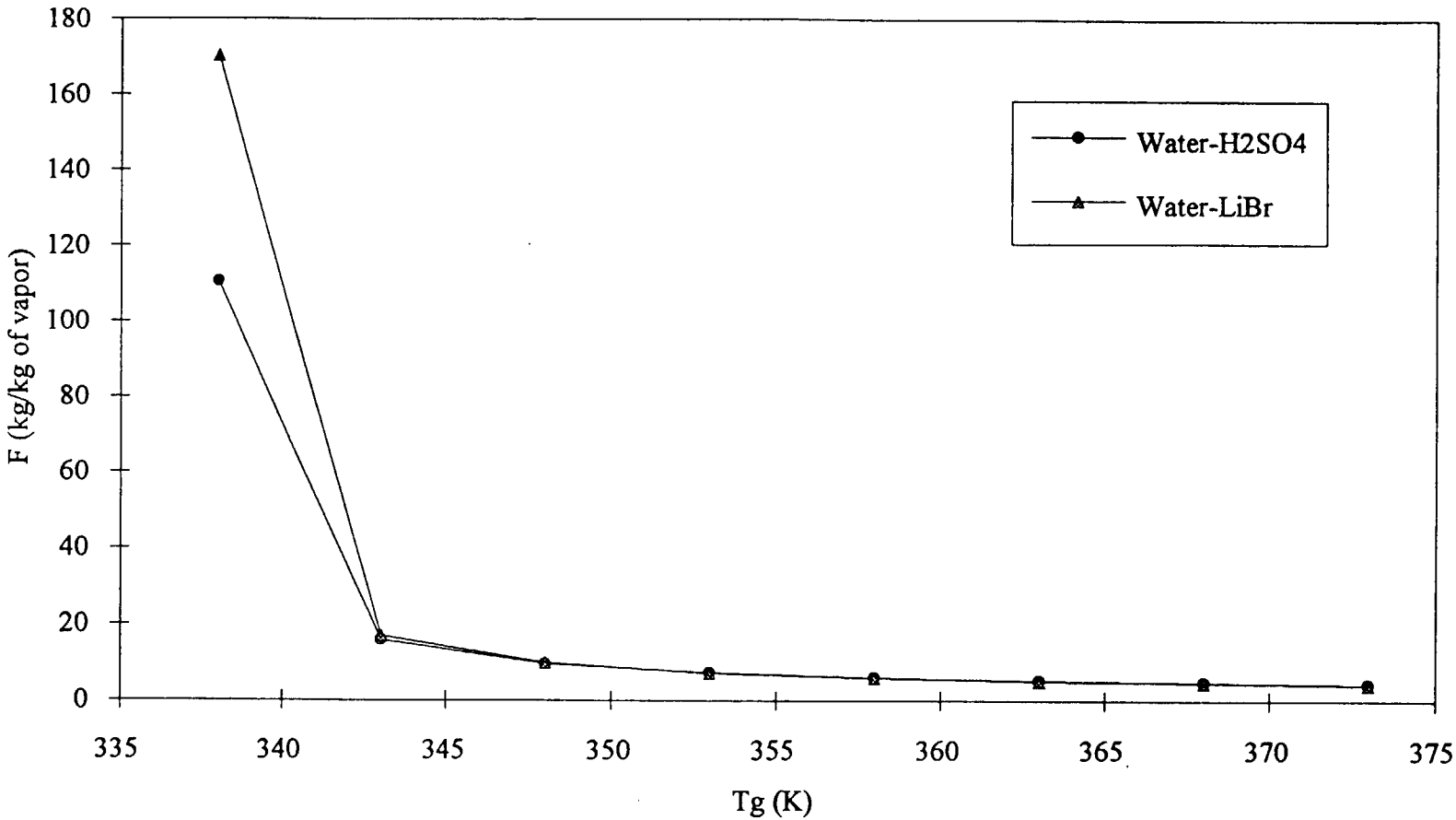

Figure 8

Variation in Specific Circulation Rates with Temperature
[H_2O-H_2SO_4 Vs. H_2O-LiBr]

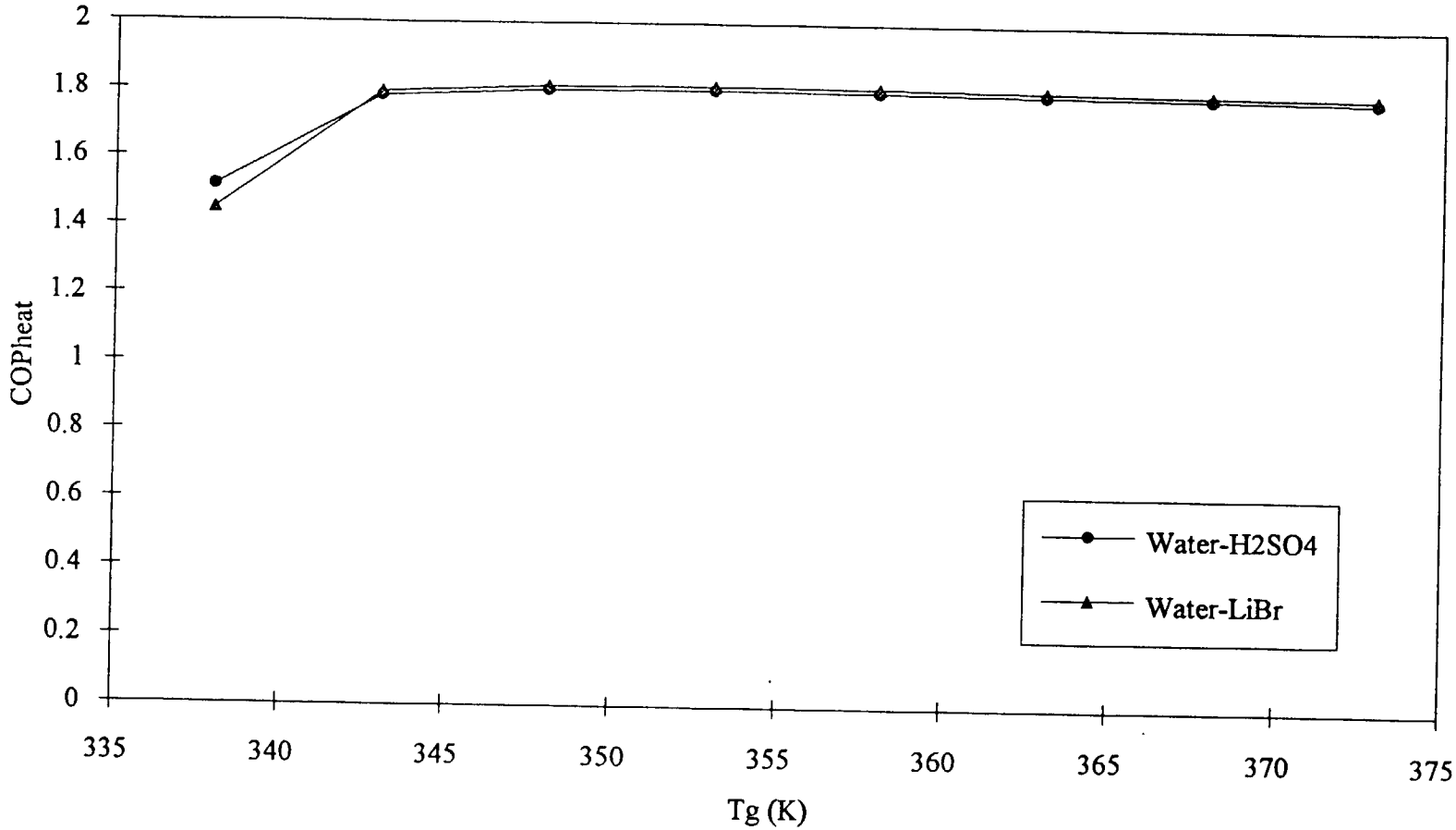

Figure 9

Heating Mode COP Comparison [H_2O-H_2SO_4 Vs. H_2O-LiBr]

Table 11

Water-Magnesium Chloride System
[m_5 = 0.00149 kg/s, ε = 0.8]

T_g K	Q_g kW	Q_c kW	Q_a kW	Q_e kW	ξ_1 mass frac.	ξ_3 mass frac.	$m_3(10^3)$ kg/s	F kg sol/ kg vap.	COP cool	COP heat
321	4.57	4.27	3.82	3.52	0.337	0.367	16.126	12.091	0.769	1.769
320	4.57	4.27	3.82	3.52	0.337	0.363	18.746	13.893	0.769	1.769
319	4.57	4.27	3.82	3.52	0.337	0.358	22.704	16.615	0.770	1.770
318	4.57	4.27	3.82	3.52	0.337	0.353	28.951	20.911	0.769	1.769
317	4.58	4.26	3.83	3.52	0.337	0.349	40.773	29.042	0.768	1.768
316	4.56	4.26	3.88	3.52	0.337	0.343	71.952	50.485	0.761	1.761
315	5.03	4.26	4.29	3.52	0.337	0.338	354.547	244.871	0.699	1.699

Table 12

Water-Lithium Bromide System (II)
[m_5 = 0.00149 kg/s, ε = 0.8]

T_g K	Q_g kW	Q_c kW	Q_a kW	Q_e kW	ξ_1 mass frac.	ξ_3 mass frac.	$m_3(10^3)$ kg/s	F kg sol/ kg vap.	COP cool	COP heat
321	3.88	3.61	3.79	3.52	0.455	0.508	12.483	9.585	0.904	1.904
320	3.89	3.61	3.80	3.52	0.455	0.500	14.702	11.111	0.903	1.903
319	3.90	3.61	3.81	3.52	0.455	0.494	16.963	12.666	0.902	1.902
318	3.96	3.60	3.87	3.52	0.455	0.480	26.463	19.200	0.887	1.887
317	4.00	3.60	3.91	3.52	0.455	0.475	33.079	23.750	0.879	1.879
316	4.07	3.59	3.98	3.52	0.455	0.470	44.105	31.333	0.864	1.864
315	4.43	3.59	4.35	3.52	0.455	4.462	94.511	66.000	0.794	1.794

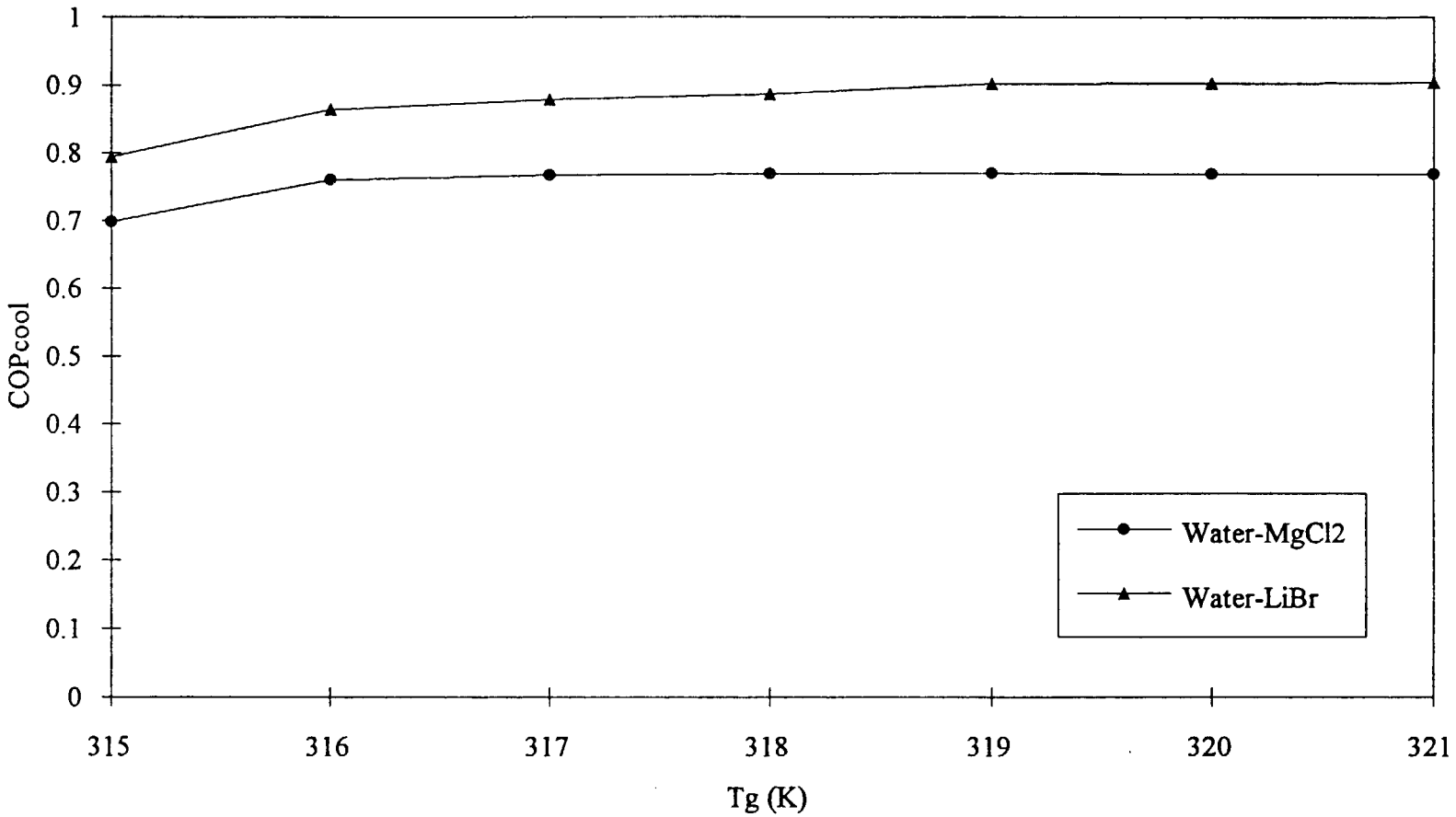

Figure 10

Cooling Mode COP Comparison [H_2O-$MgCl_2$ Vs. H_2O-LiBr]

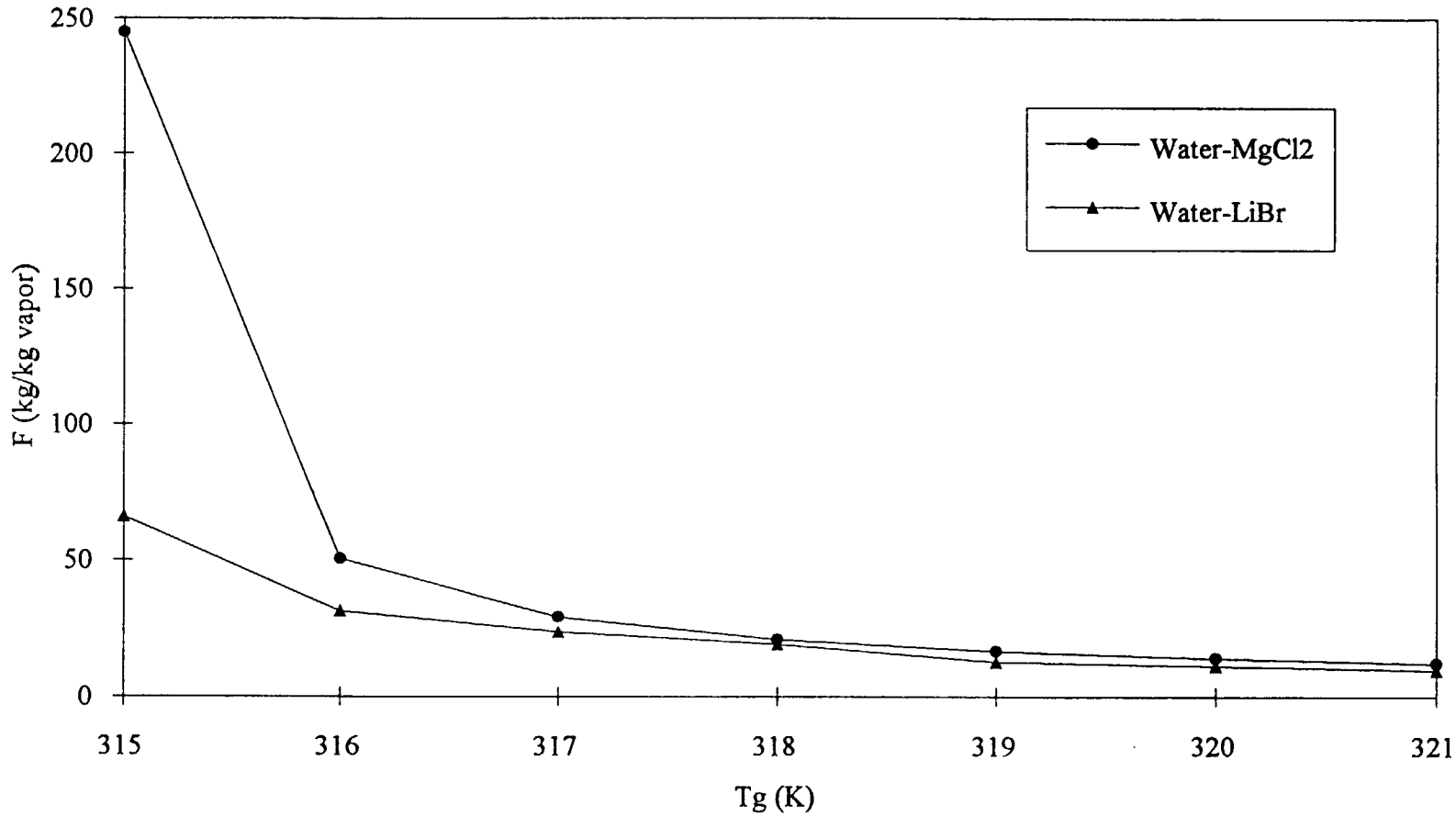

Figure 11

Variation in Specific Circulation Rates with Temperature
[H_2O-$MgCl_2$ Vs. H_2O-LiBr]

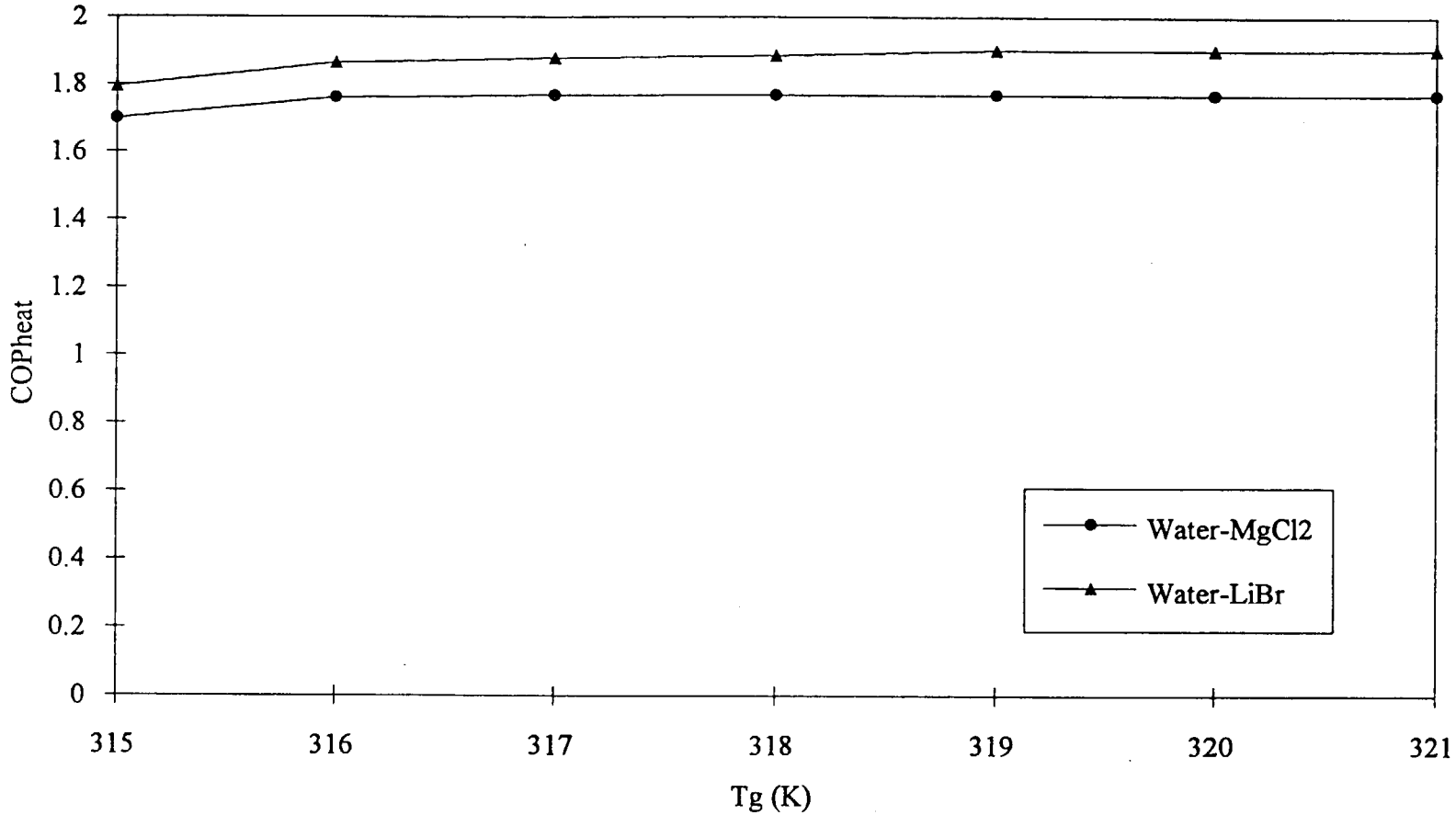

Figure 12

Heating Mode COP Comparison [H_2O-$MgCl_2$ Vs. H_20-LiBr]

Section II

Design of an ElectroHydrodynamic Pump for the Absorption Heat Pump

Design of an ElectroHydrodynamic Pump for the Absorption Heat Pump

Introduction

Several thermal control techniques have been developed for thermal transport and heat rejection in space applications (Kerrebrock, 1986). One method is the absorption-cycle heat pump system. It is generally understood that the absorption heat pump offers significant benefits in terms of mass and complexity reduction of the radiator area, tighter thermal control, and relatively high efficiency. One essential component of the absorption heat pump is a highly reliable pump which is needed to circulate the working fluids. However, major problems limiting the reliability of currently used pumps include wear in the bearings, seals, and in moving parts of the pump. The electrohydrodynamic (EHD) pump is an innovative technology which, through proper development, can provide a solution to this problem.

As early as 1937, J. Hartman and F. Lazarus investigated the EHD flow of mercury between two flat plates assumed infinite in two dimensions (Samaras, 1962). This fluid flow arrangement, known as Hartman-Poiseuille flow, was used in the theoretical development of C. Beal (1967) and J. Melcher (1981). Since the work of Hartman and Lazarus, several types of EHD pumps have been studied (Baker, 1987), but the most appropriate type of EHD pump for aqueous fluids to date is a conduction, or direct-current Faraday type. Also called simply an electromagnetic, or "EM" pump, this type works on the principle of current flow across the fluid perpendicular to an external magnetic field. A resultant body force is exerted on the fluid in a direction mutually perpendicular to the current and to the magnetic field in the sense of a left-handed coordinate system.

Liquid metal EM pumps based on this principle have been available since the early 1950's and are used primarily in nuclear reactor cooling facilities. Pumps of this type have been built for volumetric capacities as high as 3500 m^3/hour and for heads approaching 2.4×10^5 Pa (Andrev, 1981).

Investigations are currently being conducted by others on the use of electrohydrodynamic pump for sea water thrusters (Doss, 1992). Also, this unique pump is under investigation by the U.S. Navy for the development of a silent submarine propulsion system (Swallom, Sadovnik, Gibbs, Gurol, Nguyen, van den Bergh & Hugo, 1991).

The EHD pump is considered to be a reliable means of circulating the working fluid in a heat pump system because it has no moving parts, seals, or bearings. In a pump of this type, the pumping force for moving the fluid does not originate from a piston, diaphragm, or impeller. Instead, the force is exerted directly on the fluid. The EHD pump, therefore, offers great promise for application in an absorption heat pump system. Furthermore, the added feature of being able to repair or service these devices without breaking the fluid circuit makes this pump more attractive than conventional pumps.

Theoretical Modeling of an EHD Pump

A continuum model is used to describe the characteristics of the EHD pump, according to the following assumptions:

1. Incompressible, viscous, steady, and fully developed flow.
2. Uniform electromagnetic field applied in a direction perpendicular to the flow.

The physical configuration is illustrated in Figure 1. The governing equations for the fluid, in normalized form (Melcher, 1981) are as follows:

$$\nabla \cdot \vec{H} = 0 \tag{1}$$

$$\nabla \times \vec{E} = -\frac{\partial \vec{H}}{\partial t} \tag{2}$$

$$\nabla \times \vec{H} = \frac{\tau_m}{\tau} \sigma(\vec{E} \times \vec{V} \times \vec{H}) \tag{3}$$

$$\frac{\partial \vec{V}}{\partial t} + \vec{V} \cdot \nabla \vec{V} + \nabla P = \frac{\tau_m}{\tau_{MI}} \frac{\tau}{\tau_{MI}} (\vec{E} + \vec{V} \times \vec{H}) \times \vec{H} + \frac{\tau}{\tau_v} \nabla^2 \vec{V} \tag{4}$$

$$\nabla \cdot \vec{V} = 0, \tag{5}$$

where, $\vec{H}$, $\vec{E}$, $\vec{V}$, P, and t are electric field intensity, magnetic field intensity, fluid velocity, fluid pressure, and time, respectively. The characteristic times:

$$\tau = \frac{l}{U}, \tau_v = \frac{rl^2}{\eta} \tag{6}$$

$$\tau_m = \sigma_o \mu_o l^2, \tau_{MI} = \sqrt{\rho l^2 / \mu H^2} \tag{7}$$

are, respectively, the transport time, viscous diffusion time, magnetic diffusion time, and the magneto-inertial time. l is the characteristic length, U is the typical material velocity, ρ is the fluid density, and η is the fluid viscosity. It is assumed that the fluid is an ohmic conductor with characteristic conductivity of σ_o and essentially the permeability of free space, μ_o.

In typical laboratory experimentation involving the EHD flow of electrolytes, liquid metals, or plasmas, the magnetic diffusion times are short compared to the time of interest (e.g., $\tau_m << \tau$). Hence, the magnetic Reynolds number ($Re_m = \tau_m/\tau$) plays almost no role in most parts of the flow regime. It is, therefore, appropriate to assume that the induced currents on the right-hand side of Equation 3 are negligible. The magnetic field is imposed by means of currents in the external windings. With the above assumptions, the governing equations are reduced to:

$$\nabla \times \vec{E} = -\frac{\partial \vec{H}}{\partial t} \tag{8}$$

$$\nabla \cdot \vec{J} = 0; \quad \vec{J} = \sigma(\vec{E} + \vec{V} \times \mu_o \vec{H}) \tag{9}$$

$$\rho\left(\frac{\partial \vec{V}}{\partial t} + (\vec{V} \cdot \nabla)\vec{V}\right) + \nabla P = \vec{J} \times \mu_o \vec{H} + \eta \nabla^2 \vec{V} \tag{10}$$

Locally, the axial variations of electric field and current density are assumed to be negligible in comparison with their variations perpendicular to the flow. This assumption may not be accurate when strong variations exist in the magnetic and/or velocity flow field, or when abrupt changes in the boundary conditions occur, as may happen near the pump entrance and exit. However, this analysis is limited to the steady and fully developed section of the flow.

For the task of finding a two-dimensional, steady-flow solution, Equation 10 reduces to

$$\frac{\partial^2 V_y}{\partial x^2} + \frac{\partial^2 V_y}{\partial z^2} - \frac{\sigma(\mu_o H_o)^2 V_y}{\eta} = -\frac{\mu_o \sigma H_o}{\eta} E_z + \frac{1}{\eta}\frac{dP}{dy}. \tag{11}$$

The boundary conditions of this flow require that the velocity of the fluid be zero at the fluid/wall interface. The volumetric flow rate Q is calculated from:

$$Q = \int_{A_c} V_y dA_c \tag{12}$$

where A_C is the cross-sectional area of the pump.

The electrical power applied to the pump (P_{elec}) is obtained from

$$P_{elec} = \int_{\forall} (\vec{J} \cdot \vec{E}) d\forall, \tag{13}$$

where $\forall$ is the active volume of the pump. Since some part of the electrical power is consumed in Joule heating, the mechanical power delivered to the fluid is, thus lower than the electrical power applied to the pump. The power imparted on the fluid (P_{fluid}) can be determined from

$$P_{fluid} = \int_{\forall} (\vec{F} \cdot \vec{V}_y) d\forall, \tag{14}$$

where $\vec{F}$ is the Lorentz force defined as $\vec{F} = (\vec{J} \times \vec{B})$. The actual power produced by the pump (P_{out}) is calculated from:

$$P_{out} = Q \cdot \Delta P, \tag{15}$$

where ΔP is the differential pressure across the pump. The actual power produced by the pump is lower than the power imparted on the fluid due to the fact that some of this power is dissipated as internal viscous loss.

Three different types of efficiency can be defined to provide an insight into the behavior of the pump. They are:

1. Electrical efficiency, defined as:

$$\eta_{elec} = \frac{P_{fluid}}{P_{elec}} = \frac{\int_{\forall} (\vec{F} \cdot \vec{V}) d\forall}{\int_{\forall} (\vec{J} \cdot \vec{E}) d\forall} \tag{16}$$

2. Internal efficiency, defined as:

$$\eta_{int} = \frac{P_{out}}{P_{fluid}} = \frac{Q \cdot \Delta P}{\int_{\forall} (\vec{F} \cdot \vec{V}_y) d\forall} \tag{17}$$

3. Overall efficiency, defined as:

$$\eta_{over} = \frac{P_{out}}{P_{elec}} = \frac{Q \cdot \Delta P}{\int_{\forall} (\vec{J} \cdot \vec{E}) d\forall} = \eta_{int} \cdot \eta_{elec} \qquad (18)$$

These three efficiencies are discussed in detail in later sections.

Numerical Method

Referring to Equation 11,

$$\frac{\partial^2 V_y}{\partial x^2} + \frac{\partial^2 V_y}{\partial z^2} - \frac{\sigma(\mu_o H_o)^2 V_y}{\eta} = -\frac{\mu_o \sigma H_o}{\eta} E_z + \frac{1}{\eta}\frac{dP}{dy}, \qquad (11)$$

ı with Dirichlet boundary

face.). This equation can

(12)

technique is developed in

l/2, and z = -w/2 to w/2,

ıd, the finite difference

$h^2 k_2$), (13)

l is then utilized with this

iterations required to

ly reduced. The algebraic

$$\bar{V}_{i,j}^{<k>} = (1 - \omega)\bar{V}_{i,j}^{<k-1>} + \omega\bar{V}_{i,j}^{<k>} \tag{14}$$

and $$V_{i,j}^{<k>} = \frac{1}{4 + h^2k_1}(V_{i+1,j}^{<k-1>} + V_{i-1,j}^{<k>} + V_{i,j+1}^{<k-1>} + V_{i,j-1}^{<k>} - h^2k_2), \tag{15}$$

where:

$V_{i,j}$ is the velocity calculated from Gauss-Seidel iteration at node i, j

$\bar{V}_{i,j}$ is the approximation of V_y by the SOR method at node i, j.

ω is a relaxation parameter.

<k> is the component of the k^{th} iteration.

The optimal value of the relaxation parameter, ω, is found empirically by performing calculations with different values of ω for coarse grids until the optimal value of ω is obtained. With the optimal ω, the corresponding optimal value of ω for finer grids can then be found by applying the following formula (Strikwerda, 1989) :

$$\omega = \frac{2}{1 + Ch} \tag{16}$$

where C is a constant obtained experimentally, and h is a distance between iterative nodes.

A computer program (Appendix B) was written to implement the iterative scheme. Numerical results from this program are then transferred to a graphics software package for graphical presentation.

Experimental Apparatus and Instrumentation

Experiments were performed to verify the theoretical results obtained from modeling the electromagnetic flow. A copper sulfate solution was used as the working fluid for model verification, with properties as shown in Appendix B.

Experimental Apparatus

The experimental apparatus, illustrated in Figure 3, consists of a reservoir, rectangular conduit, EHD pump, manometer, rotameter, and secondary centrifugal pump.

As can be seen from Figure 3, the rectangular conduit carries the fluid from the reservoir to the EHD pump, and is connected by the return conduit (7.875 mm ID). The flow rate was monitored by a rotameter connected to the end of the return conduit. A valve at the rotameter was used to control the flow rate of the system. The secondary centrifugal pump was connected from the reservoir to the rectangular conduit in parallel to the direct connection between the reservoir and the rectangular duct. This secondary pump was used to drain air bubbles from the system during the startup process. Startup and operational procedures are discussed later in this chapter.

The rectangular conduit, with internal dimensions of 6.35 mm by 25.4 mm, was made of Plexiglas. Plexiglas was chosen because, in addition to being a good electrical insulator, it also allows visual observation of the pumping process. The various Plexiglas parts were assembled using dichloroethane solvent.

Two 6.35 mm by 101.60 mm slots were provided on each side of the conduit at the pump section to accommodate the copper electrodes, which were affixed to the Plexiglas conduit with epoxy.

Figure 4 illustrates the EHD pump used for the experiments. The EHD pump envelope is by definition the volume between the electrodes and the magnetic poles. Some

consideration was given to the fact that the theoretical modeling was based on the electromagnetic flow in the fully developed region. The pump section, thus, should be as long as possible to comply with the theoretical model. The length of the pump section was chosen to be 101.6 mm (four times greater than the width of the channel).

The copper electrodes, shown in Figure 4, were connected to the power supply via three #18 AWG insulated wires to ensure even distribution of the electric field across the pump section. The surfaces of the electrodes were sanded and polished before installation in the conduit. A 15 ampere, 0-50 volt DC power supply (Accurate Electronics Co., model PP-1725) was used with the electrodes.

The magnetic circuit was designed to provide a maximum of 0.4 teslar magnetic flux density in the vertical direction across the pump section. The geometry of the steel core and the arrangement of the coil winding were configured to minimize magnetic fringing outside the pump. Figure 5 illustrates the details of the electromagnet used in the test setup.

Since a larger wire requires higher current at lower voltage and vice versa, an analysis (Appendix C) was performed to select the proper wire size for operation at the voltage and current rating of the available power supply. According to the analysis, #18 AWG wire with 840 turns is sufficient for this application.

A 10 ampere, 0-55 volt DC power supply (Epsco Incorporated., model PS-5) was used for the electromagnet power supply. The actual magnetic flux density was measured using a gaussmeter (General Electric, model 416X37). This reading was then used as a standard for the entire set of experiments. Comparison of the calculated and measured magnetic flux density is given in Appendix D.

A manometry system was used to measured the difference between the suction and discharge heads. Two static pressure taps of 2.23 mm diameter at the entrance and exit of

the EHD pump were connected to the manometer tubes (glass tubes of 4.5 mm internal diameter) by 3.175 mm internal diameter flexible plastic tubing.

The flow measurements at high flow rate were acquired using a Dyna VFB-141-BV, 0.5-5 gpm ($31.5 \cdot 10^{-6}$-$315.4 \cdot 10^{-6}$ m^3/s) rotameter. The rotameter was calibrated for the test fluid (Appendix E). To obtain accurate readings at flow rates lower than $31.5 \cdot 10^{-6}$ m^3/s, the flow measurements were made by measuring the total volume collected in a given time interval.

Initially, a pitot tube was installed at the end of the pump to measure the local velocity of the fluid. However, this method was abandoned due to unsatisfactory differential pressure measurement.

Two multimeters (Micronta Electronics Inc., model 22-185A) were used to measure the voltage and current applied to the electromagnet and electrodes before each experiment was performed. Once the experiments were started, the voltage and current readings were then monitored using the voltmeters and ammeters provided with the power supplies.

Experimental Procedure

After apparatus assembly, leak-checking, and instrumentation verification, the experimental system was certified "test-ready," and all was in order to begin the test runs. Before beginning, however, some precautions were taken to assure the integrity of the test data. These are summarized as follows:

1. The valve at the rotameter must be fully opened when the centrifugal pump is turned on in order to prevent hydraulic pressure from building up and rupturing the conduit.

2. Prolonged use of the electromagnet may cause a damage to the magnetic circuit due to high temperatures generated in the interior coils. Thus, coil temperature was

gauged by noting the rising resistance of the magnetic circuit. In this way the resistance of the magnetic circuit was monitored continuously and maintained lower than 6 ohm during the experiments.

3. The resistance across the electrodes must be regularly monitored. If the resistance is higher than the initial value (8.8 ohm), the electrodes must be cleaned. This increase in resistance cross the electrodes is due to the uneven deposition of copper and impurities on the cathode.

After having incorporated the above precautions into the test operation, the following experimental procedure was implemented:

1. The test loop was filled with the test solution. This was done by pouring the test solution into the reservoir until the level of the test solution was approximately 10 cm above the conduit level. The valve at the rotameter was then slowly opened to allow the solution to flow into the conduit. Trapped air inside the conduit was drained by closing the ball valve located near the reservoir and turning on the centrifugal pump to help circulation and to force air to exit the system at the reservoir.

2. The magnetic circuit was energized. Multimeters were used to monitor the current and voltage applied to the electromagnet. The supply source was adjusted until the power necessary to provide the desired flux density was obtained. The power supply was then turned off.

3. The power supply to the electrodes was turned on. The power supply was adjusted until the desired voltage across the electrodes was obtained. Two multimeters were used to monitor the voltage and current supplied to the electrodes during this process. The power supplied was then turned off after the desired power was set.

4. For each position of the valve settings at the manometer (from fully-closed to fully-opened), the magnetic field and the electric field were simultaneously energized. The ball valve at the reservoir was then opened. The differential pressure head across the EHD

pump was measured by the manometer.. The lower surfaces of the suction pressure and the discharge pressure meniscuses formed in the manometer tubes were marked. The height difference was then recorded. The flow rate was also observed directly at the rotameter for high flow rates. For lower flow rates, where the rotameter reading was inaccurate, the time interval required to fill a calibrated container was recorded, and the flow rate was calculated from this data.

5. The experiment was performed for various magnetic flux densities and voltages applied across the electrodes. Table 1 summarizes the various conditions of magnetic flux density and voltage across the electrodes used in the test runs.

Results and Discussion

Numerical results

The following sections discuss the numerical results obtained for the velocity profile, pressure-flow rate relationship, and efficiency of the EHD pump as a function of magnetic flux density and conduction current.

1. Numerical Results for the Velocity Profile

The numerical methods developed earlier have been used to determine the flow characteristics of the EHD pump. The numbers of nodes in the x and z directions were initially chosen to be 11 and 41, respectively. The dependence of the accuracy of the results on the number of nodes chosen was then investigated. It was found that the results varied by less than 1% when a 21 X 81-node configuration was used, and more than 3% for a 5 X 17-node configuration. Hence, the 11 X 41-node configuration was retained for this analysis.

The relaxation factor (ω) is an empirically determined quantity of the calculational process. Since the solution converges rapidly, the relaxation factor can be found directly without using the scaled-down configuration (lesser number of nodes). It was found that the most suitable value of the relaxation factor for the nodal configuration used (11 X 41) was 1.7.

Since the mathematical model has no closed-form solution, verification of the results was accomplished by modifying the two-dimensional finite-difference scheme developed earlier to a one-dimensional model, and then comparing the results obtained with the analytical closed-form solution. Comparison of the numerical and closed-form solutions indicated an error of less than 1%.

An example of the numerical results obtained for the axial, fully-developed velocity profile is shown in Figure 6. The vertical plane indicates the axial component of the velocity (V_y).

The Lorentz force in the axial direction (J_Z X B) acts as the driving force for the pump. This force, however, is not uniform over the entire cross-section of the pump flow area, due to the non-uniform distribution of the current density. It can be seen from Equation 7 that the local current density depends upon the local fluid velocity. For an EHD pump, a higher fluid velocity corresponds to a lower current density. The force acting on the fluid near the walls, where the local velocity is lower, is higher than that at the core of the duct. This increase in the force causes a rapid change in the velocity profile near the walls.

From the above discussion, it appears that two factors, namely, the voltage across the electrodes and the magnetic flux density, are the parameters controlling the characterization of EHD pump performance. Figure 7 (a,b and c) illustrates the resultant velocity profiles for various applied voltages with constant magnetic flux density and pressure. The voltage across the electrodes exhibits a synergistic effect on the velocity profiles as indicated in the figures for voltage variations from 10 V to 20 V. In Figure 8 (a, b and c) , the effect of varying the magnetic flux density is shown. As with the previous case, the velocity profiles intensify as the flux density increases from 0.2 T to 0.4 T.

2. Numerical Results for Pressure-Flow Rate Performance Characteristics

The pressure-flow rate relationship is also of primary interest in characterizing the performance of the pump. A parametric study was performed by varying the differential pressure while the pump power input was held constant. The analysis indicates that the theoretical pressure-flow rate relationship for an EHD pump is similar to that of a conventional centrifugal pump.

Figures 9 illustrates the pressure-flow rate performance characteristic for various magnetic flux densities with constant voltage maintained across the electrodes. As indicated in the figure, an increase in the flux density increases the pump output.

The effect of the voltage applied across the electrodes on the pressure-flow rate performance characteristic is illustrated in Figure 10. As can be seen from this figure, the pump output increases with an increase in the applied voltage. However, it should be noted that the physical properties of the fluid limit the voltage across the electrodes. This limitation is discussed later in this chapter.

3. Numerical Results for Pump Efficiency

Since efficiency is a parameter of primary importance in characterizing the performance of an EHD pump, the efficiency was determined using two different methods.

In the first approach, the effect of magnetic flux density and voltage applied to the electrodes on pump efficiency was investigated while maintaining a constant flow rate. This method is useful in determining the optimal input condition for a given flow rate.

In the second method, the effects of flow rate on pump efficiency were studied for a given voltage and magnetic flux input. This method provides a convenient way of comparing the numerical results with the experimental results. The comparison of the numerical and experimental results are discussed later in this chapter.

i. Effects of Magnetic Flux Density and Voltage Across the Electrodes on EHD Pump Efficiency.

Three different types of efficiencies have been previously discussed. Figure 11 illustrates the effects of the magnetic flux density and the voltage across the electrodes on the internal efficiency of the EHD pump for a constant volumetric flow rate. As can be seen from Figure 11, an increase in either the magnetic flux density or the voltage across the electrodes increases the internal efficiency of the pump. This is because, at constant

flow rate, the viscous loss in the fluid is almost constant. For a higher magnetic flux density or an increase in the voltage across the electrodes, the pump power input increases while the losses remain nearly constant. This improves the internal efficiency of the EHD pump.

The effects of varying magnetic flux density and voltage across the electrodes on the electrical efficiency are shown in Figure 12. As indicated in the Figure, high electrical efficiency can be obtained using higher magnetic flux density and lower voltage across the electrodes. This phenomenon can be explained by considering local electrical efficiency given as:

$$\left[\eta_{elec}\right]_{local} = \frac{B \cdot V_y}{E} = \frac{B \cdot V_y}{v/w} \qquad (17)$$

where B is the magnetic flux density; V_y the local velocity of the fluid and E the electric field strength. E is again defined as the ratio of the voltage across the electrodes to the width of the pump ($E = v/w$). For a given flow rate, the local fluid velocity is almost constant. The local electrical efficiency thus depends on the ratio of the flux density to the voltage across the electrodes.

It should be noted that the local electrical efficiency is not uniform over the entire cross-sectional area of the pump. Equation 17 indicates that the local electrical efficiency depends on the local fluid velocity. The local electrical efficiency of the fluid at the core is, therefore, higher than that near the walls. Figure 13 illustrates the overall efficiency of the pump. The overall efficiency of the pump is the product of the integrated electrical and internal efficiencies. An increase in the magnetic flux density will increase both the electrical and internal efficiencies, therefore increasing the overall efficiency of the EHD pump. An increase in the voltage across the electrodes will increase the internal efficiency but decrease the electrical efficiency. The maximum overall efficiency of the pump is

therefore dependent on the particular pump configuration, namely, flow rate, voltage across the electrodes, and magnetic flux density.

ii. Effect of Flow Rate on EHD Pump Efficiency

The effect of volumetric flow rate on the efficiency of the pump is another important characteristic which must be understood to properly characterize pump performance. A parametric study was conducted by varying both the volumetric flow rate and the pump power input. Figures 14 (a and b) illustrate the relationship between internal efficiency and volumetric flow rate for various input conditions. As can be seen from the figure, the internal efficiency decreases linearly from its maximum (no-flow condition) to zero (maximum flow rate). This is due to the fact that the viscous loss of the fluid is directly proportional to the volumetric flow rate. For the maximum flow rate, all of the mechanical power delivered to the fluid is used to overcome the viscous loss. Therefore, no useful output is produced. The internal efficiency of the pump is thus zero for the maximum delivery condition. Since the viscous loss converges to zero as the flow rate approaches the no-flow condition, the internal efficiency is at its maximum.

Figure 15 (a and b) shows the electrical efficiency-volumetric flow rate relationship for the EHD pump. Increasing the flow rate results in an increase in the mechanical power delivered to the fluid but does not change the input power to the system. Therefore, the electrical efficiency increases as the flow rate increases.

In Figure 15a, it is important to note that as the magnetic flux density increases, the slopes of the electrical efficiency-flow rate curves (each at a constant B) increase. But as seen from Figure 15b, the slopes of the electrical efficiency-flow rate curves (each at a constant v) decrease as the applied voltage across the electrodes increases.

Overall efficiency curves for the EHD pump are shown in Figures 16 (a and b). The overall efficiency as defined earlier is the product of the internal and electrical efficiencies. Figures 16a shows that for a given voltage across the electrodes, the overall

efficiency increases from zero to a maximum and then decreases to zero as flow rate increases from the no-flow condition to the maximum-flow condition. As the flux density increases, the maximum value of overall efficiency also increases. It should be noted that the maximum values of the overall efficiency occur at higher flow rates when the flux density increases.

Figure 16b shows the theoretical relationship between overall efficiency and flow rate for constant magnetic flux density and varying voltage. For a given value of voltage applied across the electrodes, the overall efficiency increases form zero to its maximum and then decreases to zero as the flow rate increases. As the voltage increases, the maximum value of the overall efficiency obtained remains approximately the same but occurs at higher flow rate values.

Experimental Results

Since repeated attempts to measure the velocity profile yielded unsatisfactory results, the following sections will focus only on the experimental results obtained for the pressure-flow rate relationship and efficiency determinations for the EHD pump.

1. Experimental Results of Pressure-Flow Rate Relationship

The effects of the magnetic flux density and voltage across the electrodes have been discussed in previous sections. Figures 17 to 28 show the comparison between the experimental and theoretical pressure-flow rate relationship for various input conditions. The various input conditions are summarized in Table 2.

As seen from Figures 17 to 28, the experimental values agree well with the predictions for low flow rates. At higher flow rates, the experimentally measured values were lower than the predicted values. The aberrations observed are due to the assumption that the flow is fully developed. Since the fluid at low flow rate tends to become fully

developed faster than the fluid at high flow rate, the theoretically predicted values are more accurate at the low flow rates than at the high flow rates.

The difference in the measured and predicted pressure at high flow rates may also be due to the non-linear losses in the system. These non-linear losses are the those caused by local turbulence.

For higher values of applied voltage across the electrodes, the efficiencies obtained experimentally were lower than the predicted values. The variations observed were due to increasing current fringing at higher voltages. This resulted in the decrease of the useful conduction current in the system.

Physical properties of the working fluid also limit the applied voltage. High voltage applied across the electrodes caused an uneven deposition of copper on the cathode, thus increasing the electrode surface resistance. This effect degraded the pump power output rapidly. Since this phenomenon is pronounced for applied voltages higher than 20 V, no experiments were performed in this voltage range.

As the magnetic flux density increased, it was expected that the fringing effect would cause variations in the experimental results, in the same manner that current fringing did. However, comparison of experimental and theoretical data does not conclusively substantiate this theory.

2. Experimental Results for Overall Efficiency

Since internal and electrical efficiency could not be directly measured, the overall efficiency was the most important parameter of interest. The theoretical effects that the magnetic flux density, the voltage across the electrodes, and the volumetric flow rate have on the overall efficiency have been discussed previously.

The experimental and theoretical values of overall efficiency are shown in Figures 29 to 40 for the various input conditions. The input conditions are listed in Table 3.

As can be seen from Figures 29 to 40, the experimentally obtained efficiencies agree well with the predicted values at low flow rates. However, the experimental results were lower than the numerical results for higher flow rates. This is due to the fact that the actual differential pressure across the pump is lower than the theoretical value, when the flow rates become higher.

The current fringing effect could also cause the actual overall efficiency to be lower than the theoretically predicted value. As discussed earlier, higher voltage across the electrodes increases the current fringing, thus reducing the power output of the pump. Although theoretically, the magnetic fringing should decrease the pump performance, experimental data does not substantiate this fact.

Conclusions and Recommendations

An investigation of the operational characteristics of an electrohydrodynamic pump was performed in this study. The numerical and experimental results obtained provide an insight into the electrohydrodynamic characteristics of the fluid inside the pump. The results obtained are summarized as follows:

1. The numerical mathematical model developed based on continuum electromechanics provides reasonable results within the limitations of the assumptions made.

2. The operational characteristics of the EHD pump as predicted by the model were found to be similar to those of a conventional centrifugal pump.

3. The predicted overall behavior of the EHD pump is comparable to that of turbomachinery hardware; however, the overall efficiency of the electromagnetic pump is, as predicted, much lower.

4. The pressure-flow rate performance characteristics and overall efficiency of the pump obtained experimentally agree well with the theoretical results.

Although the model developed during this study yielded satisfactory results, better results could be obtained with a more sophisticated model based on a three-dimensional mathematical model.

The small size of the experimental apparatus used in this study caused some inherent limitations in the accuracy of the measured quantities. In the future, these limitations could be eliminated by utilizing a pump of larger capacity.

The electrohydrodynamic pump is very sensitive to fluid properties. Because of this, care must be exercised in selecting the feasible range of operational parameters and appropriate electrode types for a given application. As a recommendation for future

research, it is proposed that additional effort be expended to explore the variety of fluids available, with appropriate electrode combinations, for use in an EHD pump.

Also, as the overall efficiency of the pump is largely dependent on the magnetic flux density, superconductors could be used to improve pump performance.

The development of the EHD pump for circulating the working fluid in the absorption heat pump system can be considered a high-risk, high-payoff application of advanced technology to provide revolutionary improvement in reliability and maintainability of the heat pump system. The results of the present effort should help researchers understand the fundamental performance characteristics of this type of pump in order to develop an improved electrohydrodynamic pump for future applications.

References

Ames, W. F. (1977). Numerical Methods for Partial Differential Equations. NY: Academic Press.

Adreev, A. M. (1981). The TsLIN - 3/3500 electromagnetic pump. Magnetohydrodynamics, 24(1), 55-61.

Baker, R. S. (1987). Electromagnetic Pump Technology. NY: Elsevier Press.

Beal, C. C. (1967). A Study of the Macroscopic Performance Characteristics of a Stesdy-State Electromagnetic Pump for an Electrolyte. Unpublished master's thesis, Texas A&M University, College Station.

Guna, S. K., Alfred, W. R. & Benjamin, R. (1966). Pulsatile Electromagnetic Pump Without Moving Parts. Medical and Biological Engineering, 24(1), 53-67.

Kerrebrock, J. L. (1986). Optimization of Heat Rejection in Space. Journal of Propulsion, 2, 562-563.

Melcher, J. R. (1981). Continuum Electromechamics. Cambridge: MIT Press.

Samaras, D. G. (1962). Theory of Ion Flow Dynamics. NJ: Prentice-Hall.

Strikwerda, J. C. (1989). Finite Difference Schemes and Partial Differential Equations. NY: Wadsworth & Brooks/Cole Advancs Books & Software.

Swallom, D. W. (1991). Magnetohydrodynamic Submarine Propulsion Systems. Naval Engineering Journal, 103(3), 141-157.

Warrier, G. R., Annamalai, S., Nguyen, T. & Lin, C. H. (1993). Water-Sulfuric Acid as Refrigerant-Absorbent Fluid Pair for the Absorption Heat Pump. ASME Winter Annual Meeting, New Orleans.

Woramontri, W. & Nguyen, T. (1993). A Novel Electrohydrodynamic Pump for the Absorption Heat Pump. ASME Winter Annual Meeting, New Orleans.

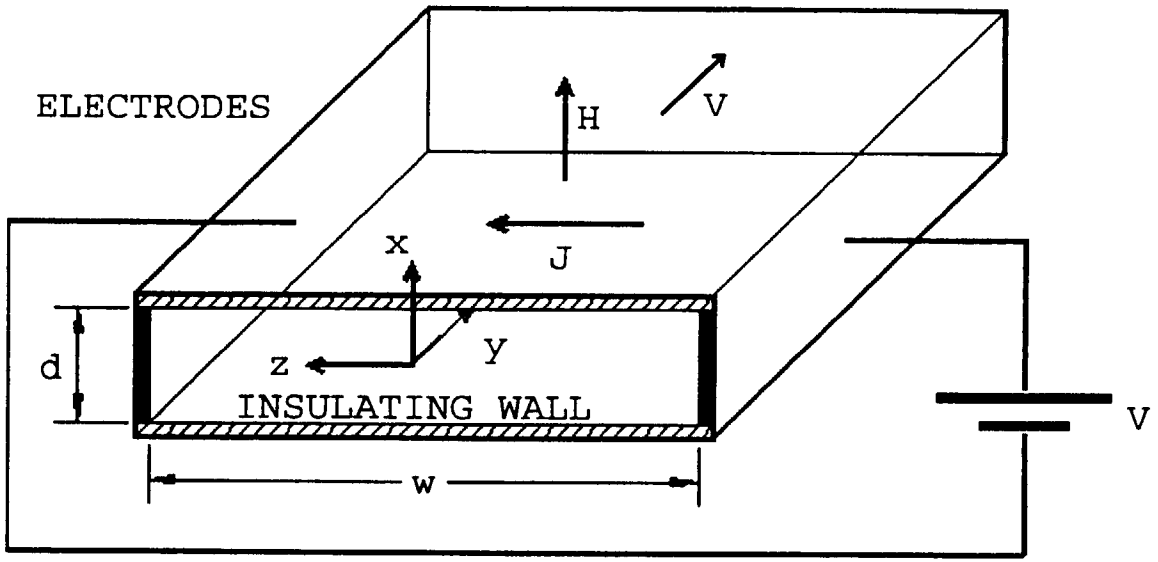

Figure 1

Configuration of an EHD Pump

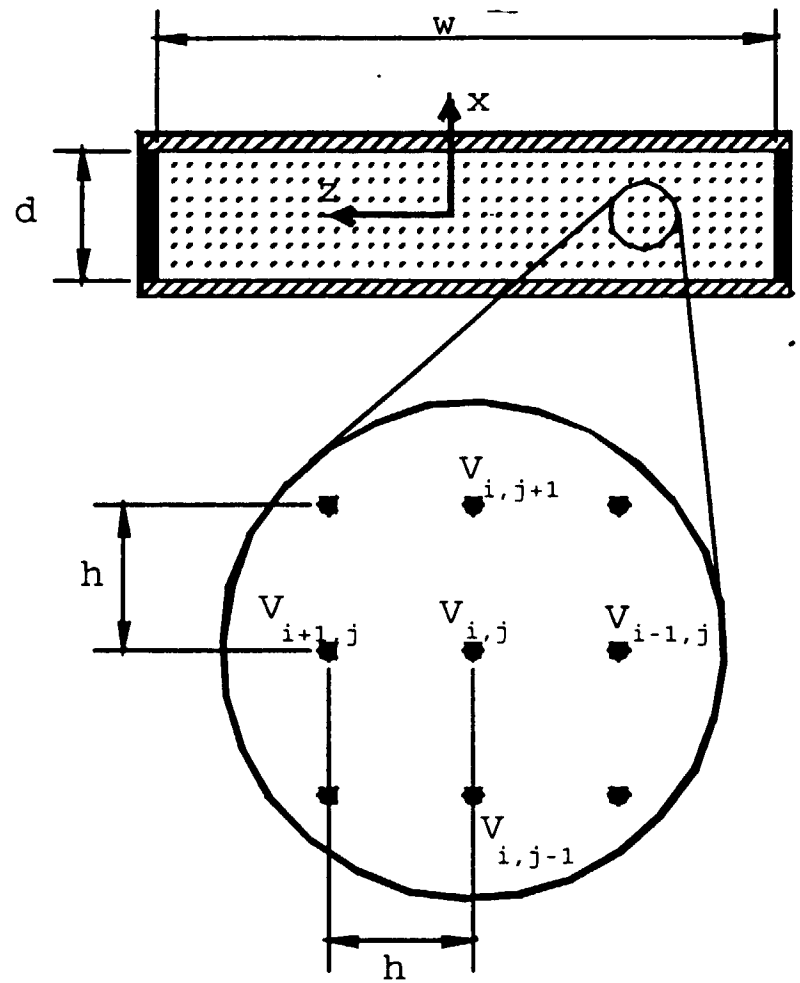

Figure 2

Grid Point Layout used in the Finite Difference Method

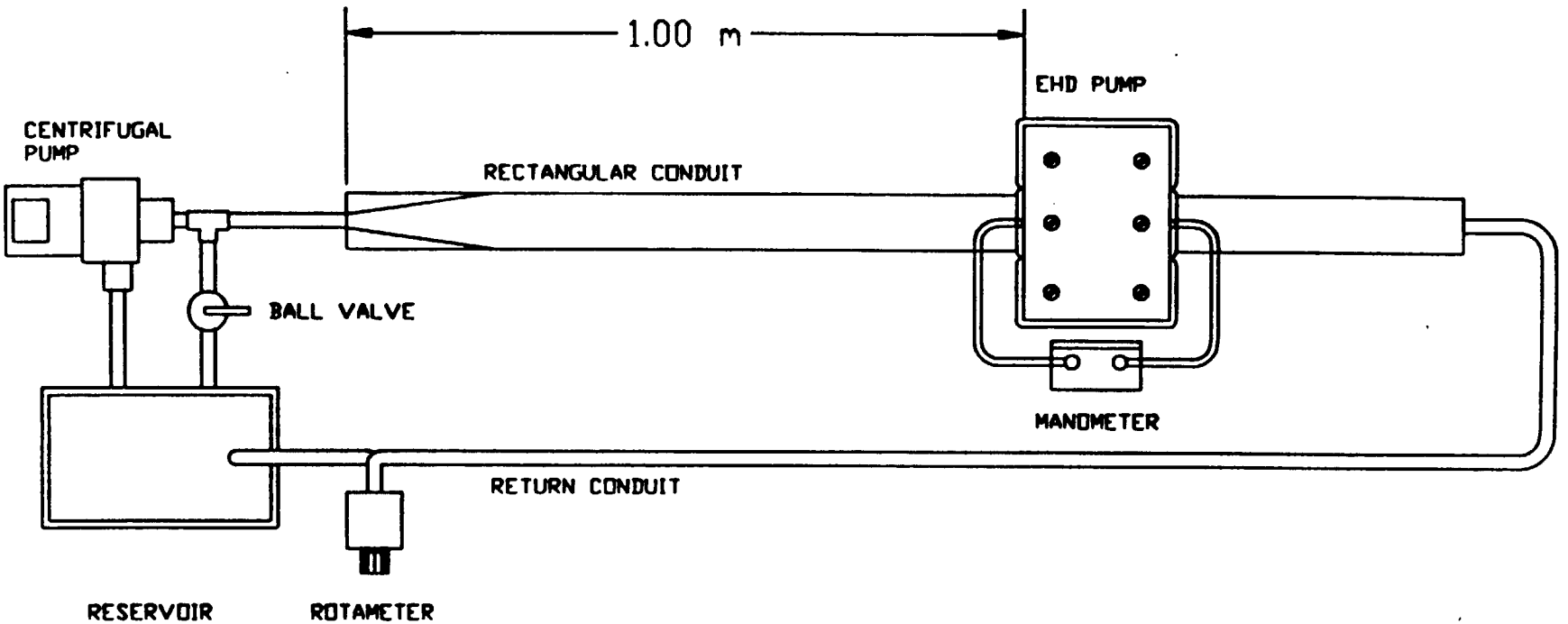

Figure 3

Experimental Apparatus

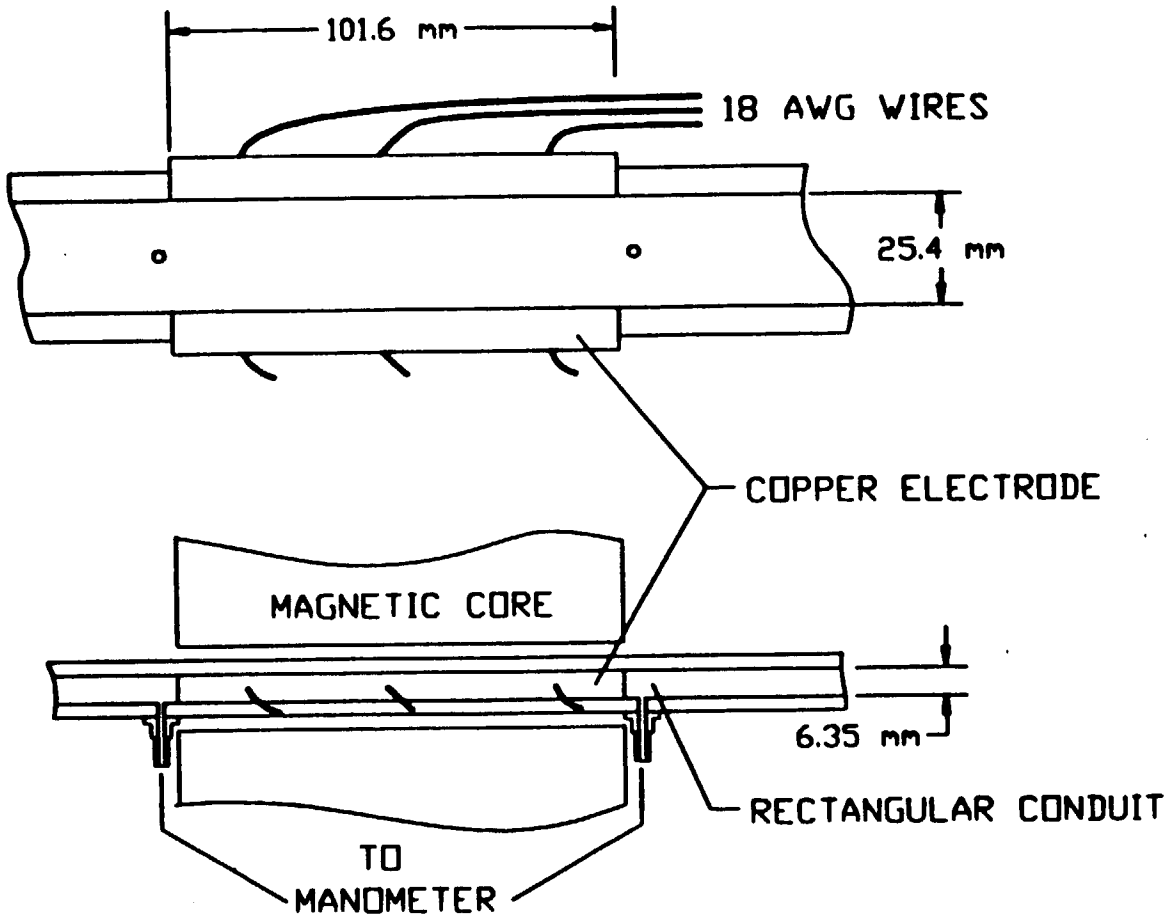

Figure 4

EHD Pump Layout used in the Experiments

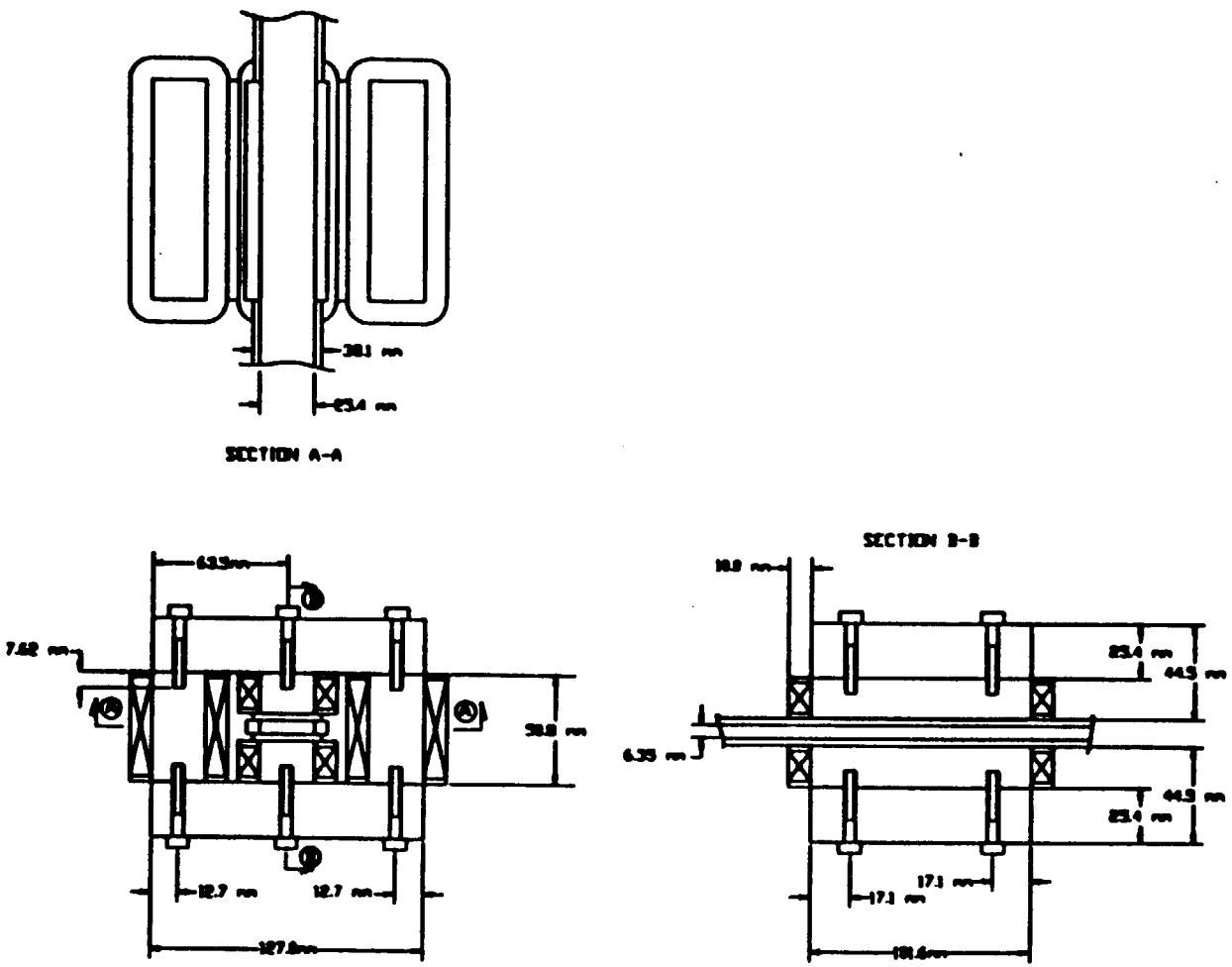

Figure 5

Details of the Electromagnet

Table 1

Experimental Conditions for the Magnetic Flux Density and Voltage Across the Electrodes

	B = 0.1 T	B = 0.2 T	B = 0.3 T	B = 0.4 T
v = 10 V	Experiment #1	Experiment #2	Experiment #3	Experiment #4
v = 15 V	Experiment #5	Experiment #6	Experiment #7	Experiment #8
v = 20 V	Experiment #9	Experiment #10	Experiment #11	Experiment #12

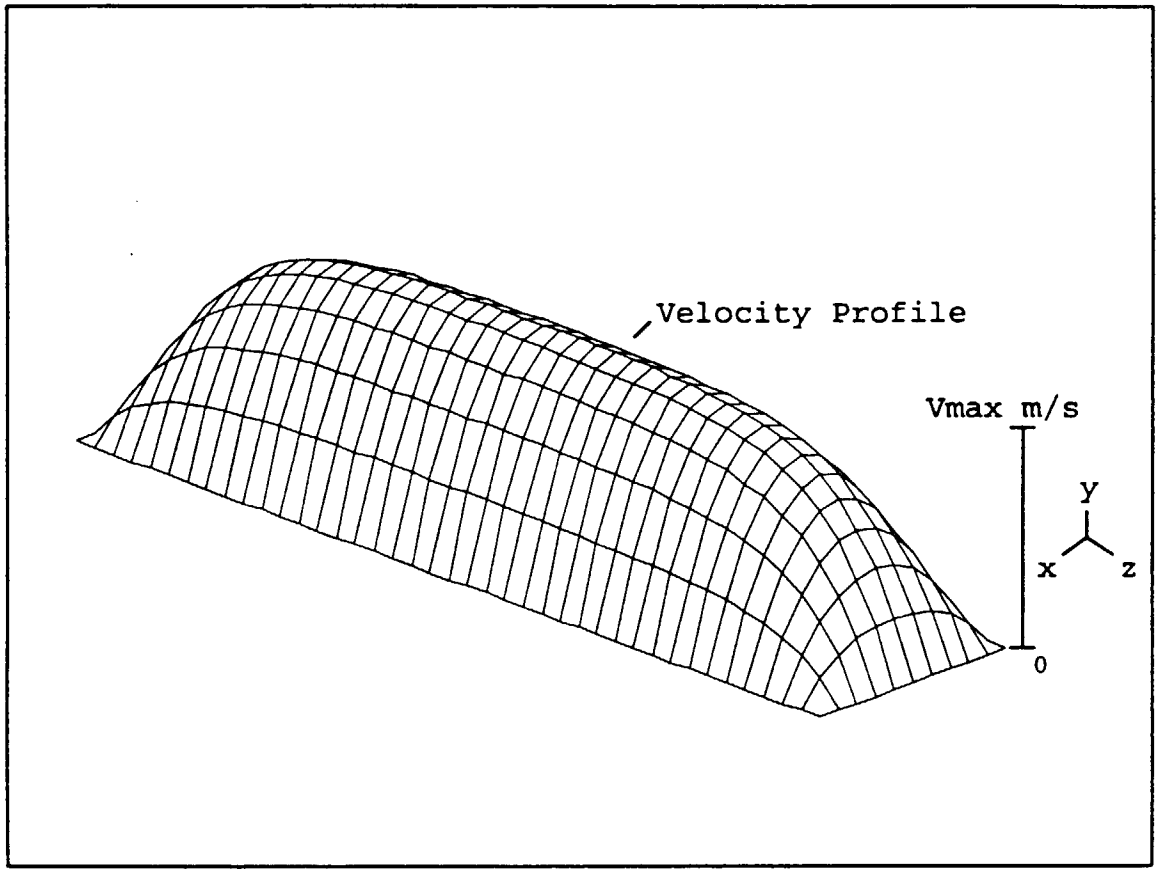

Figure 6

An Example of the Velocity Profile Obtained Numerically

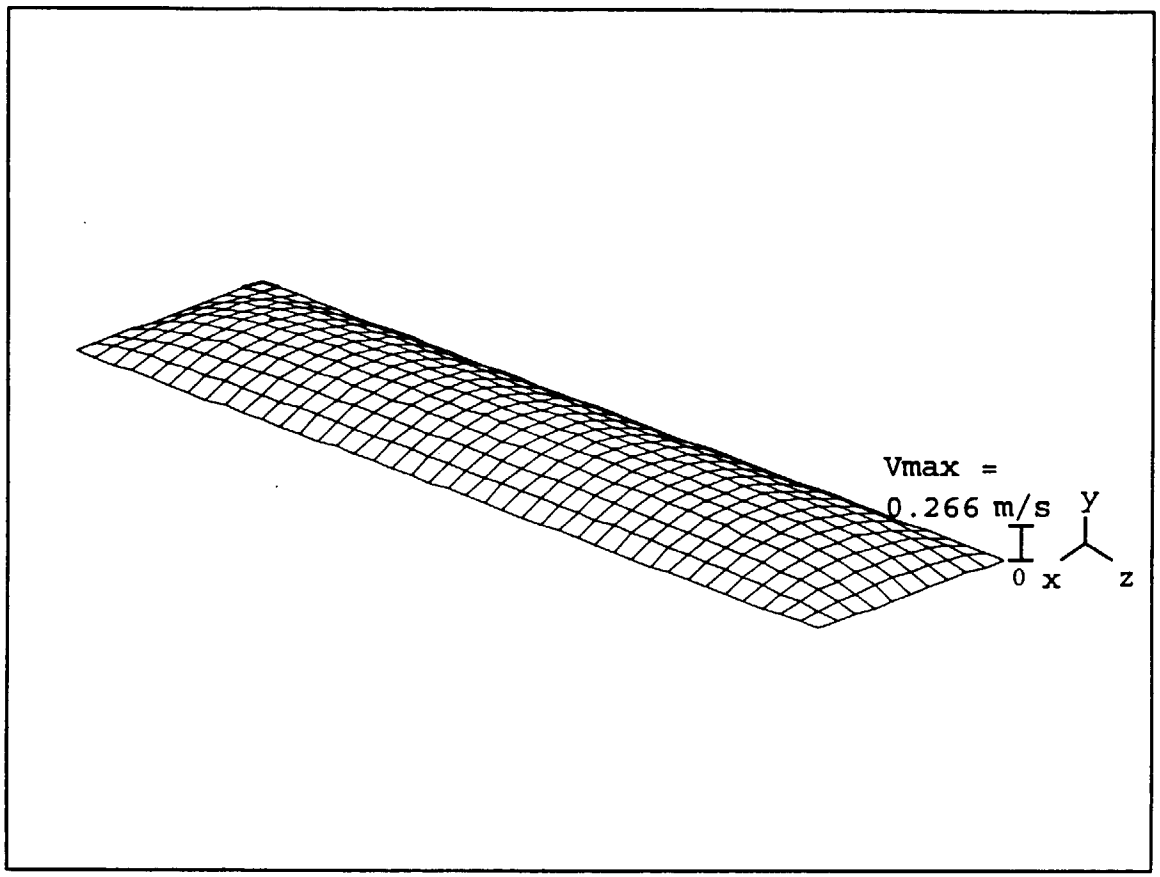

Figure 7

The Velocity Profile for V = 10 V (B = 0.2 T, P = 30 Pa)

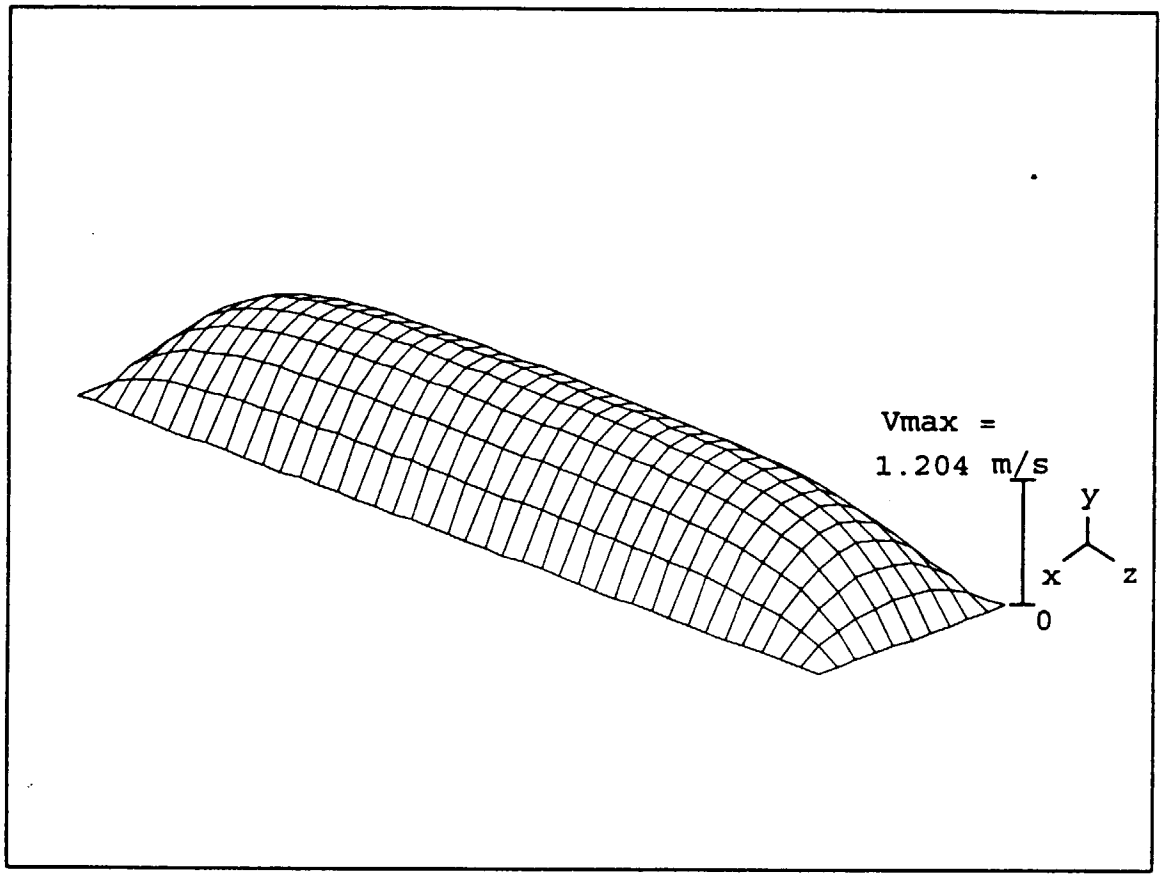

Figure 8

The Velocity Profile for V = 15 V (B = 0.2 T, P = 30 Pa)

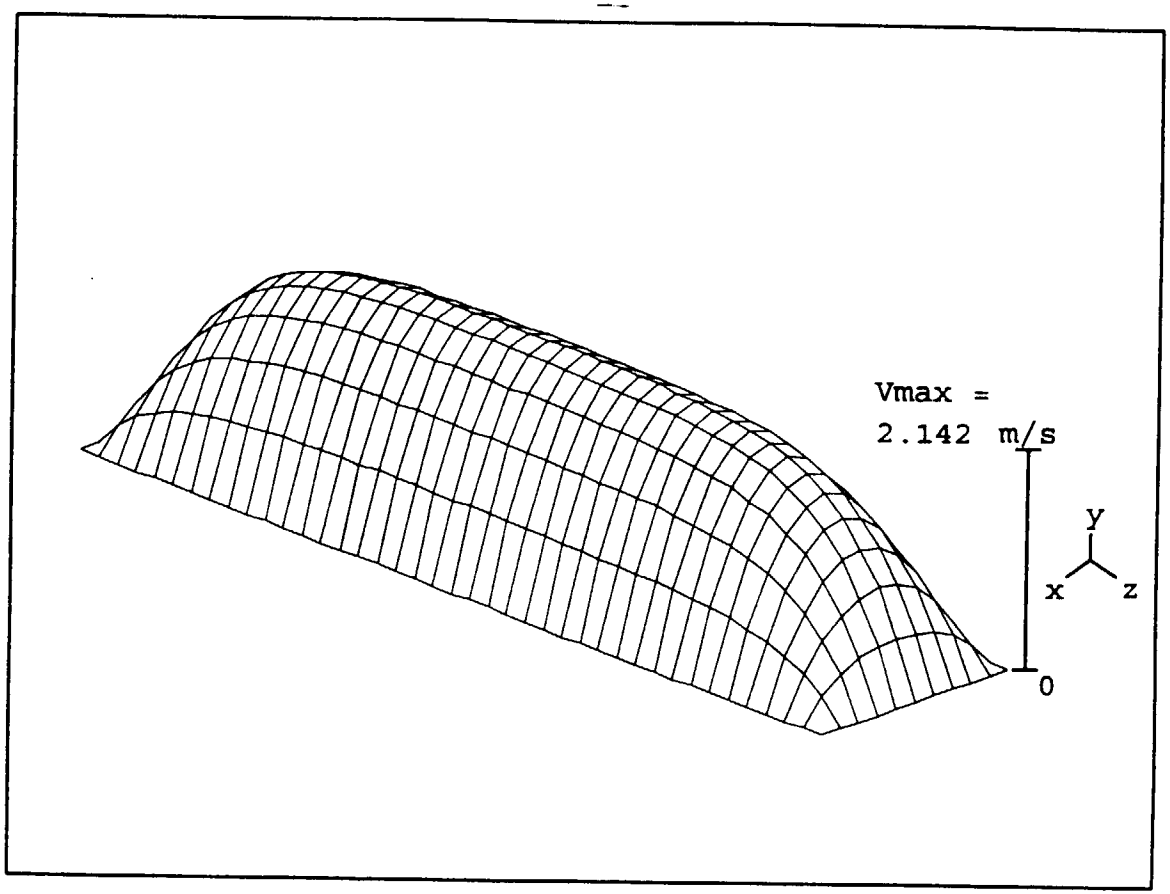

Figure 9

The Velocity Profile for V = 20 V (B = 0.2 T, P = 30 Pa)

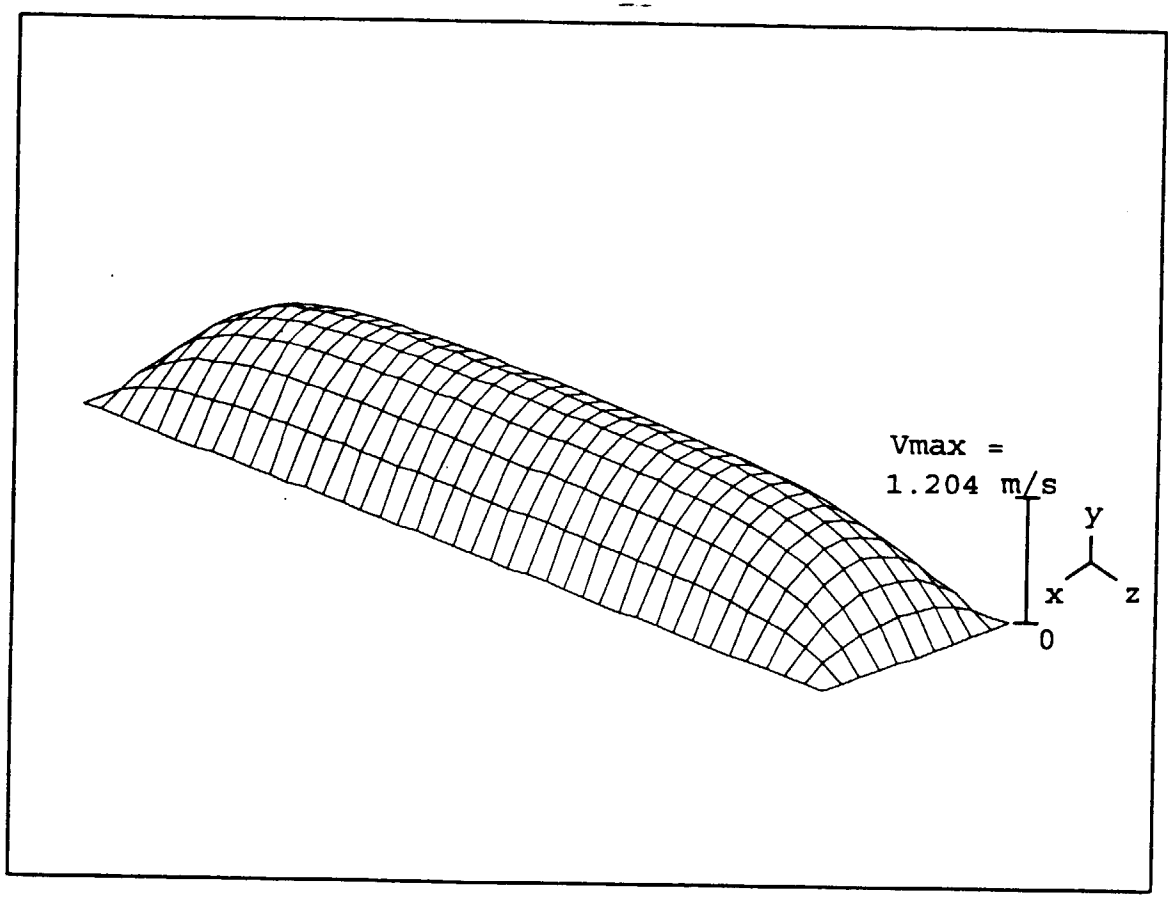

Figure 10

The Velocity Profile for B = 0.2 T (V = 15 V, P = 30 Pa)

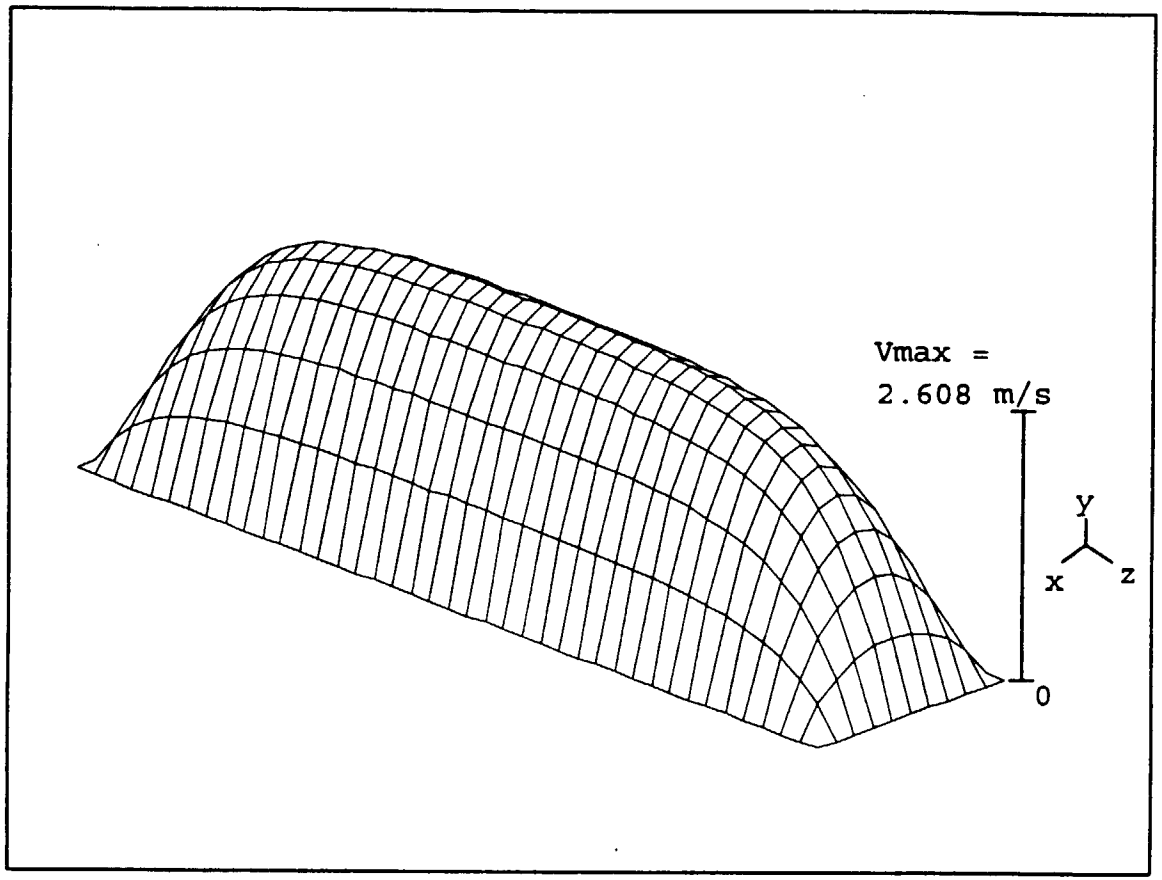

Figure 11

The Velocity Profile for B = 0.3 T (V = 15 V, P = 30 Pa)

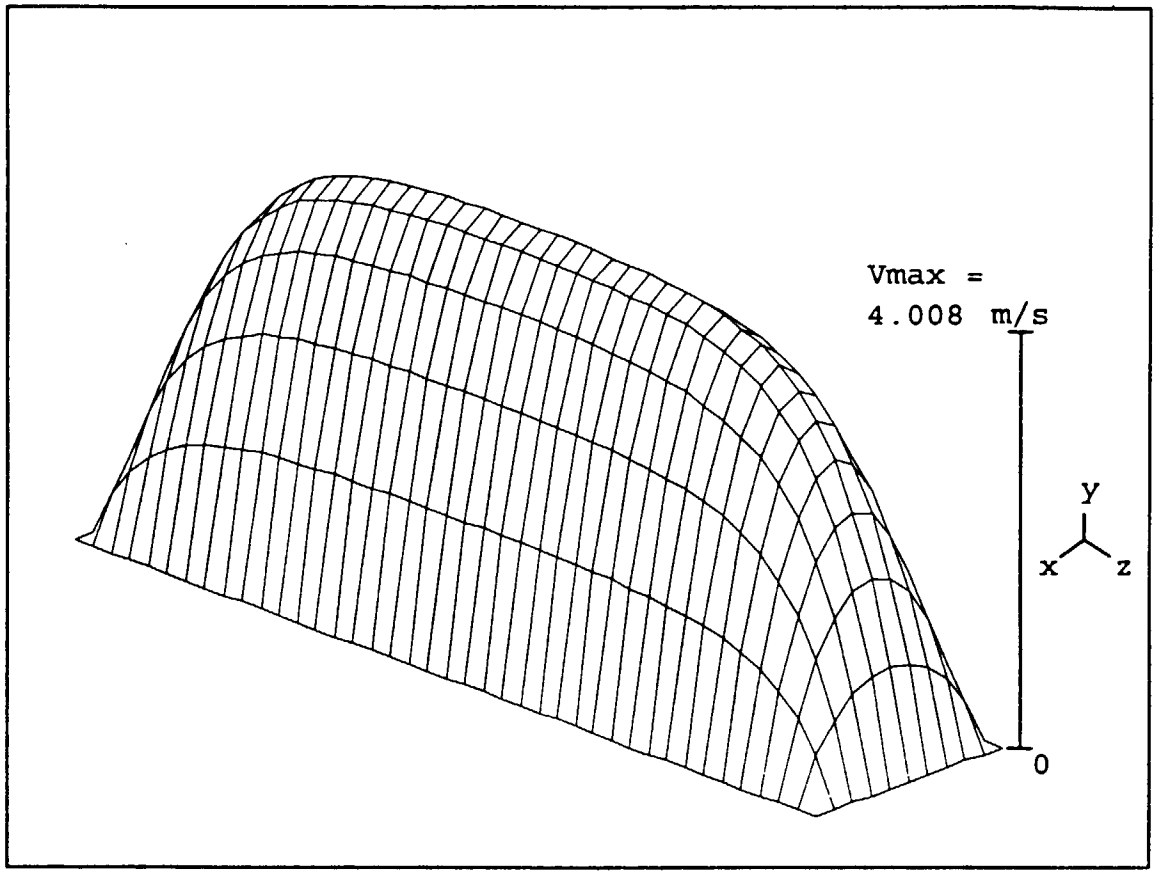

Figure 12

The Velocity Profile for B = 0.4 T (V = 15 V, P = 30 Pa)

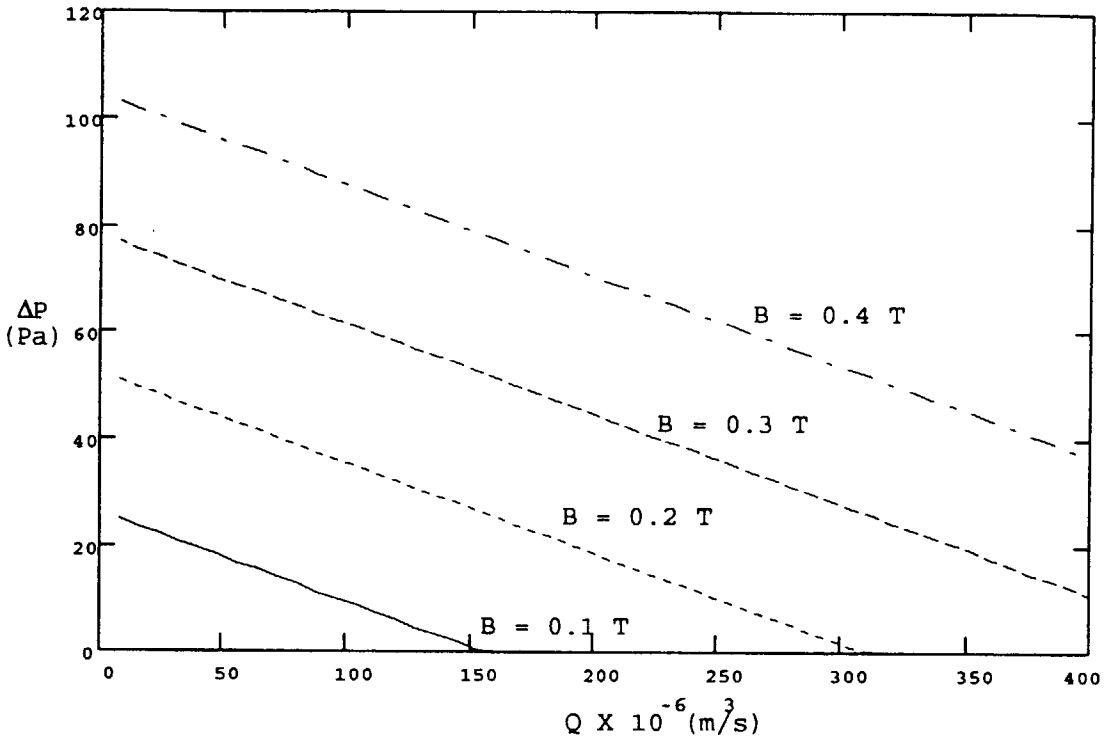

Figure 13

The Pressure - Flow Rate Relationship at Constant Voltage (V = 15 V)

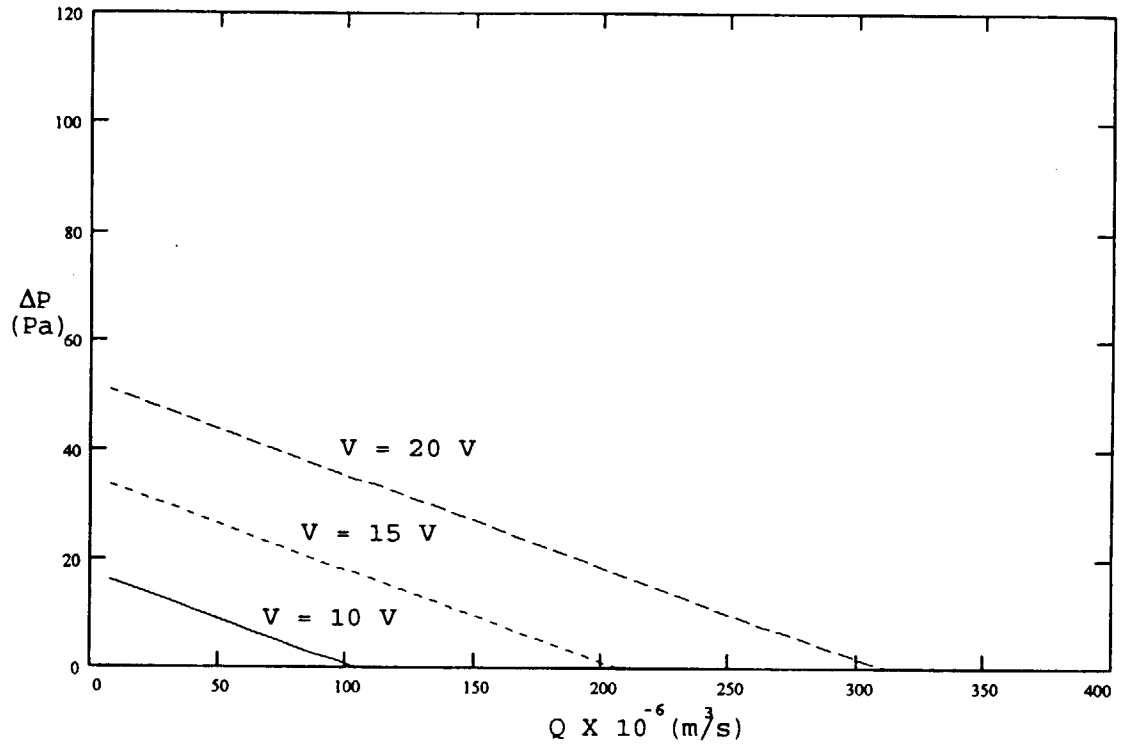

Figure 14

The Pressure - Flow Rate Relationship for Constant Magnetic Flux Density (B = 0.2 T)

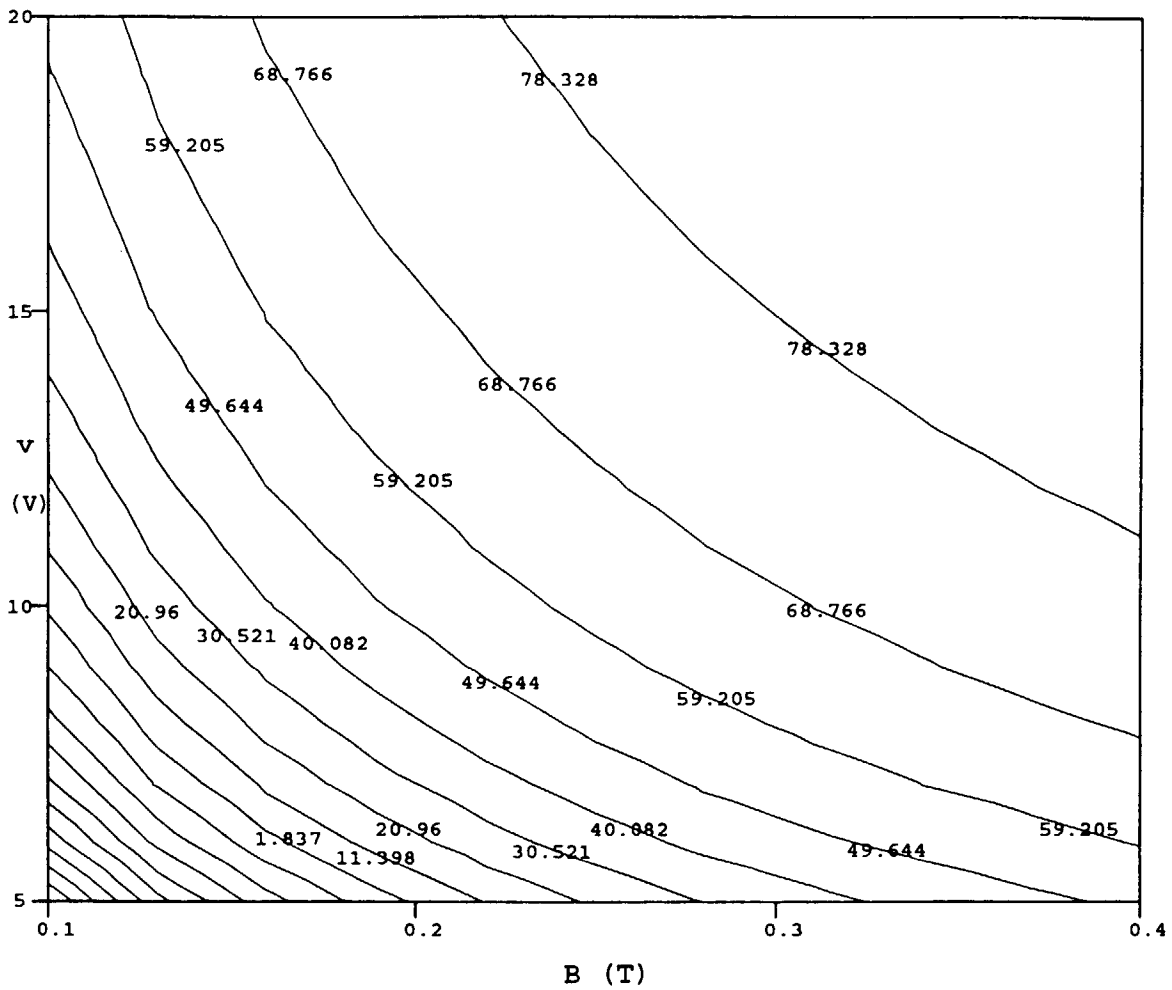

Figure 15

Contour Plot of the Internal Efficiency at Constant Volumetric Flow Rate ($Q = 1 \times 10^{-4}$ m^3/s)

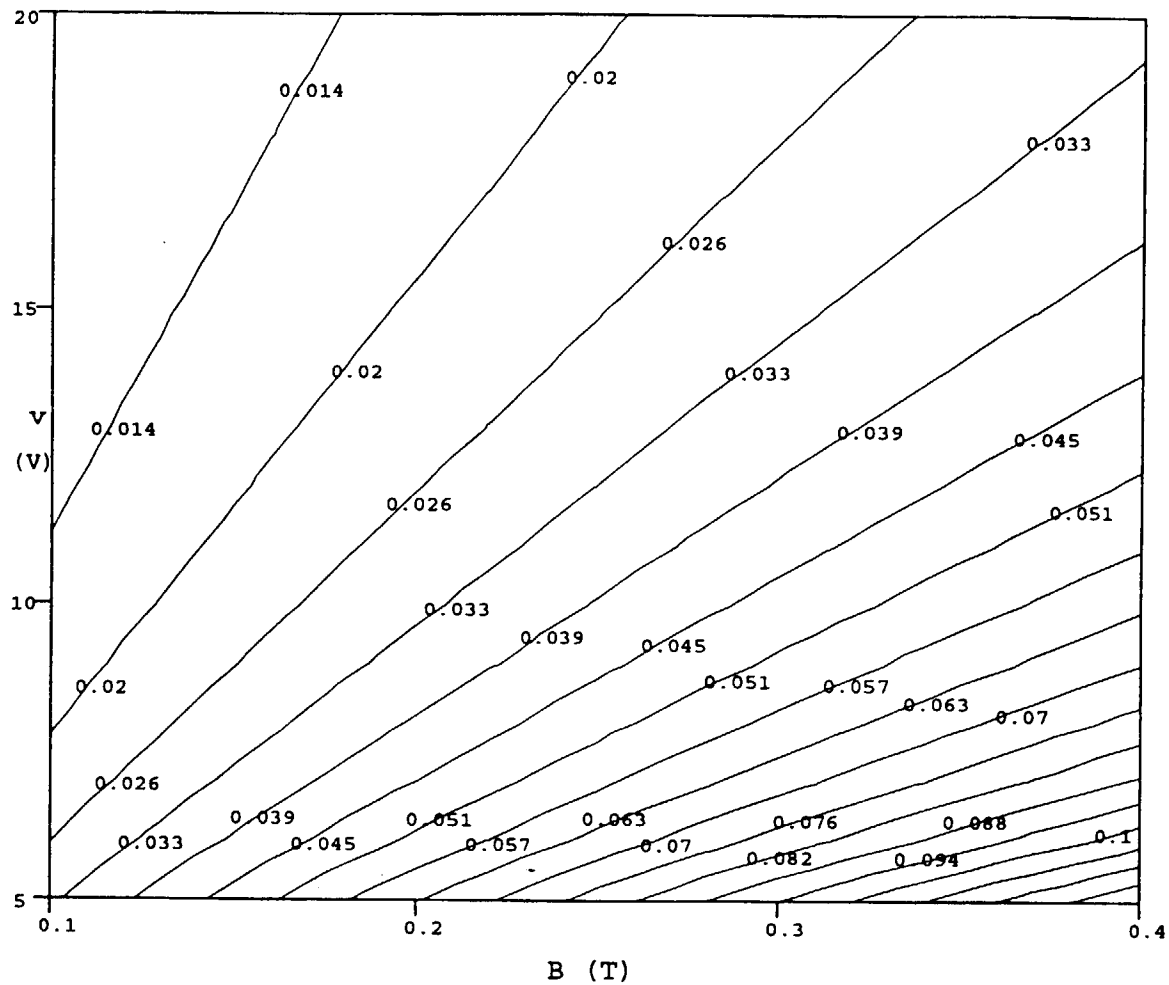

Figure 16

Contour Plot of the Electrical Efficiency at Constant Volumetric Flow Rate ($Q = 1 \times 10^{-4}$ m^3/s)

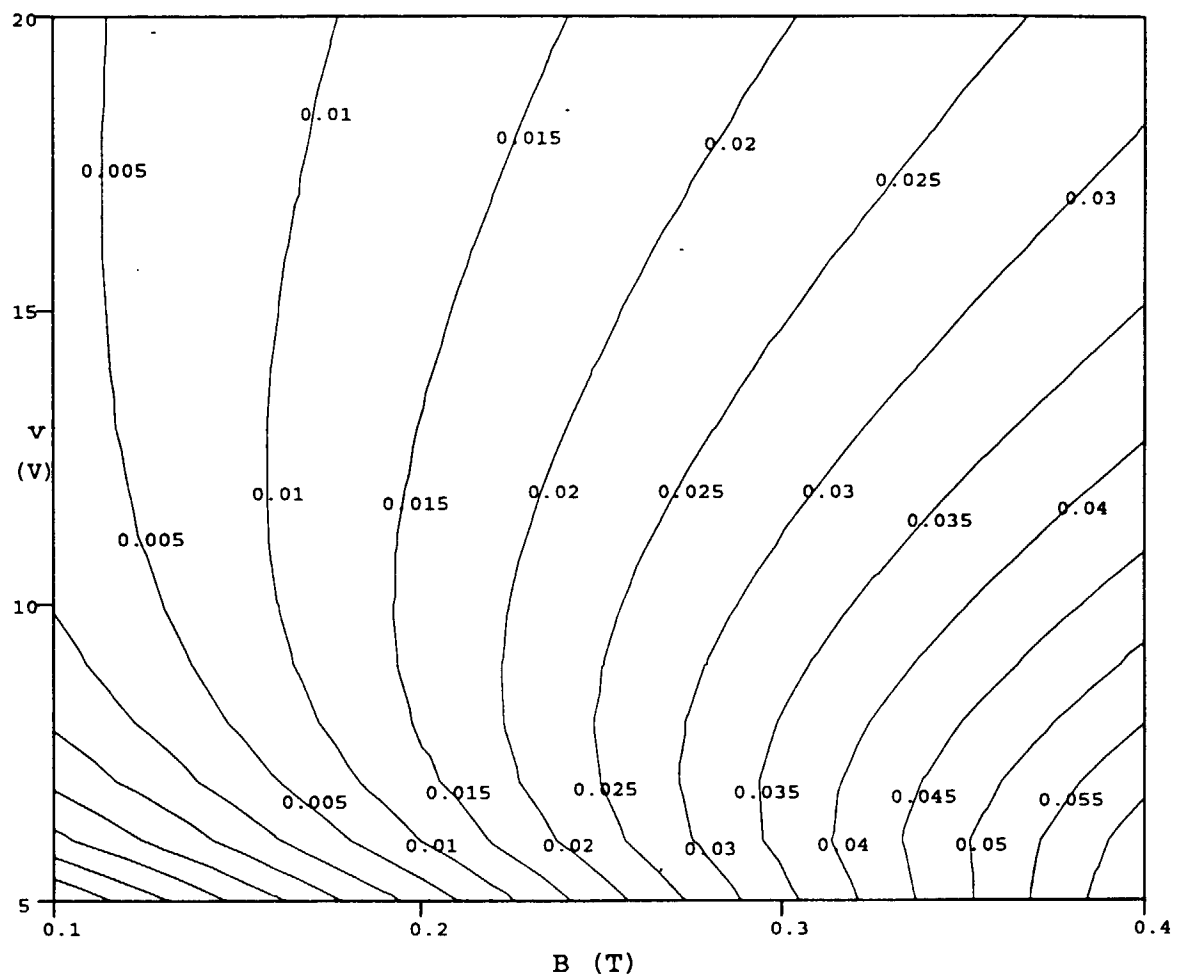

Figure 17

Contour Plot of the Overall Efficiency at Constant Volumetric Flow Rate ($Q = 1 \times 10^{-4}$ m^3/s)

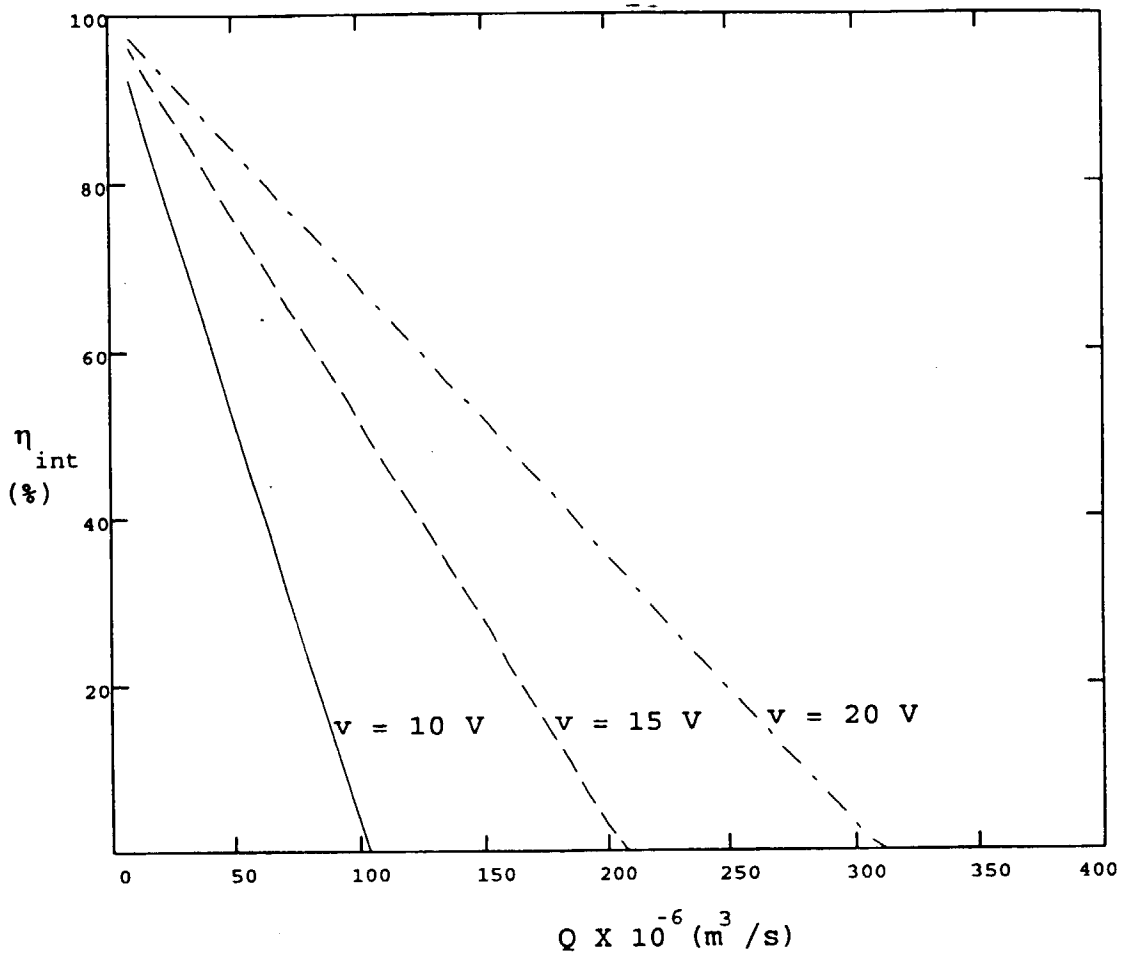

Figure 18

Internal Efficiency as a Function of Applied Voltage at Constant Magnetic Flux Density (B = 0.2 T)

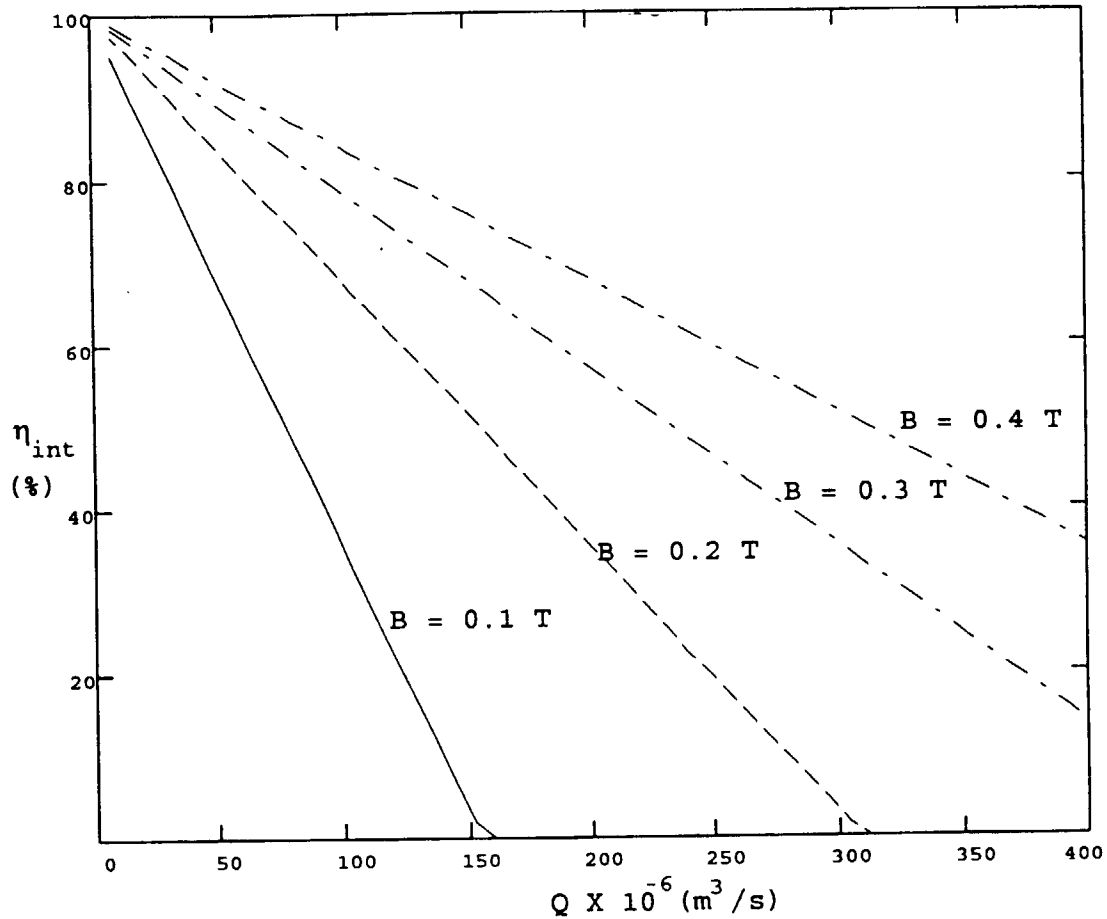

Figure 19

Internal Efficiency as A Function of Magnetic Flux Density at Constant Voltage (V = 15 V)

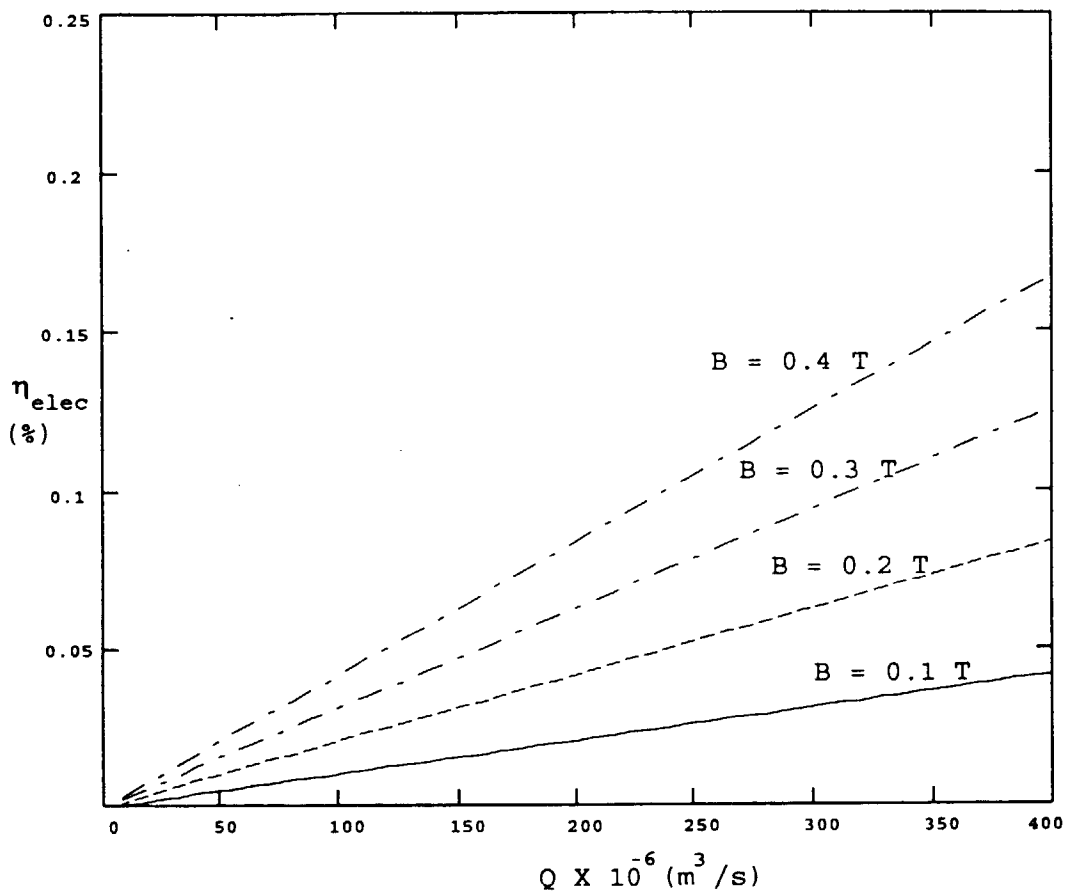

Figure 20

Electrical Efficiency as A Function of Magnetic Flux Density at Constant Voltage (V = 15 V)

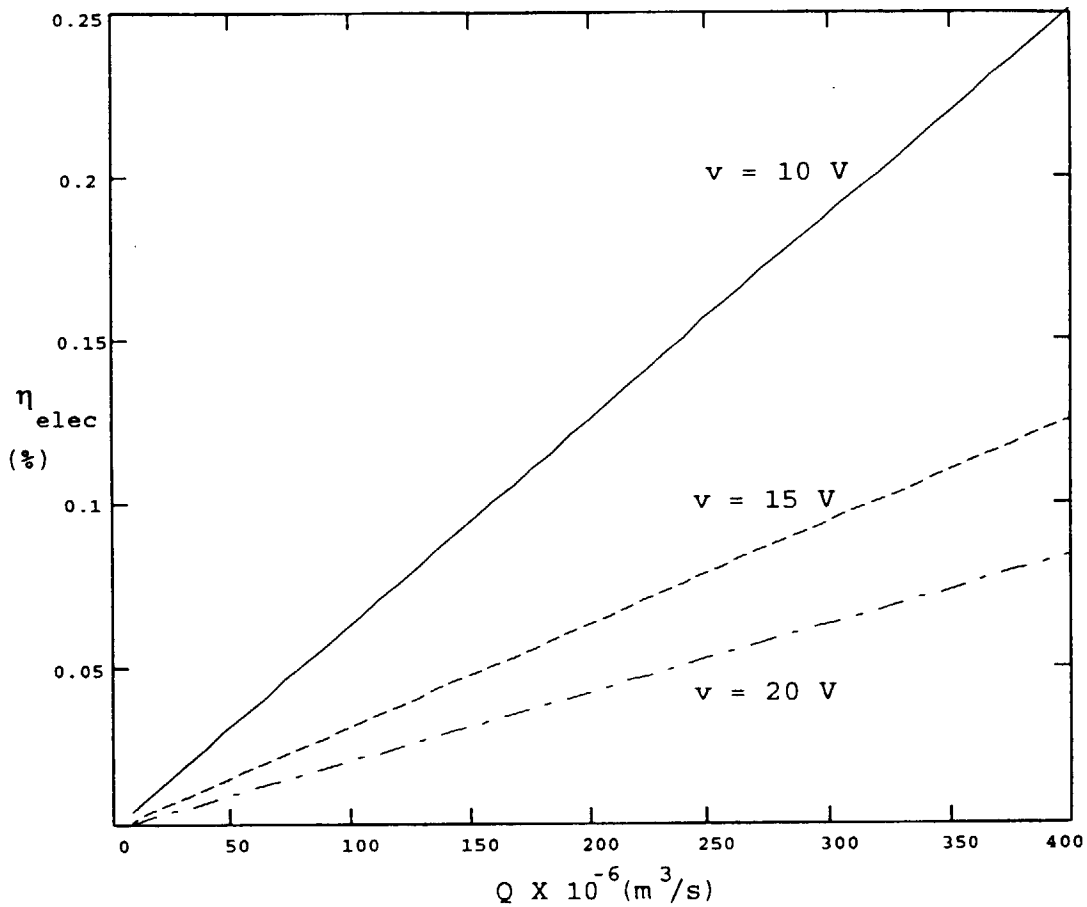

Figure 21

Electrical Efficiency as a Function of Applied Voltage at Constant Magnetic Flux Density (B = 0.2 T)

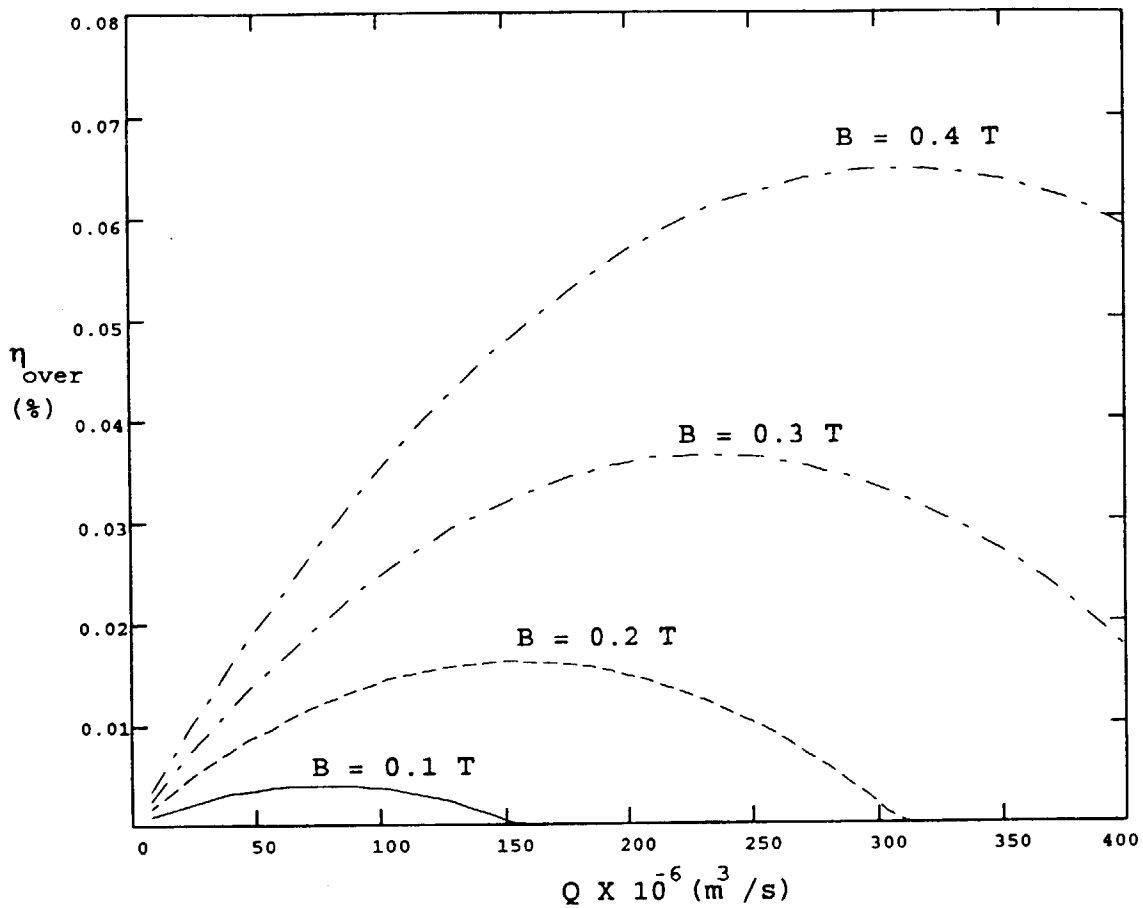

Figure 22

Overall Efficiency as a Function of Magnetic Flux Density at Constant Voltage (V = 15 V)

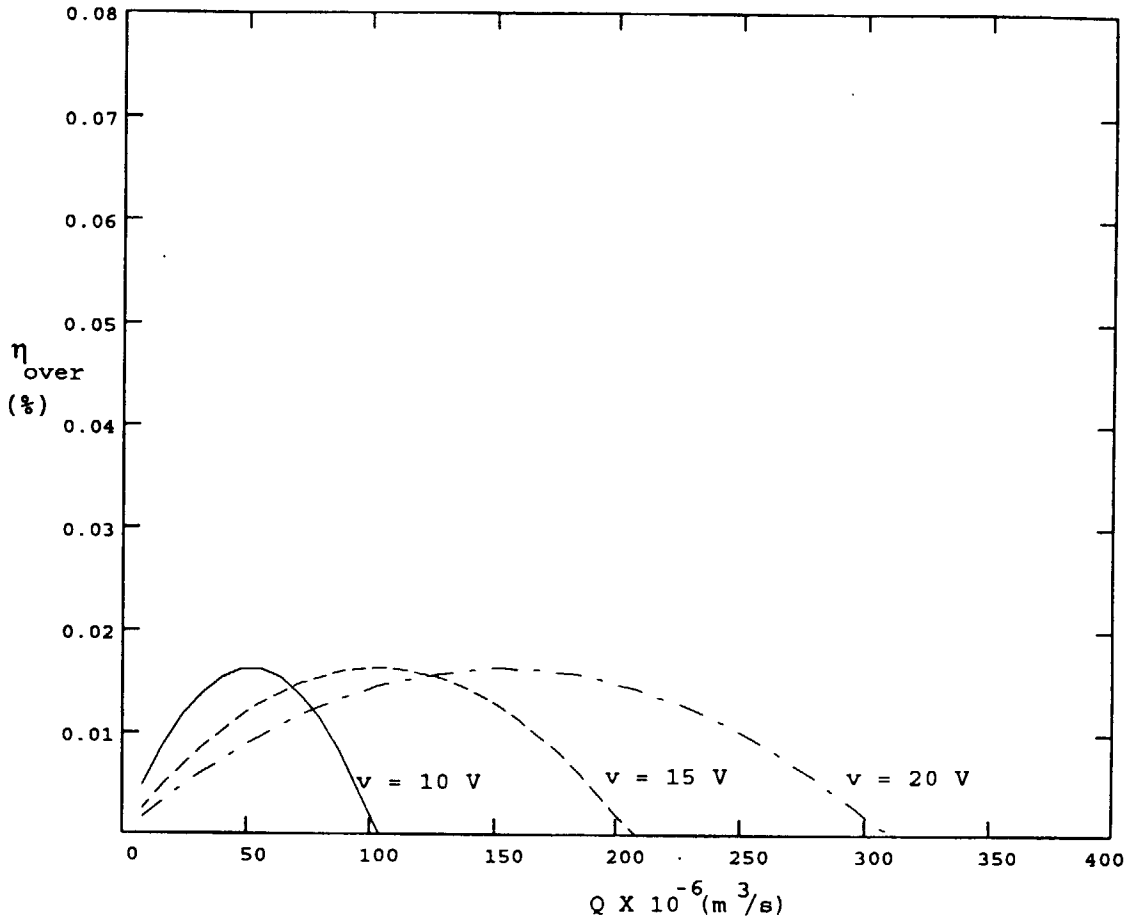

Figure 23

Overall Efficiency as a Function of Applied Voltage at Constant Magnetic Flux Density (B = 0.2 T)

Table 2

Magnetic Flux Density and Voltage Across the Electrodes for Figures 17 to 28

	B = 0.1 T	B = 0.2 T	B = 0.3 T	B = 0.4 T
v = 10 V	Figure 5.12	Figure 5.13	Figure 5.14	Figure 5.15
v = 15 V	Figure 5.16	Figure 5.17	Figure 5.18	Figure 5.19
v = 20 V	Figure 5.20	Figure 5.21	Figure 5.22	Figure 5.23

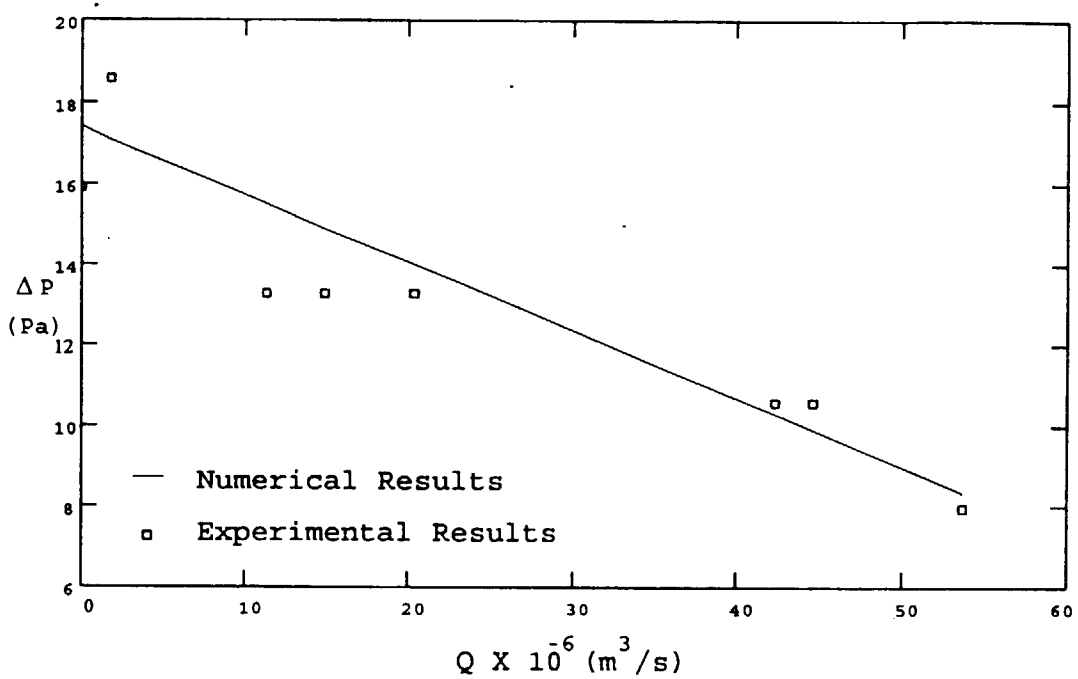

Figure 24

Pressure - Flow Rate Relationship Obtained Numerically and Experimentally for V = 10 V and B = 0.1 T

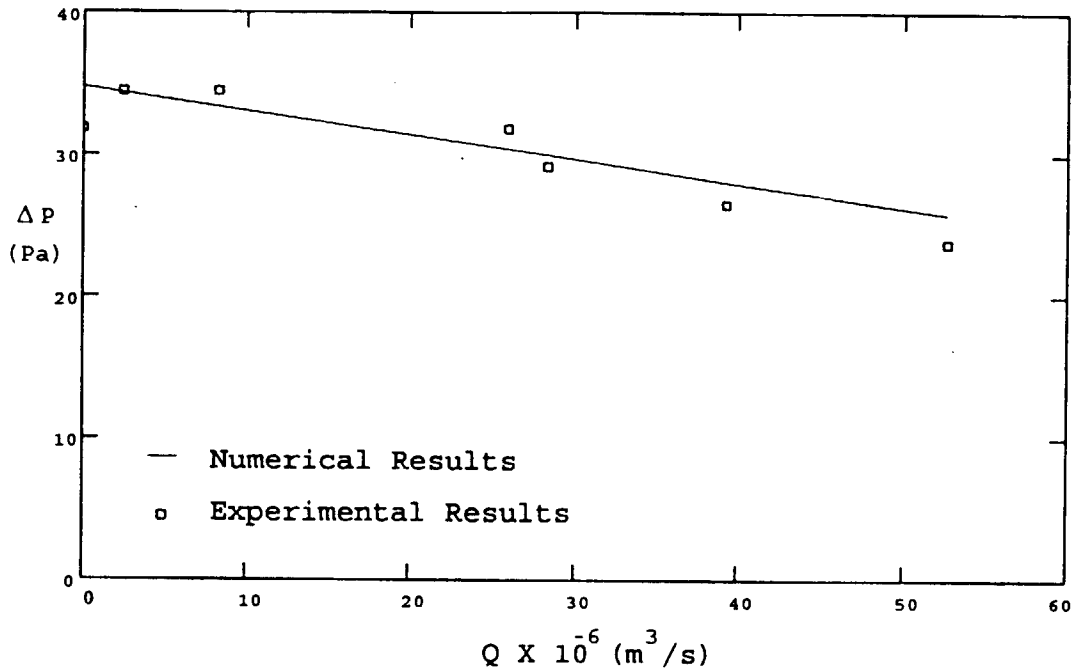

Figure 25

Pressure - Flow Rate Relationship Obtained Numerically and Experimentally for V = 10 V and B = 0.2 T

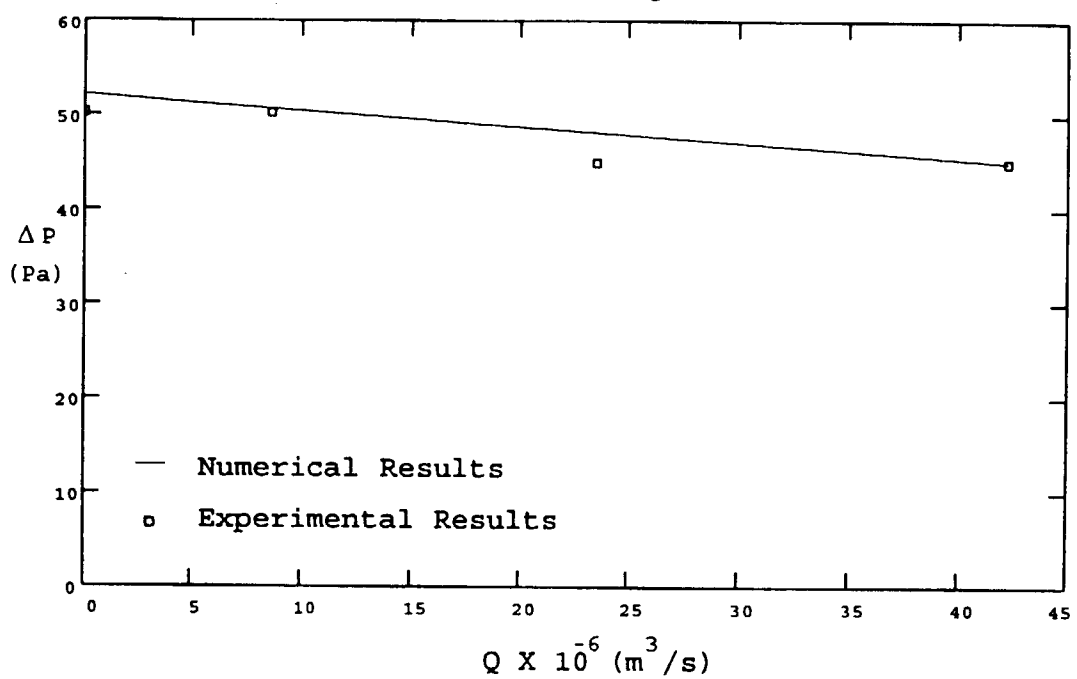

Figure 26

Pressure - Flow Rate Relationship Obtained Numerically and Experimentally for V = 10 V and B = 0.3 T

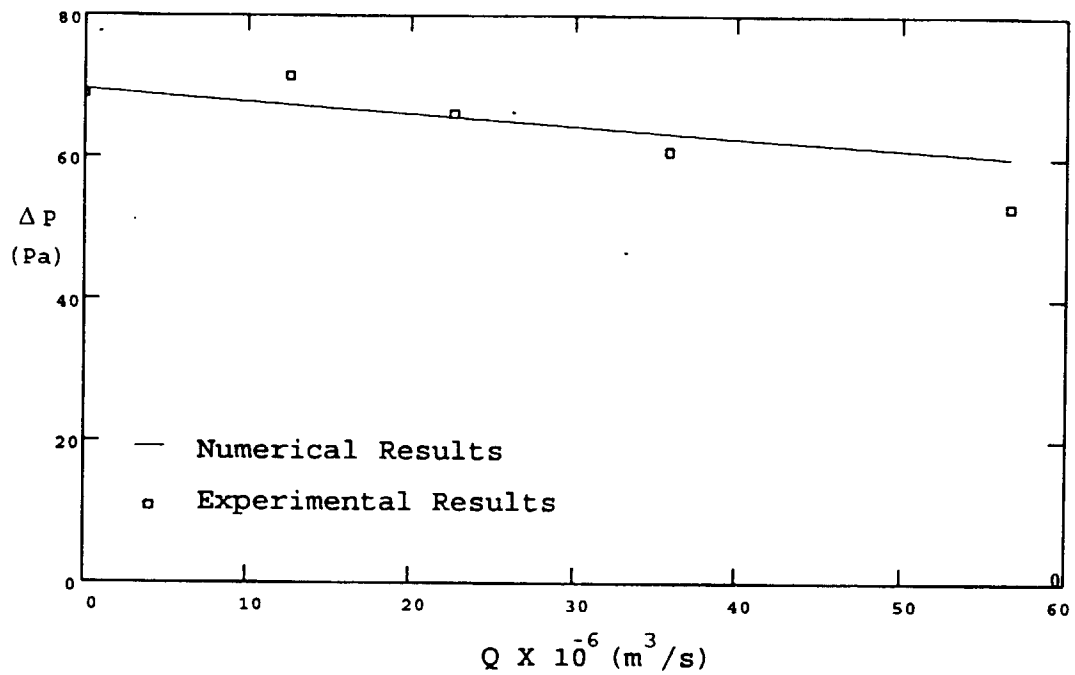

Figure 27

Pressure - Flow Rate Relationship Obtained Numerically and Experimentally for V = 10 V and B = 0.4 T

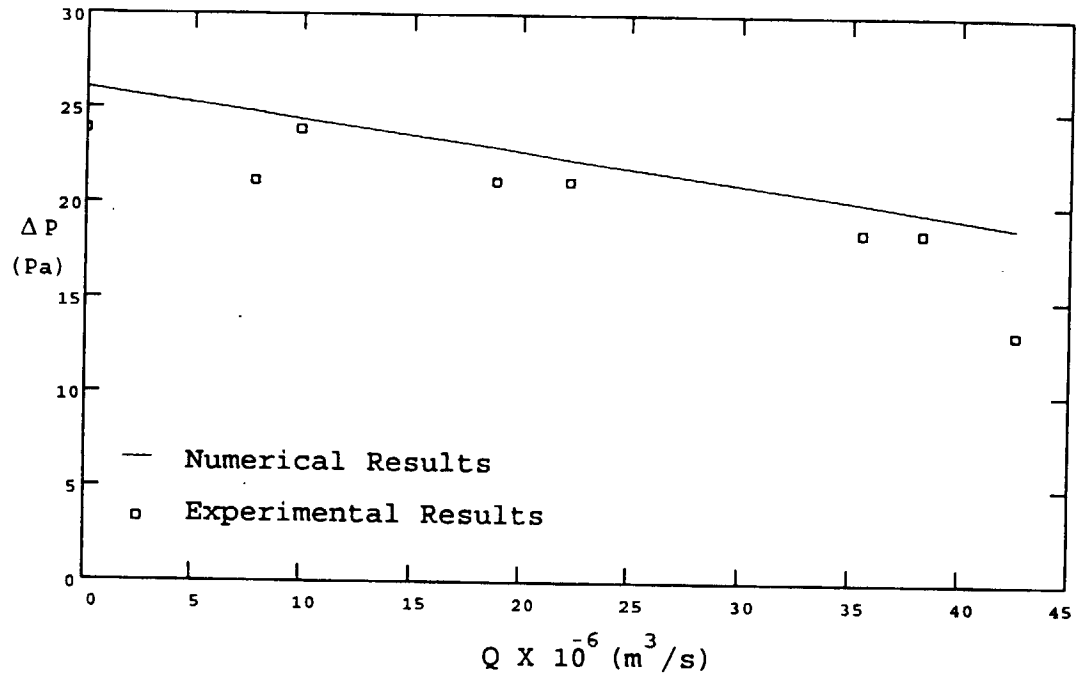

Figure 28

Pressure - Flow Rate Relationship Obtained Numerically and Experimentally for V = 15 V and B = 0.1 T

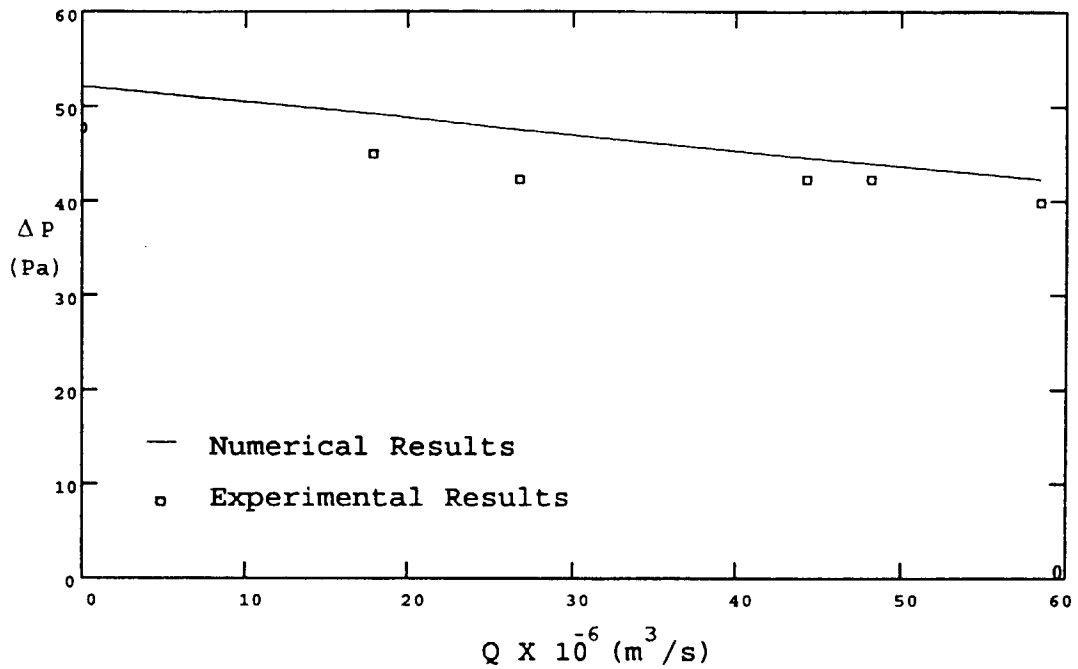

Figure 29

Pressure - Flow Rate Relationship Obtained Numerically and Experimentally for V = 15 V and B = 0.2 T

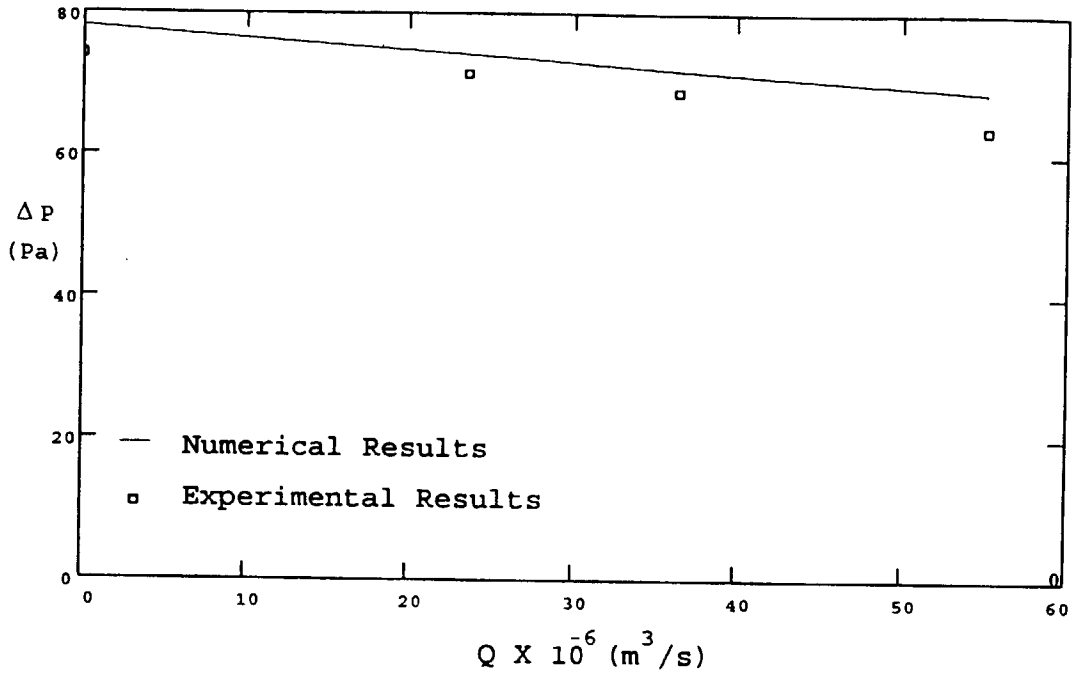

Figure 30

Pressure - Flow Rate Relationship Obtained Numerically and Experimentally for V = 15 V and B = 0.3 T

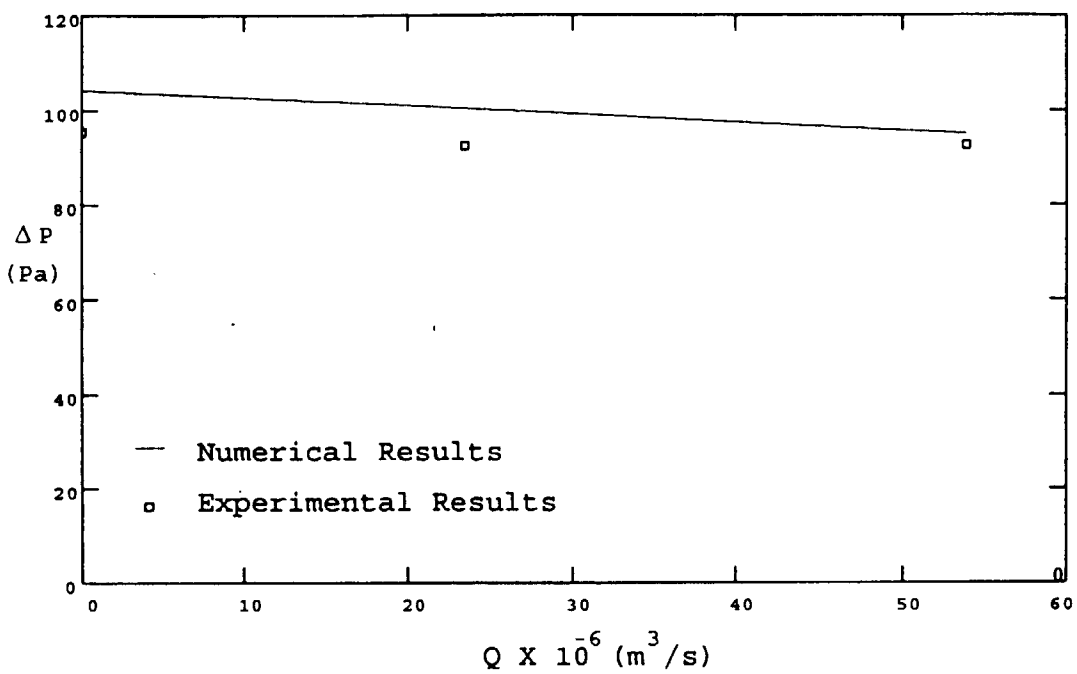

Figure 31

Pressure - Flow Rate Relationship Obtained Numerically and Experimentally for V = 15 V and B = 0.4 T

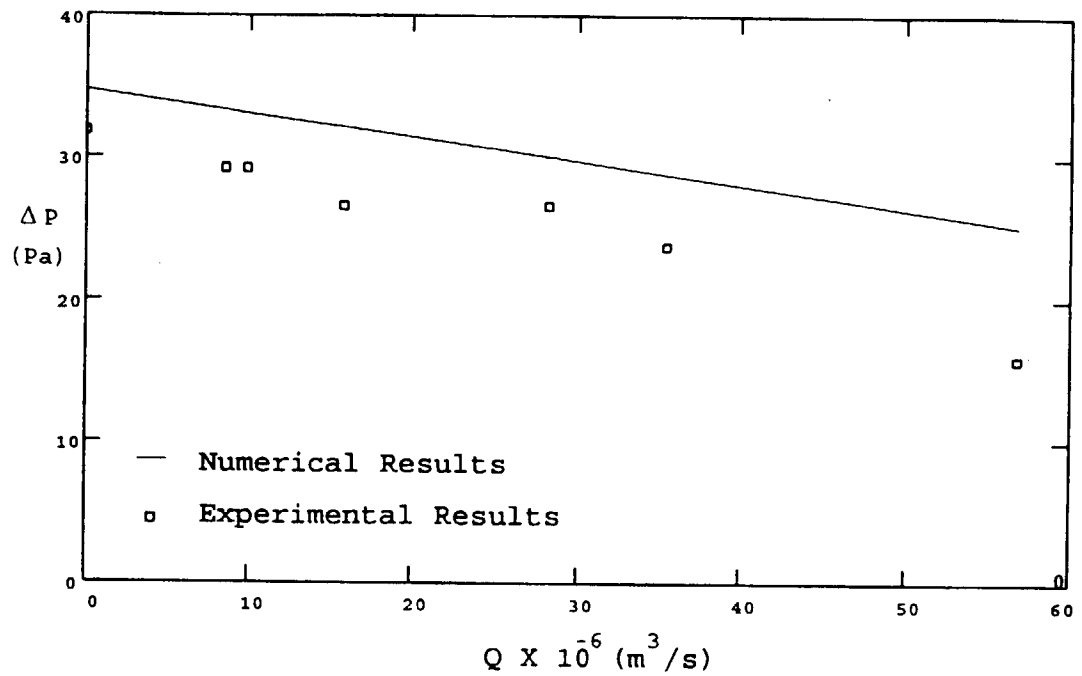

Figure 32

Pressure - Flow Rate Relationship Obtained Numerically and Experimentally for V = 20 V and B = 0.1 T

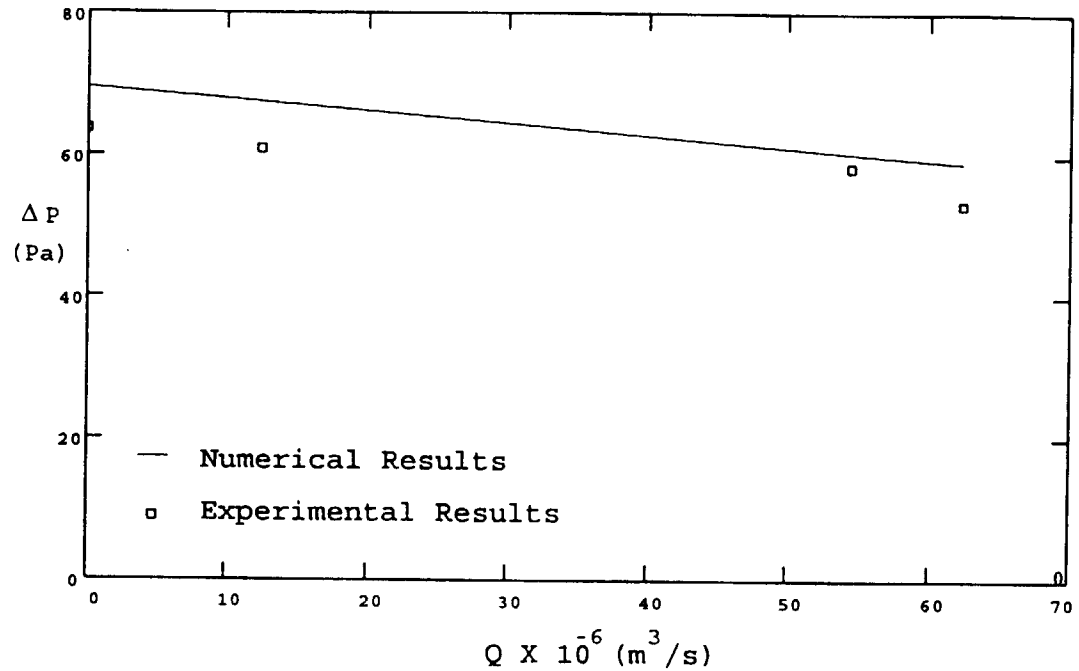

Figure 33

Pressure - Flow Rate Relationship Obtained Numerically and Experimentally for V = 20 V and B = 0.2 T

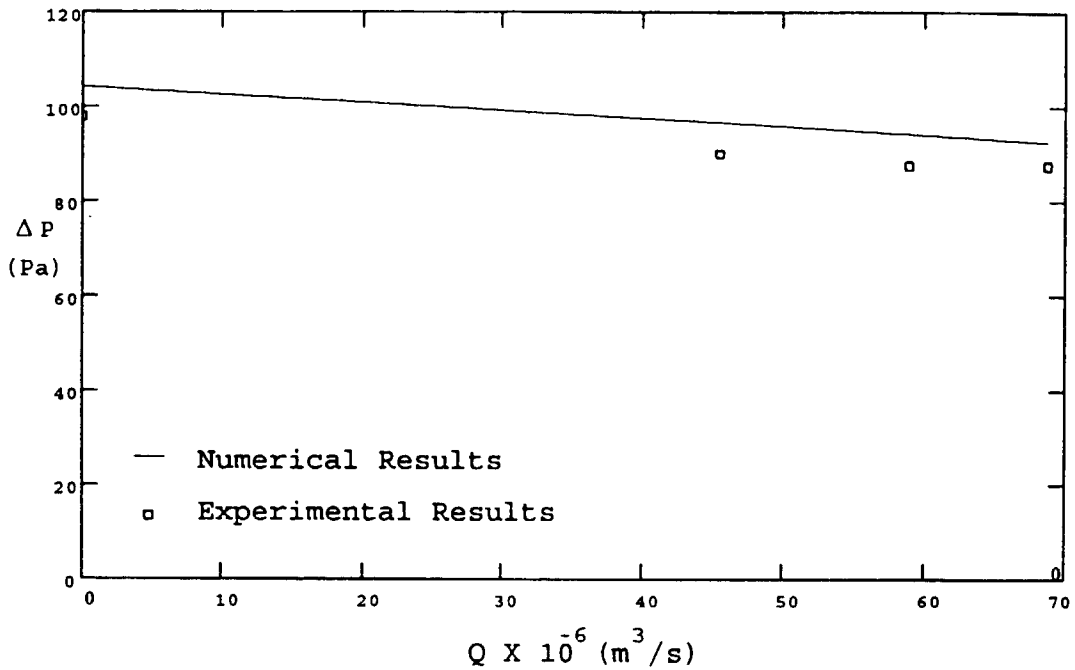

Figure 34

Pressure - Flow Rate Relationship Obtained Numerically and Experimentally for V = 20 V and B = 0.3 T

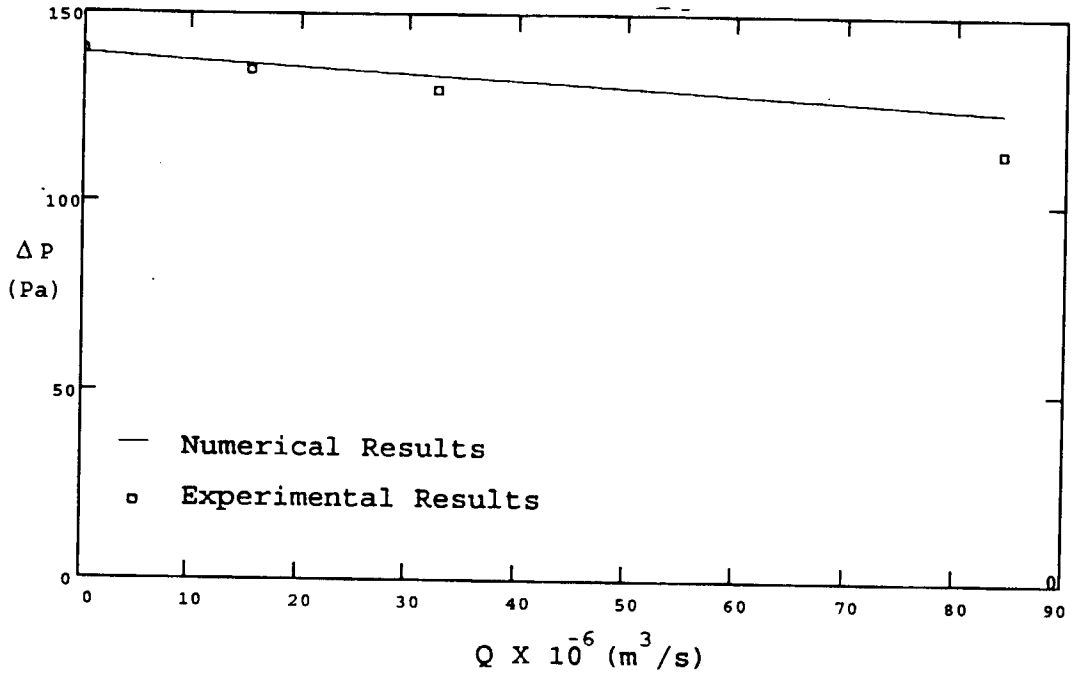

Figure 35

Pressure - Flow Rate Relationship Obtained Numerically and Experimentally for V = 20 V and B = 0.4 T

Table 3

Magnetic Flux Density and Voltage Across the Electrodes for Figures 29 to 40

	B = 0.1 T	B = 0.2 T	B = 0.3 T	B = 0.4 T
v = 10 V	Figure 5.24	Figure 5.25	Figure 5.26	Figure 5.27
v = 15 V	Figure 5.28	Figure 5.29	Figure 5.30	Figure 5.31
v = 20 V	Figure 5.30	Figure 5.31	Figure 5.34	Figure 5.35

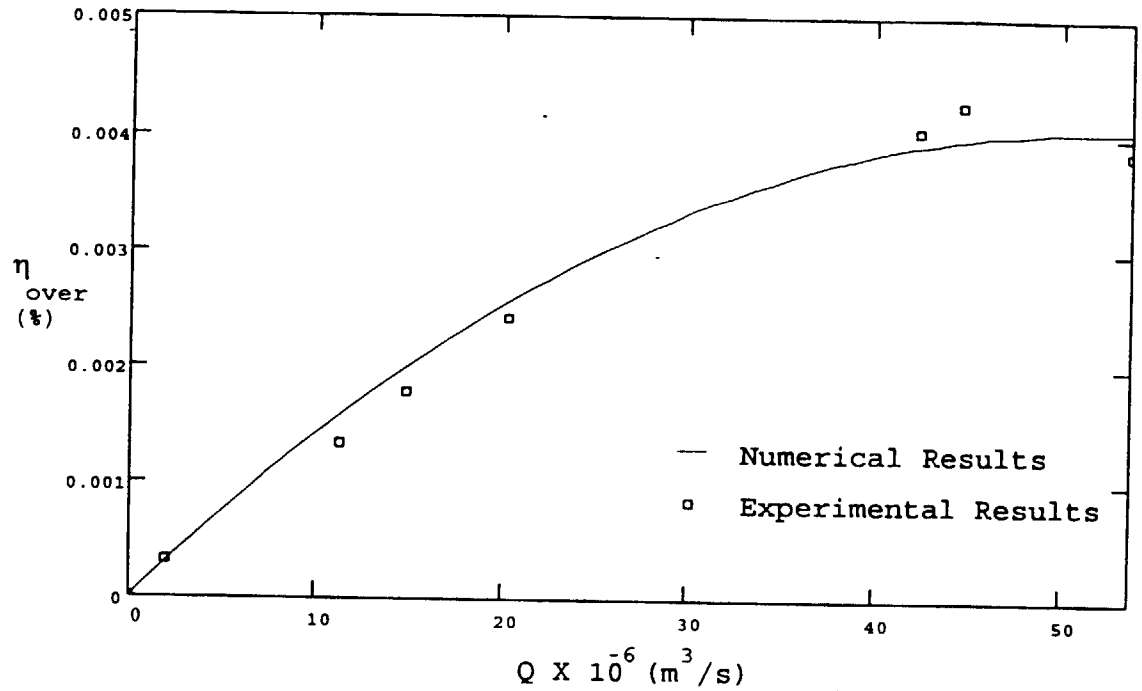

Figure 36

Overall Efficiency Obtained Numerically and Experimentally for V = 10 V and B = 0.1 T

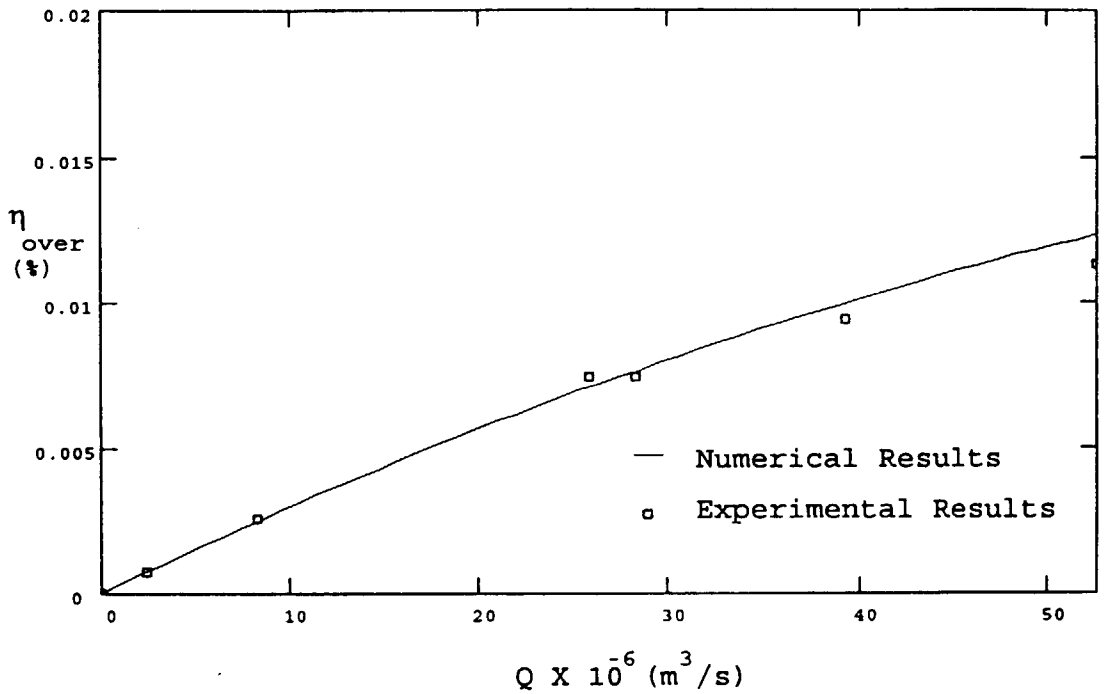

Figure 37

Overall Efficiency Obtained Numerically and Experimentally for V = 10 V and B = 0.2 T

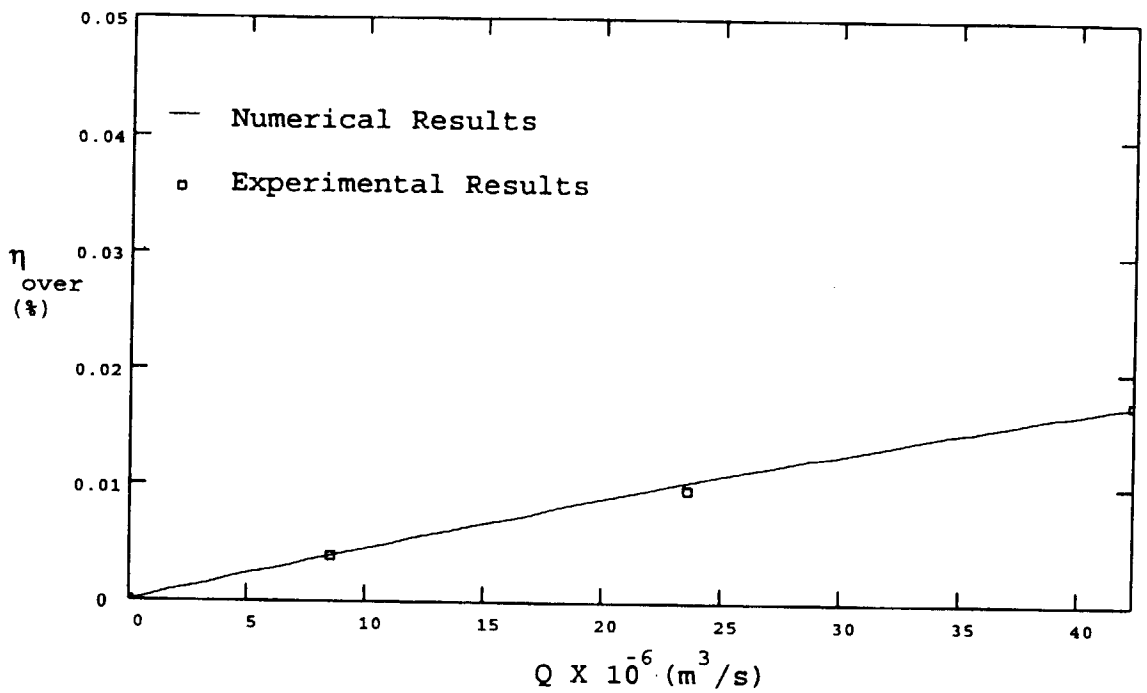

Figure 38

Overall Efficiency Obtained Numerically and Experimentally for V = 10 V and B = 0.3 T

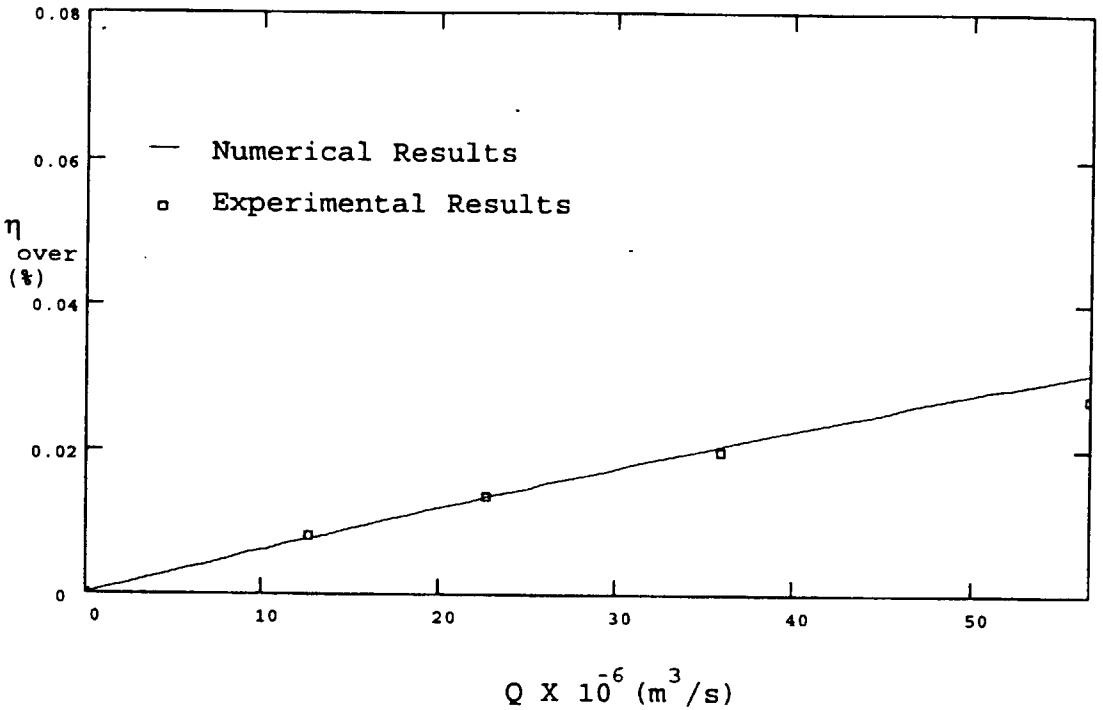

Figure 39

Overall Efficiency Obtained Numerically and Experimentally for V = 10 V and B = 0.4 T

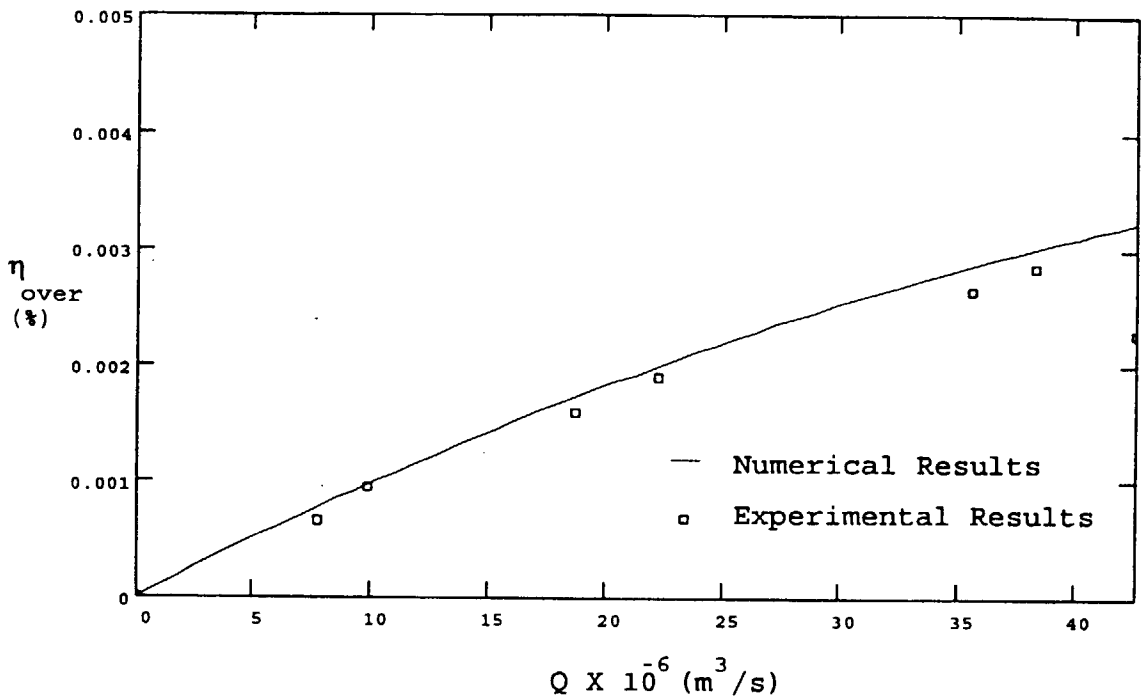

Figure 40

Overall Efficiency Obtained Numerically and Experimentally for V = 15 V and B = 0.1 T

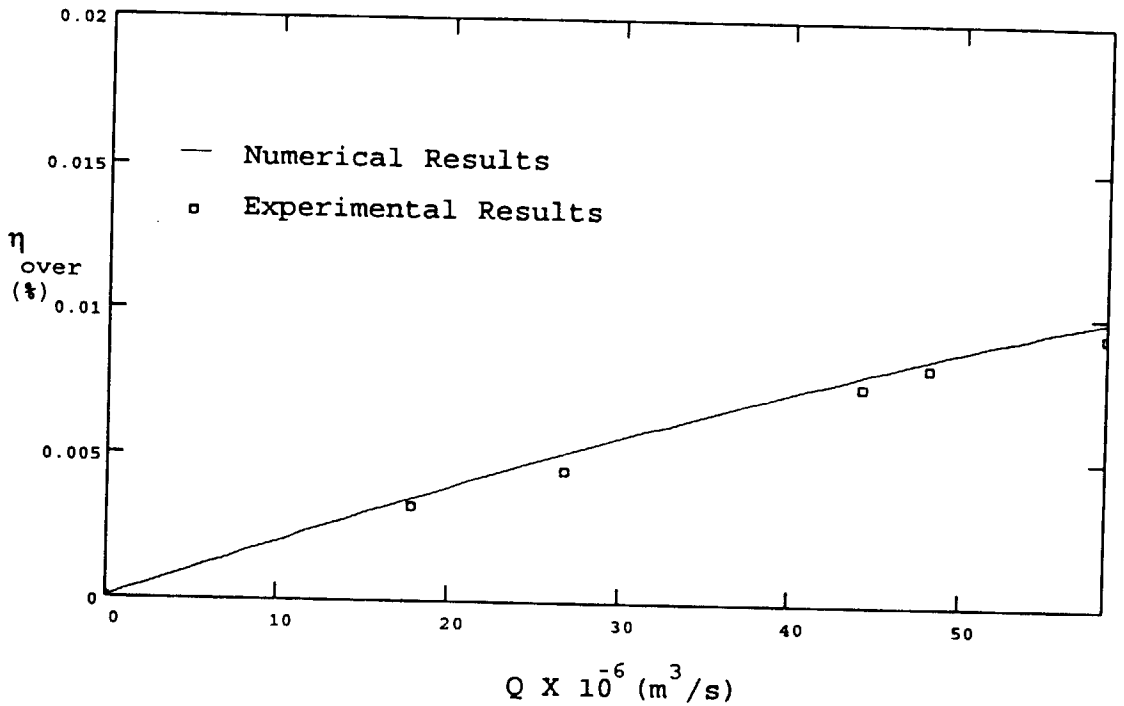

Figure 41

Overall Efficiency Obtained Numerically and Experimentally for V = 15 V and B = 0.2 T

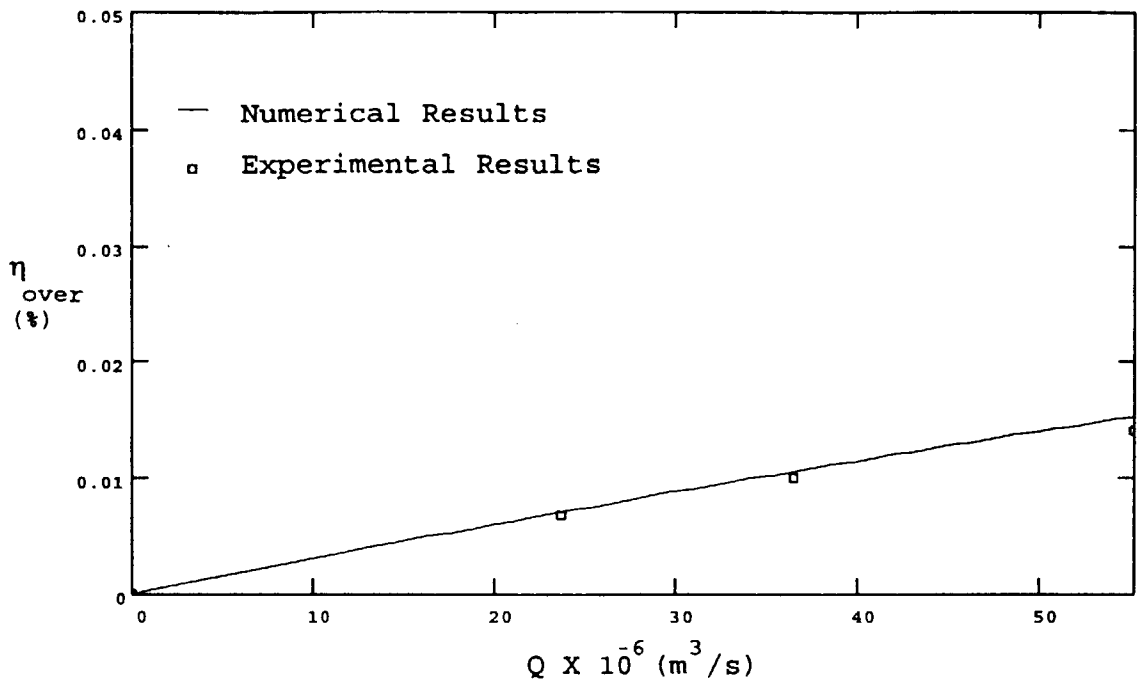

Figure 42

Overall Efficiency Obtained Numerically and Experimentally for V = 15 V and B = 0.3 T

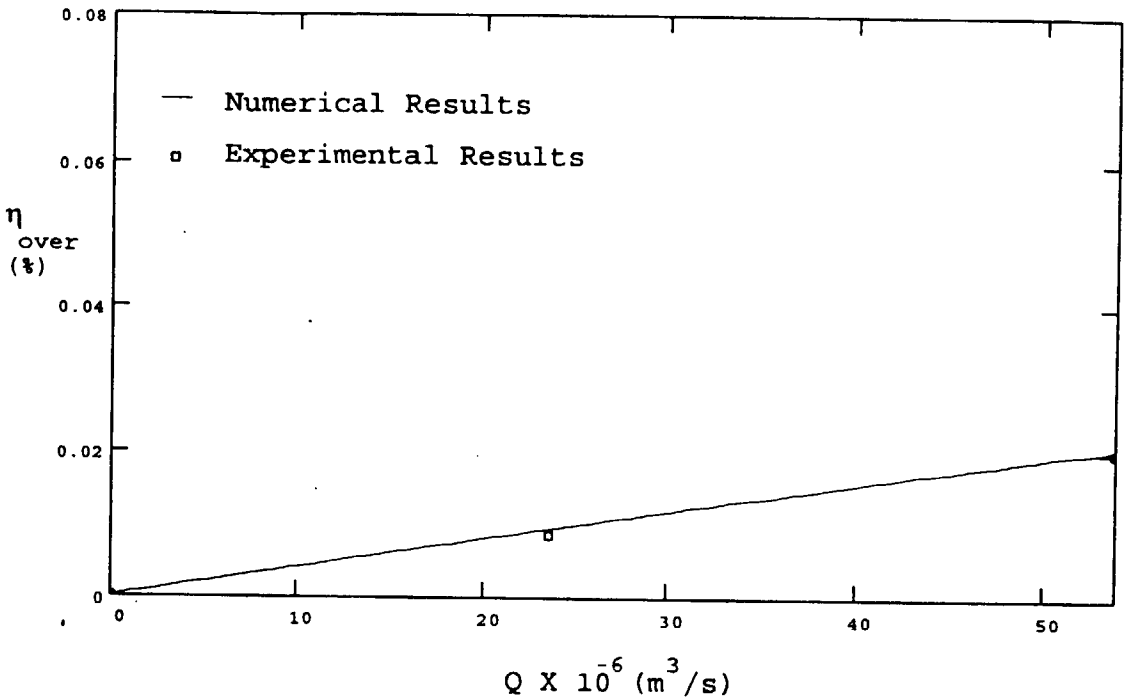

Figure 43

Overall Efficiency Obtained Numerically and Experimentally for V = 15 V and B = 0.4 T

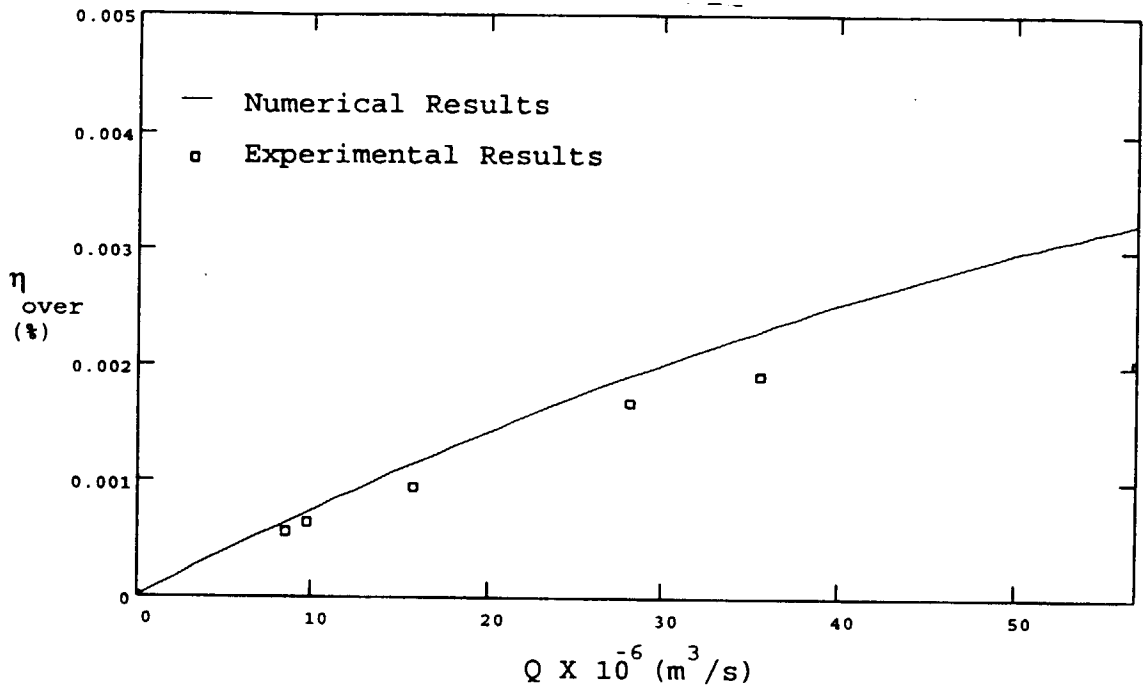

Figure 44

Overall Efficiency Obtained Numerically and Experimentally for V = 20 V and B = 0.1 T

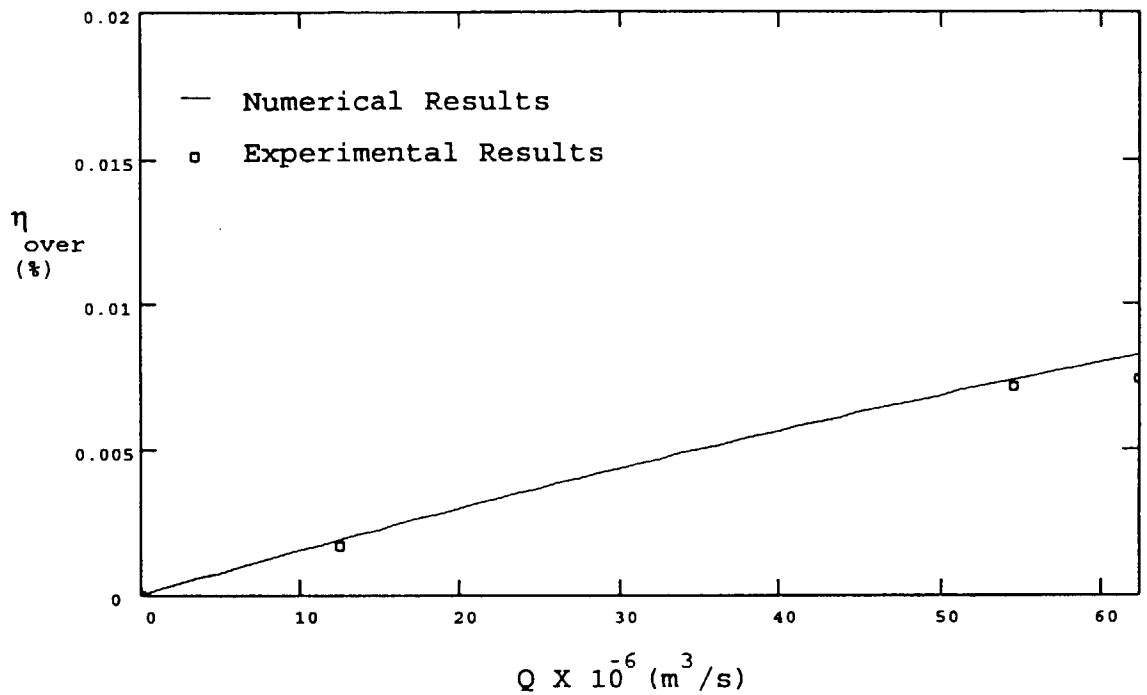

Figure 45

Overall Efficiency Obtained Numerically and Experimentally for V = 20 V and B = 0.2 T

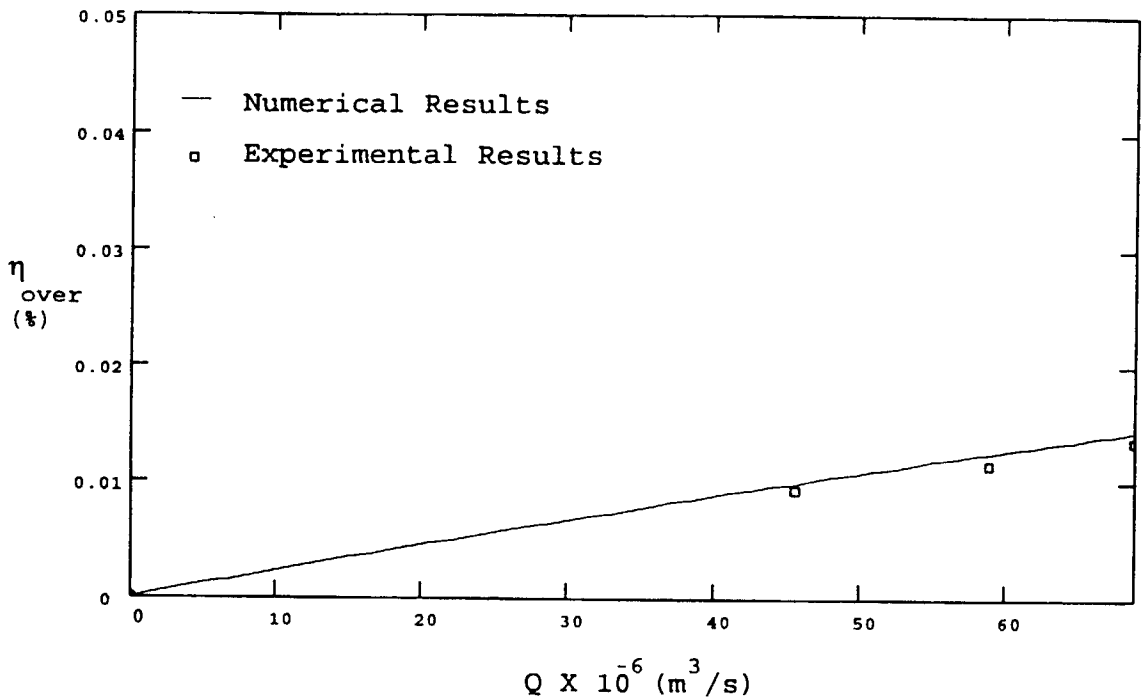

Figure 46

Overall Efficiency Obtained Numerically and Experimentally for V = 20 V and B = 0.3 T

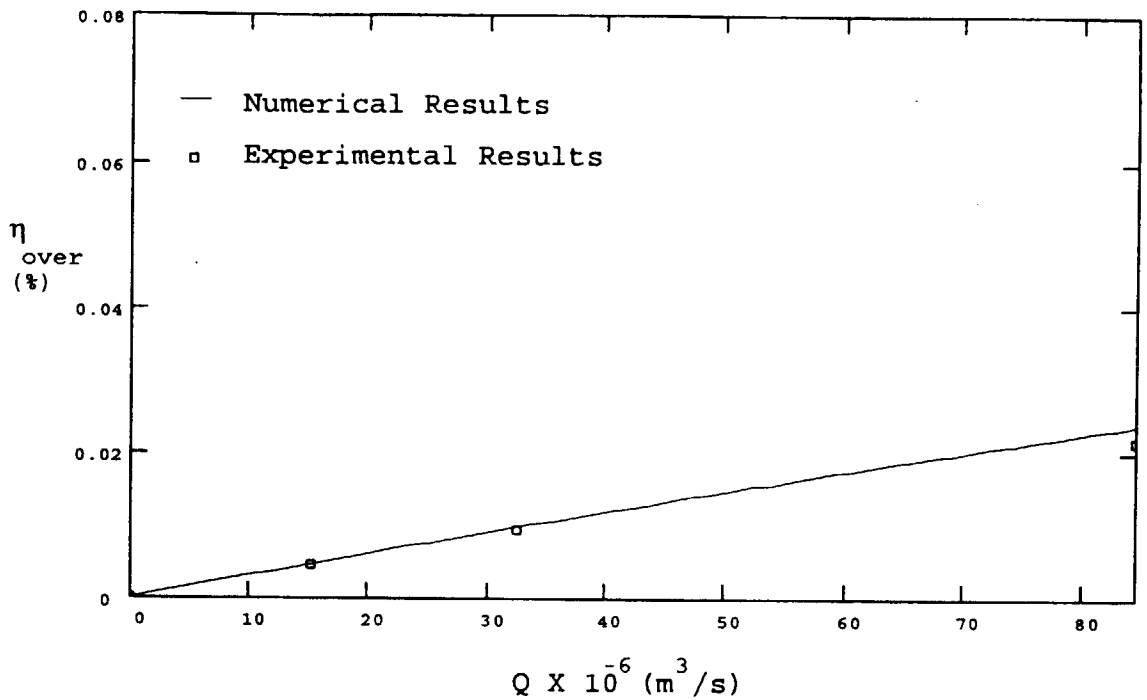

Figure 47

Overall Efficiency Obtained Numerically and Experimentally for V = 20 V and B = 0.4 T

APPENDICES

Appendix A

Computer Program

```
'FINITE DIFFERENCE FOR EHD PUMP
'WRITTEN BY WORANUN WORAMONTRI

CLEAR
SCREEN 0
COLOR 4, 7
CLS

LOCATE 3, 20
PRINT "Finite difference for EHD Conduction Pump"
LOCATE 5, 37
PRINT "By"
LOCATE 7, 30
PRINT "Woranun Woramontri"

'MENU
COLOR 1, 7
LOCATE 11, 20
PRINT "1. Find Velocity Profile Only"
LOCATE 13, 20
PRINT "2. Find P-Q Relationship Only"
LOCATE 15, 20
PRINT "3. Find Velocity Profile and P-Q Relationship"
10 LOCATE 20, 20
```

```
COLOR 6, 7
INPUT "Please select (1-3) ", menu
COLOR 1, 7

SELECT CASE menu

        CASE 1
                CLS
                LOCATE 5, 24
                COLOR 3, 8
                PRINT "  VELOCITY PROFILE CALCULATION  "
        CASE 2
                CLS
                LOCATE 5, 24
                COLOR 12, 1
                PRINT "  PRESSURE-FLOW RATE CALCULATION  "
        CASE 3
                CLS
                COLOR 14, 3
                LOCATE 5, 29
                PRINT "  VELOCITY PROFILE  "
                LOCATE 7, 37
                PRINT " AND "
                LOCATE 9, 24
                PRINT "  PRESSURE-FLOW RATE CALCULATION  "
        CASE ELSE
```

```
                    GOTO 10

END SELECT
COLOR 1, 7

'INPUT DATA
LOCATE 12, 20
INPUT "Number of Vertical Nodes"; nv
IF nv = 0 THEN nv = 11
LOCATE 13, 20
INPUT "Number of Horizontal Nodes"; nh
IF nh = 0 THEN nh = 41
LOCATE 14, 20
INPUT "Distance Between Nodes"; h
IF h = 0 THEN h = 0.00006392
LOCATE 15, 20
INPUT "Length of the Pump"; length
IF lenth  = 0 THEN length = 0.1016
LOCATE 16, 20
INPUT "Magnetic Flux Density"; b
LOCATE 17, 20
INPUT "Voltage apply Across the Electrodes"; volt

SELECT CASE menu

        CASE 1
```

```
            LOCATE 18, 20
            INPUT "Pressure Rise Across the Pump"; dp
            LOCATE 19, 20
            INPUT "File to Write Velocity Profile"; vel$
            vel$ = vel$ + ".DTA"
            OPEN vel$ FOR OUTPUT AS #1
            dta = 1

CASE 2
            LOCATE 18, 20
            INPUT "Maximum Pressure Rise Across the
                  Pump"; maxdp
            LOCATE 19, 20
            INPUT "Data Points Required (for P-Q)"; dta
            LOCATE 20, 20
            INPUT "File to Write Pressure-Flow Rate";
                pq$
            pq$ = pq$ + ".DTA"
            OPEN pq$ FOR OUTPUT AS #2

CASE 3
            LOCATE 18, 20
            INPUT "Maximum Pressure Rise Across the
                  Pump"; maxdp
            LOCATE 19, 20
            INPUT "Data Points Required (for P-Q)"; dta
```

```
                LOCATE 20, 20
                INPUT "File to Write Pressure-Flow Rate";pq$
                OPEN pq$ FOR OUTPUT AS #2
                LOCATE 21, 20
                INPUT "File to Write Velocity Profile"; vel$

        CASE ELSE
                CLS : PRINT "There is no such a mode!"
END SELECT

'INITIALIZE CONSTANTS

'S.O.R CONSTANTS
w = 1.7                                 'OPTIMAL S.O.R VALUE
ww = 1 - w

'ELECTROMAGNETIC/FLUIDIC CONSTANTS
sig = 4.44                              'FLUID CONDUCTIVITY
mu = .000935                            'FLUID DYNAMIC VISCOSITY
E = volt / ((nh - 1) * h)               'ELECTRIC FIELD

'FINITE DIFFERENCE CONSTANTS
disv = (nv - 1) / 10                    'FOR DISPLAY PURPOSE
dish = (nh - 1) / 10

'SYSTEM CONSTANTS
```

```
itr = 1                                    'BEGIN WITH ITERATION = 1

'VELOCITY PROFILE ARRAY
DIM u(nh, nv)

'BOUNDARY CONDITIONS
FOR i = 0 TO nh - 1
u(i, 0) = 0
u(i, nv - 1) = 0
NEXT i

FOR j = 0 TO nv - 1
u(0, j) = 0
u(nh - 1, j) = 0
NEXT j

'**********  PHASE I STARTS HERE  **********
'BEGIN ITERATION
30 'CONTINUE
        'PRESSURE CONSTANT
        IF menu = 1 THEN
                        p = dp / length
                    ELSE
                        pincre = maxdp / (length * (dta -
                         1))
                        p = pincre * k
```

```
END IF

k1 = (b ^ 2 * sig) / mu                    'k1
k2 = (p / mu) - ((sig * E * b) / mu)       'k2
c1 = 4 + k1 * h * h                        'c1
c2 = k2 * h * h                            'c2

'FILE NAME FOR VELOCITY PROFILE CASE 3
IF menu = 3 THEN
        dec1 = INT(k / 10)
        dec2 = 10 * ((k / 10) - INT(k / 10))
        FOR i = 0 TO 9
                IF dec1 = i THEN LET dec1$ = CHR$(48
                                          + i)
                IF dec2 = i THEN LET dec2$ = CHR$(48
                                          + i)
        NEXT i
        ve$ = vel$ + dec1$ + dec2$ + ".DTA"
        OPEN ve$ FOR OUTPUT AS #1
END IF

CLS
LOCATE 2, 10
COLOR 4, 7
PRINT "Phase I on progress"
COLOR 0, 7
```

```
LOCATE 3, 10
PRINT "Pressure Rise ="; p * length
IF menu <> 1 THEN
        LOCATE 3, 30
        PRINT "( Max ="; maxdp; "  Step = "; pincre
            * length;")"
END IF
LOCATE 4, 10
PRINT "Calculating Velocity Profile"
COLOR 6, 7
LOCATE 22, 10
PRINT "Press <s> to stop the iteration"
COLOR 1, 7
DIFF = 1

WHILE INKEY$ <> "s" AND DIFF >= .0000001 AND itr <
  300
FOR j = 1 TO nv - 2
FOR i = 1 TO nh - 2
'Check Convergence
IF INT(itr / 10) = itr / 10 AND i = (nh - 1) / 2 AND
  j = (nv - 1) / 2 THEN
        DIFF = ABS(uref - u(i, j))
        uref = u(i, j)
END IF
  UU(i,j) = u(i,j)
```

```
            u(i, j) = 1 / c1 * (u(i + 1, j) + u(i - 1, j) +
                      u(i, j + 1) + u(i, j - 1) - c2)
            u(i, j) = ww * UU + w * u(i, j)

          NEXT i
          NEXT j
          LOCATE 6, 10
          COLOR 6, 7
          PRINT "This is the "; itr; "th Iteration"
          COLOR 1, 7
          itr = itr + 1
          FOR j = 0 TO 10
          LOCATE 8 + j, 10
          PRINT "value of u("; (nh - 1) / 2; ","; j * disv; ")
                 is equal to"
          COLOR 4, 7
          LOCATE 8 + j, 45
          PRINT USING "##.#######^^^^"; u((nh - 1) / 2, j *
                 disv)
          COLOR 1, 7
          NEXT j
          WEND
    'PHASE I COMPLETE
          BEEP
          LOCATE 2, 10
          PRINT "Phase I completed     "
```

```
        IF menu = 2 THEN GOTO 20          'SKIP THIS PROCESS

        LOCATE 4, 10
        PRINT "                                                    "
        LOCATE 22, 10
        PRINT "Writing file to disk                                "
        LOCATE 23, 10
        PRINT "Please wait..."

        'WRITING FILE FOR VELOCITY PROFILE
        FOR j = 0 TO nv - 1
        FOR i = 0 TO nh - 1
        PRINT #1, USING "##.#######^^^^"; u(i, j)
        NEXT i
        NEXT j
        CLOSE #1

'**********  PHASE II STARTS HERE  **********

20 'CONTINUE
        CLS
        LOCATE 2, 10
        PRINT "Phase II on progress"
        LOCATE 4, 10
        PRINT "Calculating Volume Flow Rate"
```

```
sigma = 0
FOR j = 1 TO nv - 2
FOR i = 1 TO nh - 2
        sigma = sigma + u(i, j)
NEXT i
NEXT j
q = sigma * h * h
area = h * h * (nh - 1) * (nv - 1)
vavg = q / area
CLS
COLOR 4, 7
LOCATE 2, 10
PRINT "Phase II completed"
LOCATE 9, 12
COLOR 1, 7
PRINT "Volume flow rate equal to      "; q; " M^3/S"
LOCATE 11, 12
PRINT "Cross-sectional Area equal to  "; area; "M^2"
LOCATE 13, 12
PRINT "Avg. Vel. equal to             "; vavg; "M/S"
IF menu <> 1 THEN
        PRINT #2, USING "##.#######^^^^"; p *
            length; q
END IF
itr = 1
k = k + 1
```

```
IF k < dta THEN GOTO 30
IF menu = 1 THEN END
CLOSE #2
END
```

Appendix B

Fluid Properties

A copper sulfate solution was used as the working fluid for the model verification. Its concentration was 133.4 g ($CuSO_4 \cdot 5H_2O$) per liter of water at STP conditions. Its other properties, also at STP, are shown in Table B.1.

Table B. 1

Properties of Copper Sulfate Solution

Density $(\frac{kg}{m^3})$	1073
Dynamic Viscosity $(\frac{kg}{m \cdot s})$	9.35×10^{-4}
Conductivity $(\frac{C^2 \cdot s}{kg \cdot m^3})$	4.44

Appendix C

Wire Size Calculation for the Electromagnet

An analysis was performed to determine the appropriate wire size required for the electromagnet. The magnetomotive force required to produce the magnetic flux density of 0.4 T was initially calculated from which the appropriate wire size was determined. Figure C.1 illustrates the geometry of the electromagnet. Table C.1 summarizes the electrical properties of the solid copper wire considered for this application.

The magnetomotive force, expressed in terms of ampere-turns, is determined from:

$$NI = B A_{core} R_{tot} \tag{C.1}$$

where N is the total number of turns, I is the current, B is the magnetic flux density, A_{core} is the core cross-sectional area and R_{tot} is the total reluctance of the magnetic circuit.

From the geometry of the electromagnet shown in Figure C.1, R_{tot} can be expressed as,

$$R_{tot} = \frac{R_1}{2} + 2R_2 + R_3 \tag{C.2}$$

where:

$$R_1 = \frac{l_1}{A_{core}\,\mu_s}$$

$$R_2 = \frac{l_2}{A_{core}\,\mu_s}$$

$$R_3 = \frac{l_3}{A_{core}\,\mu_s}$$

The values of lengths l_1, l_2 and l_3 are shown in Figure C.1. The permeability of the steel core μ_s is approximated as:

$$\mu_s = 250\,\mu_o \tag{C.3}$$

where μ_o is the permeability of free space.

According to this analysis, 4206 ampere-turns of the magnetomotive force is required to produce 0.4 T of magnetic flux density at the air gap.

In order to obtain the required current for each wire size, the number of winding turns for each wire size (N) was calculated. The approximation of the winding turns can be determined from:

$$N = \frac{A_{coil}}{A_{wire}} \tag{C.4}$$

where A_{coil} is the total cross-sectional area of the coil and A_{wire} is the cross-sectional area of the wire. The currents required for each wire size were then calculated from:

$$I_{coil} = \frac{NI}{N} = \frac{4206}{N} \tag{C.5}$$

An approximation for the length of the wire used for each case (L_{coil}) was calculated by:

$$L_{coil} = C_{coil}\,N \tag{C.6}$$

where C_{coil} is the mean circumference of the coil. The total resistance of the coil (R_{coil}) was then calculated from the total length and the wire property given in Table C.1. From the current and resistance of each wire size, the required voltage is calculated from:

$$V_{coil} = I_{coil}\,r \tag{C.7}$$

Figure C.2 shows the required voltages for various wire sizes. The required currents for various wire sizes are shown in Figure C.3. From Figures C.2 and C.3, #18 AWG was considered to be the appropriate wire size for this particular application.

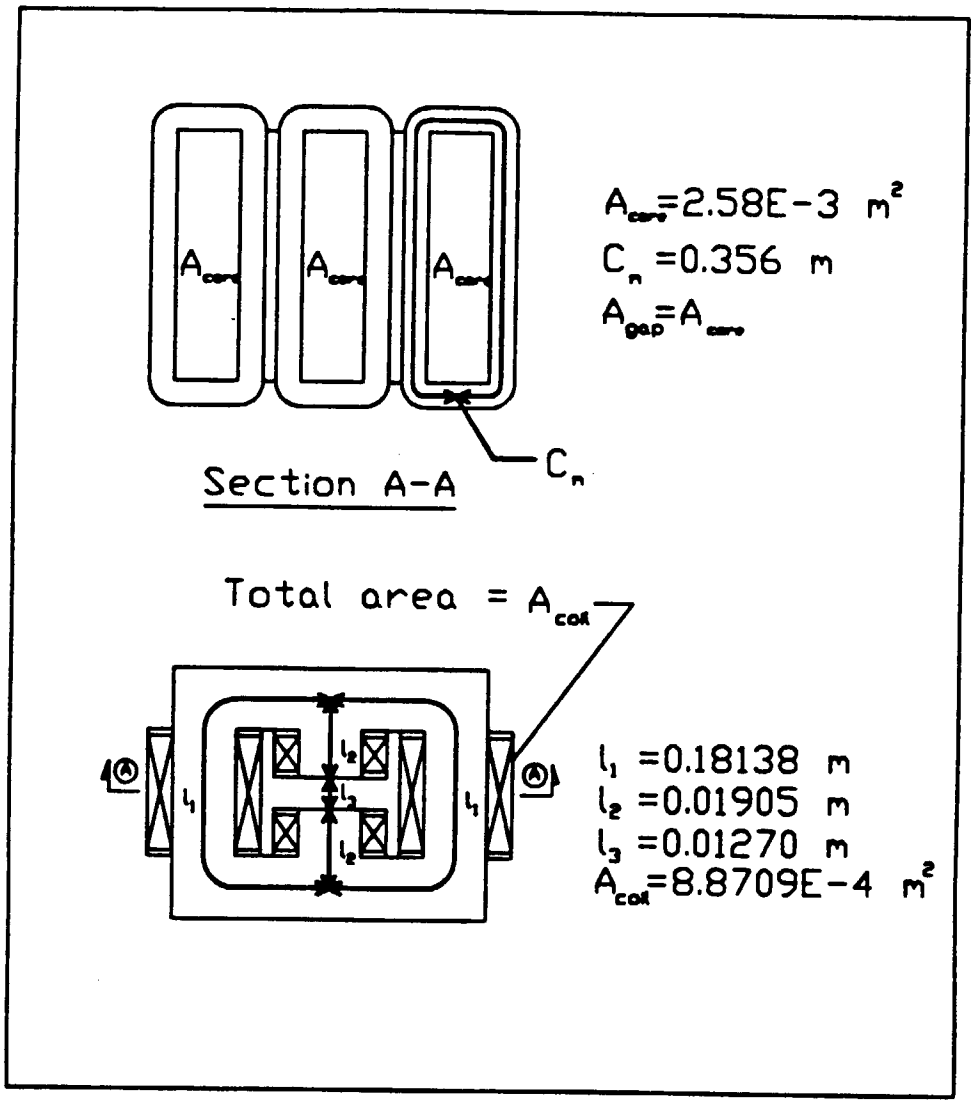

Figure C. 1

Geometry of the Electromagnet

Table C. 1

Properties of Standard Annealed Copper Wire

Gage (in AWG #)	Diameter (mm)	Cross-Sectional Area (mm^2)	Ω per 304.8 m at 25° C
12	2.057	3.3245	1.62
13	1.829	2.6268	2.04
14	1.626	2.0755	2.58
15	1.448	1.6463	3.25
16	1.295	1.3180	4.09
17	1.143	1.0261	5.16
18	1.016	0.81073	6.51
19	0.9144	0.65669	8.21
20	0.8128	0.51887	10.4
21	0.7239	0.41157	13.1
22	0.6426	0.32434	16.5
23	0.5740	0.25881	20.8
24	0.5105	0.20471	26.2
25	0.4547	0.16235	33.0
26	0.4038	0.12810	41.6
27	0.3601	0.10217	52.5
28	0.3200	0.080444	66.2
29	0.2870	0.064701	83.4
30	0.2540	0.050671	105
31	0.2261	0.040136	133
32	0.2032	0.032429	167
33	0.1803	0.025543	211
34	0.1600	0.020111	266
35	0.1422	0.015890	335
36	0.1270	0.012677	423
37	0.1143	0.010261	533
38	0.1016	0.0081073	673
39	0.08890	0.0062072	848
40	0.07874	0.0048695	1070

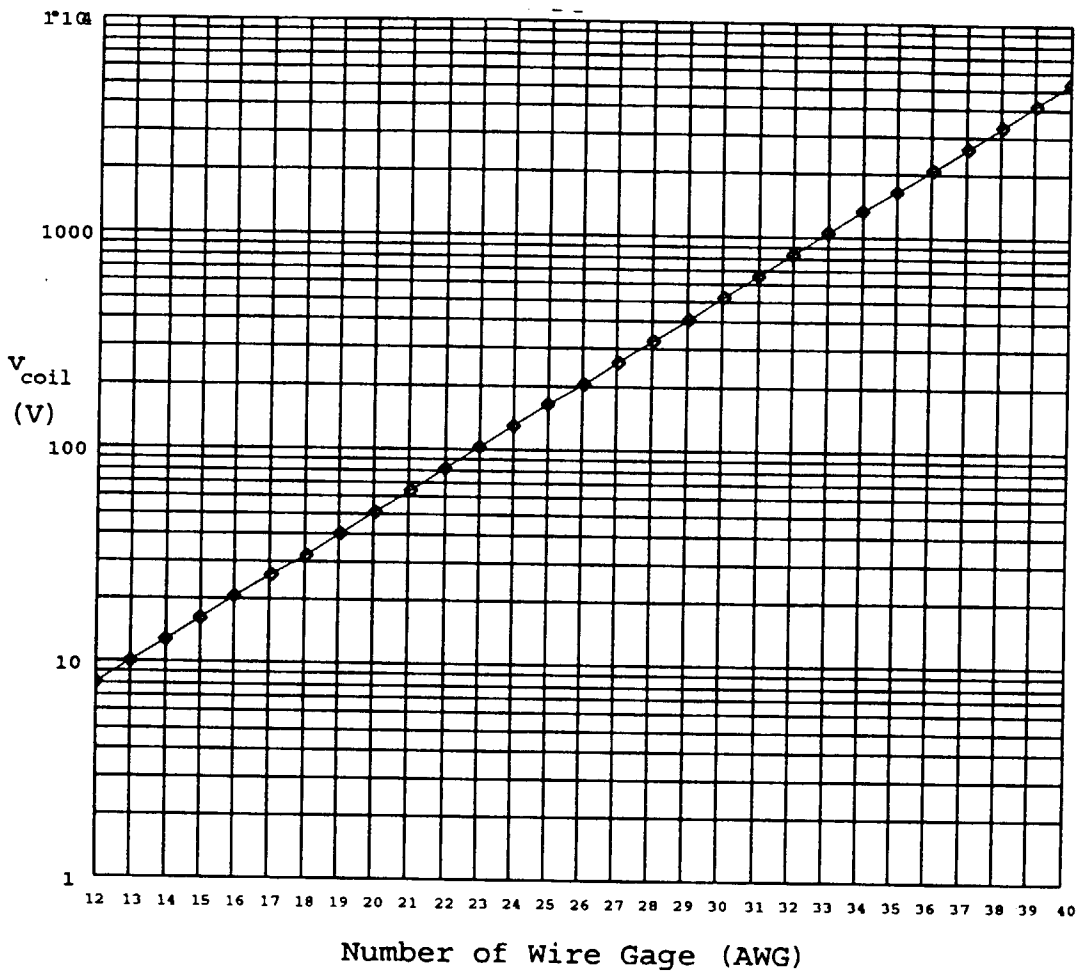

Figure C. 2

Required Voltage as a Function of Wire Size

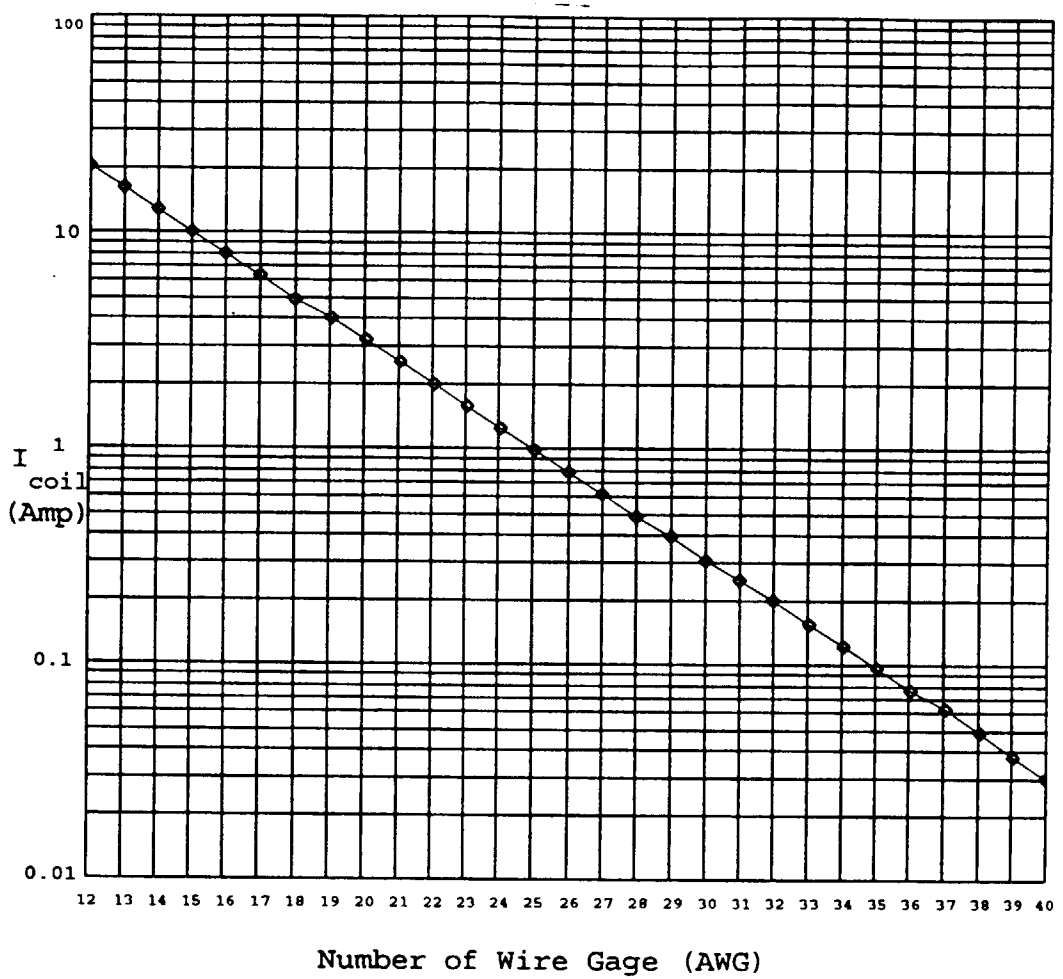

Figure C. 3

Required Current as a Function of Wire Size

Appendix D

Calculated and Measured Magnetic Flux Density

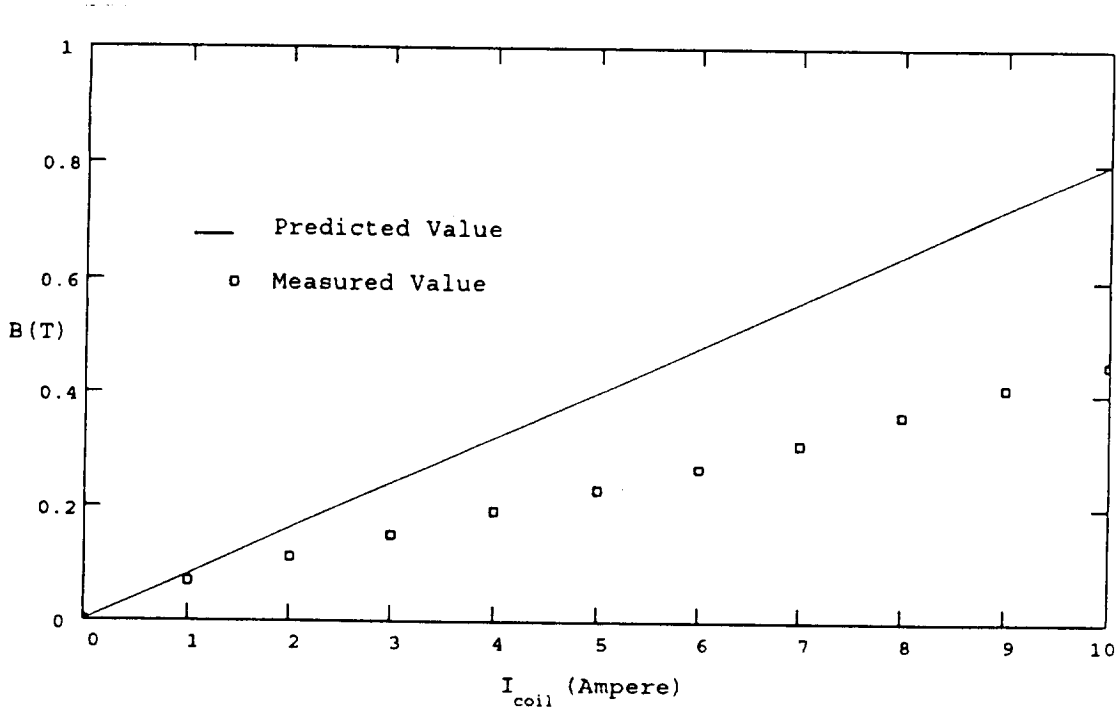

Figure D. 1

Comparison of the Calculated and Measured Magnetic Flux Density

Appendix E

Calibration Curve for the Rotameter

In order to obtain accurate readings, the rotameter used in the experiments was calibrated for the test fluid as shown in Figure E.1.

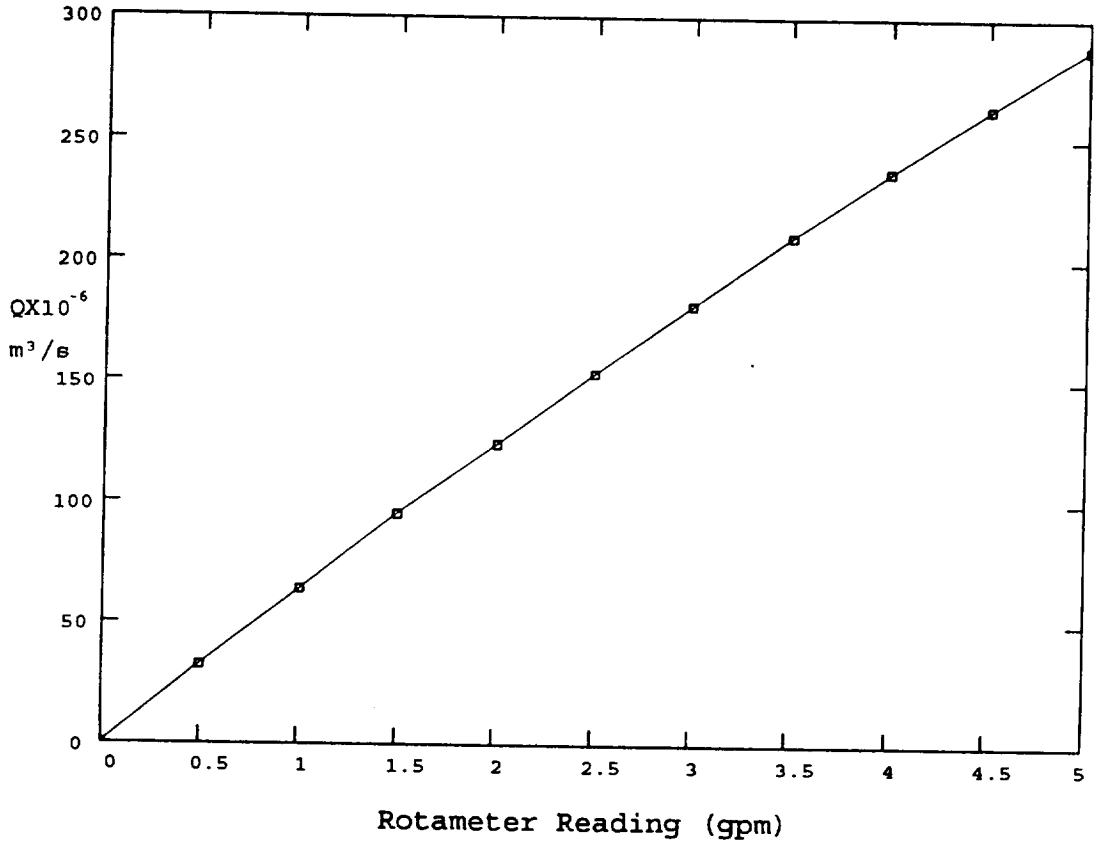

Figure E. 1

Calibration Curve for the Rotameter